A TWO DIMENSIONAL EULER FLOW SOLVER ON ADAPTIVE CARTESIAN GRIDS

A THESIS SUBMITTED TO
THE GRADUATE SCHOOL OF NATURAL AND APPLIED SCIENCES
OF
MIDDLE EAST TECHNICAL UNIVERSITY

BY

BERCAN SİYAHHAN

IN PARTIAL FULFILLMENT OF THE REQUIREMENTS
FOR
THE DEGREE OF MASTER OF SCIENCE
IN
MECHANICAL ENGINEERING

MAY 2008

Approval of the Thesis:

A TWO DIMENSIONAL EULER FLOW SOLVER ON ADAPTIVE CARTESIAN GRIDS

submitted by **BERCAN SİYAHHAN** in partial fulfilment of the requirements for the degree of **Master of Science in Mechanical Engineering Department, Middle East Technical University** by,

Prof. Dr. Canan Özgen _____
Dean, Graduate School of **Natural and Applied Sciences**

Prof. Dr. S. Kemal İder _____
Head of Department, **Mechanical Engineering**

Prof. Dr. M. Haluk Aksel _____
Supervisor, **Mechanical Engineering Dept., METU**

Assist. Prof. Dr. Cüneyt Sert _____
Co-Supervisor, **Mechanical Engineering Dept., METU**

Examining Committee Members:

Prof. Dr. Kahraman Albayrak _____
Mechanical Engineering Dept., METU

Prof. Dr. M. Haluk Aksel _____
Mechanical Engineering Dept., METU

Assist. Prof. Dr. Cüneyt Sert _____
Mechanical Engineering Dept., METU

Prof. Dr. İsmail H. Tuncer _____
Aerospace Engineering Dept., METU

Instructor Dr. Tahsin Çetinkaya _____
Mechanical Engineering Dept., METU

Date: 02/05/2008

I hereby declare that all information in this document has been obtained and presented in accordance with academic rules and ethical conduct. I also declare that, as required by these rules and conduct, I have fully cited and referenced all material and results that are not original to this work.

Name, Last name : Bercan Siyahhan

Signature :

ABSTRACT

A TWO DIMENSIONAL EULER FLOW SOLVER ON ADAPTIVE CARTESIAN GRIDS

Siyahhan, Bercan

M.S., Department of Mechanical Engineering

Supervisor: Prof. Dr. M. Haluk Aksel

Co-Supervisor: Assist. Prof. Dr. Cüneyt Sert

May 2008, 121 pages

In the thesis work, a code to solve the two dimensional compressible Euler equations for external flows around arbitrary geometries have been developed. A Cartesian mesh generator is incorporated to the solver. Hence the pre-processing can be performed together with the solution within a single code. The code is written in the C++ programming language and its object oriented capabilities have been exploited to save memory in the data structure developed.

The Cartesian mesh is formed by dividing squares successively into its four quadrants. The main advantage of using this type of a mesh is the ability to generate meshes around geometries of arbitrary complexity quickly and to adapt the mesh easily based on the solution. The main disadvantage of this method is that the treatment of the cells that are cut by the geometry.

For the solution procedure Roe's method as well as flux vector splitting methods are used for the flux evaluation. The flux vector splitting schemes used are van Leer, AUSM, AUSMD and AUSMV methods. Time discretization is performed using a

multi-stage method. To increase the accuracy least squares reconstruction is employed.

The code is validated by performing calculations around a NACA0012 airfoil profile. The effect of reconstruction is demonstrated by plotting the pressure coefficient on the airfoil. The distribution obtained using reconstruction is very close to the experimental one while there is a considerable deviation for the case without reconstruction. Also the shock capturing capabilities of different methods have been investigated. In addition the performance of each method is analyzed for flow around an NLR 7301 airfoil with a flap.

Keywords: Cartesian Mesh Generation, Approximate Riemann Solver of Roe, Euler Equations, Solution Refinement, Flux Vector Splitting

ÖZ

UYARLAMALI KARTEZYEN AĞLARDA İKİ BOYUTLU EULER AKIŞ ÇÖZÜCÜSÜ

Siyahhan, Bercan

Yüksek Lisans, Makina Mühendisliği Bölümü

Tez Yöneticisi: Prof. Dr. M. Haluk Aksel

Ortak Tez Yöneticisi: Yard. Doç. Dr. Cüneyt Sert

Mayıs 2008, 121 sayfa

Bu tez çalışması kapsamında, herhangi bir geometri etrafındaki iki boyutlu sıkıştırılabilir dış akışları Euler denklemlerinin çözümüyle modellemek için bir kod yazılmıştır. Çözücüye bir Kartezyen ağ çözücüsü ilave edilmiştir. Böylece hem ağ oluşturma hem de çözüm işlemlerinin aynı kodla yapılması sağlanmıştır. Kod C++ dilinin nesneye yönelik programlama özellikleriyle veri yapısının kullandığı hafızayı azlatma amacı güdülerek yazılmıştır.

Kartezyen hesaplama ağı karelerin art arda dörde bölünmesiyle oluşturulmaktadır. Kartezyen ağların temel artısı değişik karmaşıklıktaki geometriler etrafında hızla ağ oluşturulabilmesi ve çözüme göre ağın uyarlanabilmesidir. Temel eksisi ise geometri tarafından kesilen hücrelerin ele alınmasındaki zorluktur.

Çözümde hücre akılarını bulmak için Roe'nun metodunun yanı sıra FVS metodları da kullanılmaktadır. FVS metodlarından van Leer, AUSM, AUSMD ve AUSMV kullanılmaktadır. Daha sonra zamanda integrasyon için çok aşamalı bir metod kullanılmaktadır. Yöntemin doğruluğunu artırmak için hücre içinde akış değişkenleri yeniden yapılandırılmaktadır.

Yöntemin geçerliliği NACA0012 kanat profili etrafındaki akış çözülerek sınanmıştır. Yeniden yapılandırmanın etkileri kanat üzerindeki basınç katsayılarının çizilmesiyle vurgulanmaktadır. Yeniden yapılandırmalı dağılım deneysel dağılıma yakındır ancak yeniden yapılandırma olmadan elde edilen sonuçlar deneyselden ciddi farklılıklar göstermektedir. Ayrıca farklı metodların şok yakalama özellikleri de sınanmıştır. Farklı metodların performansları NLR7301 profili etrafındaki akış çözülerek de kıyaslanmaktadır.

Anahtar Kelimeler: Kartezyen Ağ Oluşturucusu, Roe'nun Yaklaşık Riemann Çözücüsü, Euler Denklemleri, Yeniden Yapılandırma, Çözüm Uyarlamalı Ağ

Dedicated to my family

ACKNOWLEDGEMENTS

I would like to thank my supervisor Prof. Dr. Haluk Aksel, co-supervisor Asst. Prof. Dr. Cüneyt Sert and Dr. Ruhşen Çete for their assistance, support and constructive criticisms during my thesis work.

I would also like to thank Emre Gürdamar, Çağrı Şişman, Doruk Özdemir, Güneş Nakiboğlu and Mehtap Çakmak with whom I had the pleasure of having fruitful discussions.

Also I would like to express my appreciation for the company of Ender Özden and Samet Özkan with whom I have shared the same work environment.

Last but not least I would like to express my gratitude for all individuals and institutions that realize and cherish knowledge as something to be shared openly and freely.

TABLE OF CONTENTS

LIST OF TABLES

TABLES

LIST OF FIGURES

FIGURES

LIST OF SYMBOLS

U: vector of conserved variables

$\hat{\mathbf{U}}$:vector of rotated conserved variables

F(U): flux vector function

$\hat{\mathbf{F}}(\hat{\mathbf{U}})$: rotated flux vector function

$\mathbf{F}$: flux vector

dV: volume element

dA: surface area element

$\vec{n}$: face normal

t: time

A_{cell}: area of a cell

Δs : length of cell face

ρ : density

u : velocity in the x-direction

v : velocity in the y-direction

h_t : total enthalpy

p : pressure

$\tilde{\rho}$: Roe averaged density

$\tilde{u}$: Roe averaged velocity in the x-direction

$\tilde{v}$: Roe averaged velocity in the y-direction

$\tilde{h}_t$: Roe averaged total enthalpy

$\tilde{p}$: Roe averaged pressure

e_t : total energy

$\hat{u}$: normal velocity

$\hat{v}$: tangential velocity

γ : specific heat ratio

a : speed of sound

V : velocity

$\tilde{a}$: Roe averaged speed of sound

$\tilde{V}$: Roe averaged velocity

α : angle of attack

T : temperature

M : Mach number

R : gas constant

$\mathbf{T}$: transformation matrix

$\mathbf{A}$: Jacobian of the flux vector

$\mathbf{V}$: vector of characteristic variables

λ : eigenvalue of the Jacobian matrix

$Av(u)$:averaging function

Φ : gradient limiter

$\mathbf{R}$: residual function

β : stage coefficients

σ : CFL number

Ψ : convective spectral radius

S : length of projection

Subscripts

c : value at centroid with th

R : right state variable

L : left state variable

stag : stagnation condition

inf : free stream

x : derivative in x component

y: derivative in x component

Superscripts

~ : Roe averaged quantity

ˆ : components in normal-tangential coordinates

T : transpose

- : averaged quantity

max : maximum value

min: minimum value

x: component in the x-direction

y: component in the y-direction

CHAPTER 1

INTRODUCTION

In this thesis, numerical methods are employed to resolve external flows around arbitrary geometries. The thesis work consists of generating a Cartesian mesh around the input geometry, solving the Euler equations numerically with the finite volume method for the desired flow quantities and obtaining the necessary aerodynamic forces to verify the solution. To understand the motivation for choosing the methods followed, a brief introduction must be made to mesh generation and solution techniques employed in the field of computational fluid dynamics (CFD).

1.1 Overview of Computational Fluid Dynamics (CFD)

Computational fluid dynamics is a branch of fluid dynamics which employs numerical methods for solving the equations of fluid flow which are impossible to solve analytically due to their complex nature. Hence CFD is the third approach for solving a flow problem alongside analytical and experimental methods.

It can be said that emergence of CFD as a tool for solving flow problems has taken place only in the mid 1900s so it is a relatively new field of study compared to analytical and experimental methods. Since the publication of Isaac Newton's *Principia* in 1687, theoretical and experimental methods, often combined, were the only tools for analyzing fluid flows of differing nature (1). With the development of digital computers, however, CFD has become an indispensible tool in the field of fluid dynamics, arguably with the pioneering work of Kopal who in 1947 formed tables for the supersonic flow over sharp cones after solving the governing equations numerically. In the 1950s and 1960s CFD, has been applied to re-entry problems and

has established its place among the three essential methods for analyzing a fluid flow problem (1).

1.2 Main Elements of a CFD Program

Any CFD program mainly consists of three parts; the pre-processor, the solver and the post-processor (2) .

The pre-processor gathers the inputs to the problem being analyzed, the fluid properties, boundary conditions, geometry around which the fluid flow will be investigated. Also the grid is generated around the input geometry by the pre-processor.

The solver part of the program uses numerical techniques to resolve the flow around the input geometry. This is accomplished by converting the governing partial differential methods to algebraic set of equations in the three conventional finite difference, finite element and finite volume methods.

The post-processor is the part where the solution obtained is visualized. Contours of desired scalars and the vector fields are displayed within the domain of interest. Also non-dimensional variables and physical quantities of interest are calculated so as to verify the solution and to judge whether the mesh generated and the schemes used are appropriate for the problem at hand.

The program developed in the scope of the thesis work contains a pre-processor which gathers the inputs of the problem and generates a Cartesian mesh in the computational domain and a solver which uses the finite volume method for the solution of the compressible Euler equations in the conserved form. The mesh generation and different solution methods will be discussed in some detail below. For the post-processor a commercially available program Tecplot and a freely distributed program Mayavi have been used.

1.3 Mesh Generation

Mesh generation is the most time consuming and the most crucial step in obtaining a solution to a fluid flow problem. The generated mesh should comply with requirements of the solution schemes to be used in order to get accurate results.

In general, there are two types of meshes; the structured and the unstructured meshes. Each one of these two types of meshes can then be classified further according to the method used to construct them.

1.3.1 Structured Meshes

A mesh is considered to be structured if the organization of the grid points and the form of the grid cells depend on a general mathematical rule instead of their position (3). In other words, the grid points can be arranged as a regular array as (i, j, k) with the neighbouring point being known as (i, j, k+1) (4). Hence the connectivity of the grid points to form the cells is implicitly implied by the general mathematical rule.

The structured grids can be classified further according to the technique used to generate them as algebraic, elliptic and hyperbolic grids. The algebraic grids are formed simply by transforming cells in a Cartesian computational domain to a physical domain to obtain a boundary conforming mesh, the elliptic grids are obtained as a result of solving an elliptic differential equation to obtain a mesh that satisfies the Laplace equations while for the hyperbolic grids are obtained by solving hyperbolic equations (4).

The advantages of structured meshes are that they are boundary conforming so by adjusting the grid spacing, meshes for viscous solutions can be obtained. They require less data storage since the connectivity information is implicitly known.

One disadvantage of the structured meshes is that they require more computation power, since the governing partial differential equations or the algebraic rules must be solved and computations must be performed for the transformations from the

computational to physical spaces. However the most important disadvantage of the structured meshes is that they cannot easily be applied to complex geometries that are formed by more than one body that have small clearances or are not well streamlined.

1.3.2 Unstructured Meshes

If the grid points cannot be arranged as a regular array and additional information is required for the connectivity of the grid points then the mesh is unstructured. The unstructured meshes, though they can comprise of elements of any shape, are formed of triangular or rectangular elements generally in the two-dimensional case.

The advantages of the unstructured meshes are that they can be applied to geometries of arbitrary complexity with ease, they are more suitable to automatic meshing, and no transformation between a computational and a physical domain will be needed. While the disadvantage of these meshes is that they require more complex data structures for storing the connectivity of grid points and the neighbour cell information.

1.3.2.1 Triangular Unstructured Meshes

The most widely used methods for forming triangular unstructured meshes are the advancing front and the Delaunay triangulation methods.

In the advancing front method, the points are added to the ones that represent the geometry as the mesh is created. The added points are connected to already existing points to form triangles. Then, the points that are available for triangle formation termed as the front are connected to newly added points to update the front until the whole domain is meshed (4). In this approach, extensive search algorithms must be employed when adding new grid points to ensure that the newly formed cells adjust to the existing ones. Also, the closing stage of this approach, where the front folds

over itself, introduces some difficulties (3). An example of the advancing front method is illustrated in Figure 1.1.

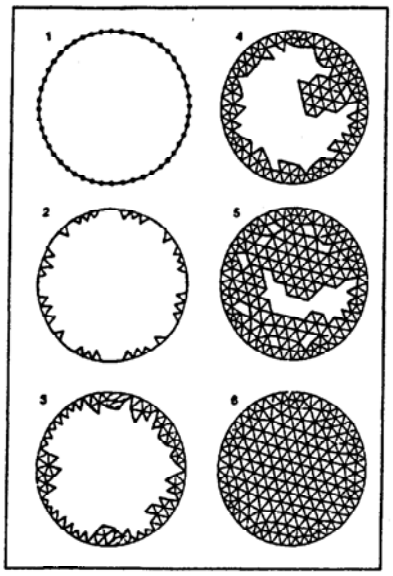

Figure 1.1- The stages of the advancing front method

The other and may be the most popular triangular meshing procedure, Delaunay triangulation, requires points to be created before the meshing process and is closely linked to the concept of Vornoï diagrams. The Vornoï diagram is obtained by tessellating the domain into Vornoï regions which are regions that are closer to one particular point within the domain than the others. This is illustrated in Figure 1.2. Hence they can be obtained by the perpendicular bisectors of the lines between neighbouring points. Once the diagram is formed, any points that have a Vornoï edge between them are connected to form the triangular mesh. The circum-circles of the triangular elements do not contain any other point in the domain and the resulting mesh is unique for the point distribution. This method is suitable for mesh adaptation since for a newly added point, the Vornoï diagram is updated locally and new triangles are formed.

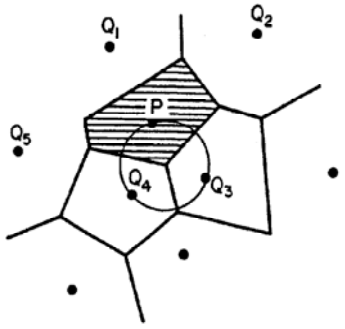

Figure 1.2- Vornoï diagram for the grid points

1.3.2.2 Cartesian Meshes

The Cartesian mesh is obtained by using the quad-tree approach in two dimensions. In the quad-tree approach, a square containing the whole domain is divided into its four quadrants to form the mesh in a tree structure. Hence, the procedure followed is much simpler than the methods for generating triangular unstructured meshes. Also, in the computation stage, the flux vectors won't have to be rotated for the greater portion of the cells. The method is very suitable for adaptation, since for the adaptation, the cell has to be simply divided into its four quadrants.

If the quad-tree approach is followed strictly, then the surface of the geometry cannot be represented accurately hence the cut-cells are used to alleviate this problem which introduces some complexity to the approach. The orientation of the geometry may cause formation of very small cut-cells, which is generally undesirable.

The code developed uses the quad-tree approach to form a Cartesian mesh for the solution. This approach was chosen to mesh arbitrary geometries of differing complexities in an automatic fashion. Also the approach is simpler than triangular mesh generation techniques and it will promote simpler calculations in the solution stage.

1.4 Solution Methods

The partial differential equations governing the flow of a fluid must be discretised in order to convert them into algebraic equations and get a numerical solution. The most widely used methods for the discretisation of the governing equations are the finite difference, finite element and finite volume methods.

1.4.1 Finite Difference Method

The finite difference method is based on the differential form of the governing system of partial differential equations. The derivatives of the conserved quantities appearing in these equations are approximated by differences of these unknown quantities at neighbouring grid points. These differences are derived from the Taylor series and their order of accuracy is dependent on the number of points used in the difference equation. Once the difference equations are written in terms of unknown quantities, these algebraic equations can be solved numerically with the boundary conditions to obtain the value of the conserved quantities at each grid point.

The major setback of this method is that it requires a regular structured mesh in order to express the derivatives accurately (5). Hence, the method is not very suitable for unstructured meshes or cases where the geometry is complex.

1.4.2 Finite Element Method

The finite element method which was initially developed for structural problems from 1940s through 1960s, divides the computational domain into triangular or rectangular sub-domains and represents the variation of the unknown quantities in terms of piecewise continuous functions. Then the unknown coefficients of these functions are found by establishing algebraic equations through satisfying the governing equations in a weighted residual form over each element (6).

The finite element method, with its mathematical background being functional analysis, has been investigated by mathematicians since its development for engineering purposes, and is a very rigorous method with specific conditions for existence and convergence criteria and exactly derived error bounds.

Even though this method is very well established in structural mechanics, it is still in the stages of evolution for complex flow problems such as compressible flows governed by Euler or Navier-Stokes equations (1).

1.4.3 Finite Volume Method

The finite volume method which was first devised as a special form of the finite difference method in the 1970s uses the integral form of the governing equations of a fluid flow. There is a wide range of methods for discretising the convective and diffusive terms of the governing integral equations as well as the definition of the control volumes for which the governing equations are satisfied. More specifically it is possible to store the flow variables at the centroid of the cells for a cell centred approach, or at the vertices for a cell vertex formulation. Another possibility is to have a staggered grid where the scalar quantities and different vector quantities can be stored on overlaid cells as in the Semi-Implicit Method for Pressure-Linked Equations (SIMPLE) algorithm (2). Hence the method has a considerable inherent flexibility (5). Also, since the method is directly based on the governing integral equations, the basic concepts of the different schemes are more comprehensible than the finite element method (2). This property of the finite volume method promotes development of numerical schemes based on physics of the flow. Approximate Riemann methods, which are used for evaluating the convective terms is one example. One other advantage of the method is with the direct discretisation of the governing integral equations, conservation of mass, momentum and energy will be guaranteed at a discrete level (5).

In the code developed, cell centred finite volume method has been used with of Roe's approximate Riemann method for the evaluation of the convective fluxes through the cell surfaces as well as the flux vector splitting schemes.

1.5 Assessment of the Solution Methods

Theoretically, a numerical solution will tend to the exact solution if infinite number of cells is used. Since this is not reasonable, a numerical scheme must possess the conservativeness, boundedness and transportiveness properties (2). The conservativeness property states that flux leaving through a certain face of a cell must enter the adjacent cell. The boundedness of a solution guarantees that numerical errors introduced by the discretisation of the governing equations will not prevent convergence. This property is related to the stability of the discretisation scheme used. The stability of a scheme can be analyzed by the discrete perturbation analysis or the von Neumann stability analysis (7). Finally, the transportiveness of numerical scheme deals with the directionality of the solution. For example, the solution of a flow dominated by convection will depend more on the upwind direction, hence upwind schemes will be more appropriate; whereas for a flow that is diffusive, a non-directional central method will be more appropriate.

CHAPTER 2

DATA STRUCTURE & MESH GENERATION

2.1 Data Structure

In the code developed, a Cartesian unstructured mesh is generated around the input geometry. Since an unstructured mesh is used, the first step in the mesh generation is to construct an appropriate data structure that will store the necessary data for each cell in the domain. However before describing each variable that is stored, the terminology adopted must be explained.

2.1.1 Terminology for the Cartesian Cells

The mesh is obtained by dividing squares successively, starting from a single large square, by connecting the midpoints of opposing edges until the desired resolution is obtained. This process results in a tree structure. The large square comprising the outer boundary of the domain is termed as the root cell. A cell (square) is called the parent of its four quadrant cells which form as a result of division and the four quadrant cells are called the children of the parent cell in turn. The children cells are numbered according to the quadrant they occupy. A cell without any children is called a leaf cell. The leaf cells can also be called the computational cells since the actual calculations for the field variables are performed for these cells. These concepts are illustrated below in Figure 2.1.

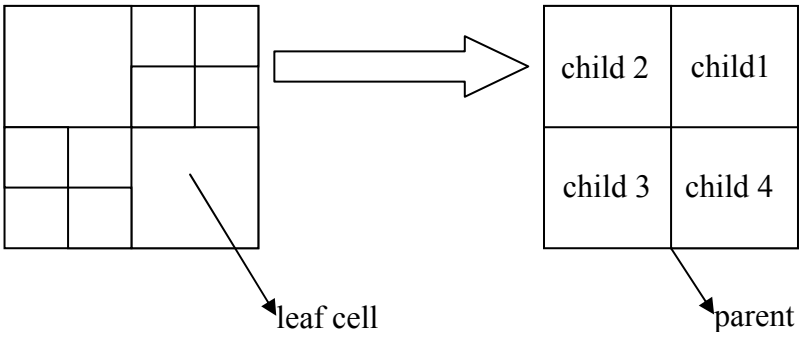

Figure 2.1- The relation between cells

Among the computational cells, some are cut by geometry lines and these are called cut-cells. The other cells mainly serve the purpose of traversing the tree. Also there is a level concept associated with each one of the cells. The level of the four children of a cell is one higher than that of their parent. The root cell is assigned a level of zero. The tree structure associated with the structure shown in Figure 2.1 is illustrated in Figure 2.2 to exemplify some of the concepts defined above.

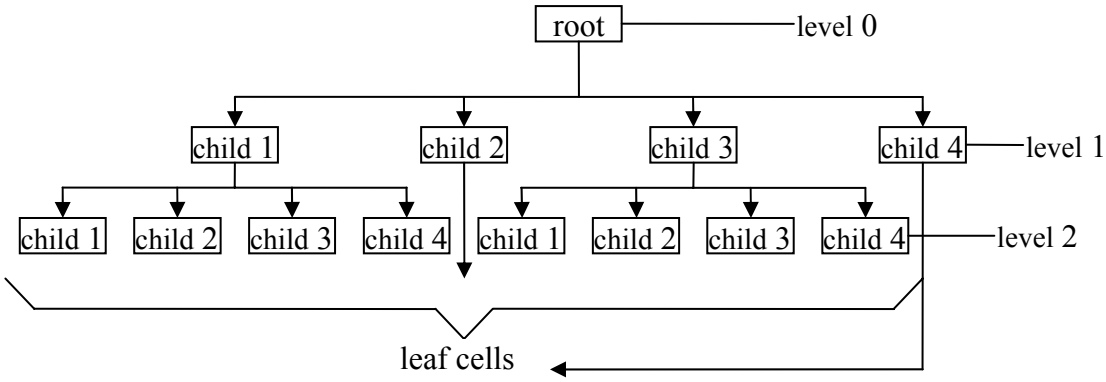

Figure 2.2- The tree structure

2.1.2 Neighbour Cell Procedures

As was mentioned before for unstructured meshes the neighbours must also be stored since for the calculation of the fluxes through a face, the neighbour along that edge must be known. Also the neighbours will be used to determine the variation of the conserved variables within the cells.

A cell will have four neighbours along its edges called the edge neighbours. These neighbours are named east, west, north and south according to the edge they are associated with. Also computational cells will have four neighbours through their vertices named as vertex neighbours; northeast, southeast, northwest, southwest. The general rule for the mesh is that a cell can have neighbours of levels that are one degree different than the cell. This ensures the grid smoothness and also simplifies flux calculations through the faces. If a neighbour is at the same level or one lower level, then it will be recognized as the neighbour along the corresponding edge, but if it is at one higher level the neighbour's parent will be recognized instead of having two neighbours along the edge. Figure 2.3 illustrates the concepts related to neighbouring relations and also the possible configurations that might occur for a cell.

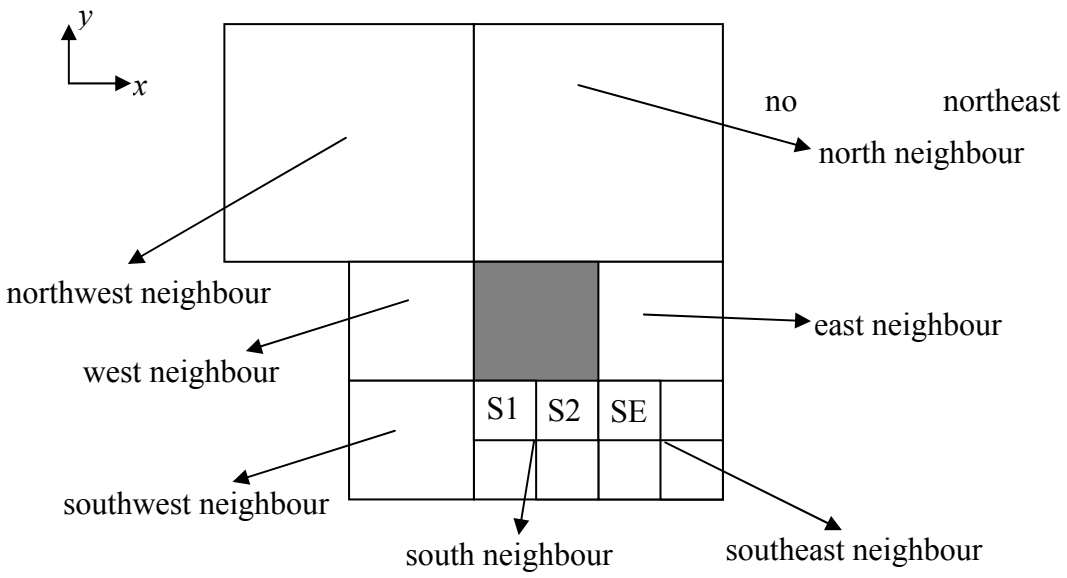

Figure 2.3- Neighbours of a cell

In Figure 2.3 the east, west and southwest neighbours of the cell are at the same level while the north and northwest neighbours are at one lower level. These cells are recognized as the neighbours themselves meanwhile the parent of the cells marked as S1, S2 and SE are recognized as the south and southeast neighbours respectively. Since the north neighbour is at a lower level the north and northeast neighbours are identical in which case the cell is considered to have no northeast neighbour, hence a vertex neighbour of a cell should be distinct if it is to be stored.

2.1.3 Information for Cut and Computational Cells

As it is defined earlier there are three types of cells; the parent cells for traversing the tree, the computational leaf cells and the cut-cells, which are special types of computational cells. The amount of data stored for each cell depends on its type. The information stored for a parent cell is shared for all types of cells, while computational cells will have additional information and for cut-cells further additional information will be stored.

For each cell in the domain, the x and y coordinates of the centre and the level of the cell are stored. Also there are a total of thirteen pointers pointing to other cells in the domain. Of these thirteen pointers four point to the children of the cell, if the cell is a leaf cell then these pointers are null pointers. Eight of the remaining nine pointers point to the neighbours of the cell. Of these eight pointers four point to edge neighbours, the remaining four point to the vertex neighbours and they are allocated only for computational cells. The remaining one of the thirteen pointers points to the parent of the cell. This pointer is null only for the root cell.

Besides the thirteen pointers aforementioned there are nine more pointers which are allocated only for computational cells. Four of these pointers store the conserved field variables for the continuity, momentum and energy equations. Of the remaining five pointers two are storing the gradient and the curl of the velocity vector. One pointer stores information dictating the cell to be refined at a stage of mesh generation or solution adaptation. One stores coefficients that will be used in solution

reconstruction and the last one stores the type of the cell; whether the cell resides totally outside or inside the geometry or whether it is cut by it.

Finally there is a set of seven pointers which are allocated for the cut-cells. Three of these seven pointers store the x and y coordinates of the centroid and area of the cell while two store the x and y coordinates of the end lines of the intersections of geometry lines with the cell edges. Of the remaining two pointers one stores which edges are cut by geometry lines while the last one stores information on which portion of the cell's edges flux passes through. The table below shows a summary of the information stored for different types of cells.

Table 2. 1- Information stored for different types of cells

ALL CELLS	
xcent:	x coordinate of center of square containing the cell
ycent:	y coordinate of center of square containing the cell
level:	level of the cell
child1:	pointer to first quadrant child
child2:	pointer to second quadrant child
child3:	pointer to third quadrant child
child4:	pointer to fourth quadrant child
eneigh:	pointer to east neighbour
wneigh:	pointer to west neighbour
nneigh:	pointer to north neighbour
sneigh:	pointer to south neighbour
parent:	pointer to parent
COMPUTATIONAL CELLS	
ro:	density associated to the cell
rouvel:	product of density and velocity in the x direction associated to the cell
rovvel:	product of density and velocity in the y direction associated to the cell
roen:	product of density and total energy associated to the cell
gradient:	pointer to gradient of velocity
curl:	pointer to curl of velocity
recons:	pointer toarray containing geometry based reconstruction coefficients
refine:	pointer to flag for refinement
celltype:	pointer to the cell type (inside, outside, cut-cell)
neneigh:	pointer to northeast neighbour
seneigh:	pointer to southeast neighbour
nwneigh:	pointer to northwest neighbour
swneigh:	pointer to southwest neighbour
CUT-CELLS	
centx:	pointer to x coordinate of the centroid of the cell
centy:	pointer to y coordinate of the centroid of the cell
area:	pointer to the area of the cell
xcut:	pointer to the x coordinate of cut location on edge
ycut:	pointer to the y coordinate of cut location on edge
edgecut:	pointer to edges cut byb the geometry
fluxcut:	pointer to the information regarding flux

2.2 Clipping Procedure

Before describing the mesh generation process in detail, the procedure for determining the location of the points cut by the input geometry for the cut-cells must be explained.

Clipping is the process of determining the portion of a geometrical shape that resides within a given clipping window. For the code developed, the input geometry, which is a polygon comprising of connected line segments, is to be clipped and the clipping windows are the computational cells within the domain. The two options for the clipping procedure are the polygon clipping, if the input geometry is conceived as a polygon, line clipping if the input geometry is conceived as a collection of individual line segments.

2.2.1 Comparison of Polygon and Line Clipping Algorithms

When the polygon and line clipping algorithms are compared, in general, it is seen that the simplest polygon clipping algorithm, Sutherland-Hodgeman (8), is not capable of handling concave geometries effectively. However there are other polygon clipping algorithms that can handle arbitrary geometries such as self intersecting geometries and geometries with internal holes. Since these cases are not in the scope of the current study, the application of these algorithms would bring unnecessary complications. Hence, the line clipping algorithms are preferred to polygon clipping algorithms.

After this general comparison, a few of the line clipping algorithms were compared amongst themselves. First the Liang-Barsky (9) line clipping algorithm is compared with the most classical algorithm, Sutherland-Cohen (10) algorithm. In the work of Liang and Barsky (9), the performance of their algorithm was tested along with the Sutherland-Cohen line clipping algorithm with 4 sets of data containing 1000 randomly generated line segments. To reduce the effects of random variation, each line segment was clipped 1000 times resulting in a total of 4 million clippings. It was

reported that an improvement of about 36 percent in the execution time was obtained.

Even though Liang and Barsky claim that their algorithm is more efficient than Sutherland Cohen, other researchers postulate that experimental analysis is inadequate to measure the performance of a clipping algorithm. Instead it is suggested that a measurement based on operation count should be used (11). A study conducted by J. D. Day (12) takes both the experimental and operations count view into consideration and reveals that Nicholl-Lee-Nicholl (11), Sobkow-Pospisil-Yang (13) algorithms are more efficient in both aspects compared to the Liang-Barsky algorithm. However the algorithms mentioned are considerably more complex, in fact the latter algorithm classifies lines into 81 different cases.

Since the clipping procedure will be carried out once at the mesh generation step for all the computational cells and for the cells formed as a result of solution adaptation, its effect on overall computation time will not be very significant. Hence, the simplest algorithm that is the easiest to implement has been chosen. Thus the Liang-Barsky line clipping algorithm has been employed to determine the location of the points that are cut by the input geometry lines.

2.2.2 Liang-Barsky Line Clipping Algorithm

The Liang-Barsky line clipping algorithm (9) tests the extensions of given line segments against each one of the four boundaries of a rectangular clipping window independently, to determine which if any portion of the line segment is inside the clipping window. A line segment with end points V_0 and V_1 which happens to reside wholly within a clipping window is shown in Figure 2.4. The line obtained from the segment and its extensions will be tested with each one of the lines comprising the boundary of the clipping window to determine which portion of the line is visible. After each test the invisible part of the line will be discarded. After all the boundaries are tested, the portion of the line segment that is inside the clipping window will be obtained.

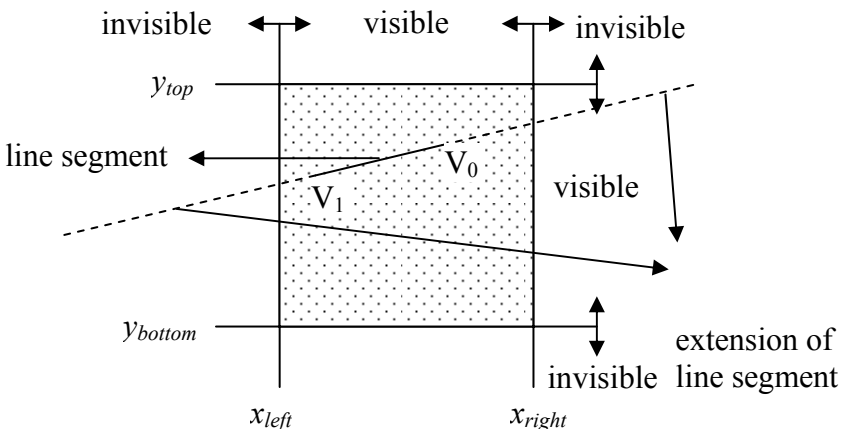

Figure 2.4- The visible and invisible regions for a clipping window

The algorithm makes use of the parametric form of the line segments with end points V_0 (x_0, y_0) and V_1 (x_1, y_1) as given in equations (2.1) to (2.4).

$$x = x_0 + \Delta x \cdot t \tag{2.1}$$

$$y = y_0 + \Delta y \cdot t \tag{2.2}$$

$$\Delta x = x_1 - x_0 \tag{2.3}$$

$$\Delta y = y_1 - y_0 \tag{2.4}$$

Adopting this representation t=0 corresponds to the first end point V_0 and t=1 corresponds to the second end point V_1. The orientation of the line is considered to be from point V_0 to V_1.

Once the line is parameterised, the clipping window can be visualized as the combination of four boundary lines each having a visible and an invisible region as

in Figure 2.4. Ultimately, the intersection of all the visible sides of each boundary line would give visible region for the whole clipping window.

The visible region for the clipping window can be represented in terms of four inequalities using the parametric relations (2.1) to (2.4).

$$\Delta x \cdot t \le x_{right} - x_0 \tag{2.5}$$

$$-\Delta x \cdot t \le x_0 - x_{left} \tag{2.6}$$

$$\Delta y \cdot t \le y_{top} - y_0 \tag{2.7}$$

$$-\Delta y \cdot t \le y_0 - y_{bottom} \tag{2.8}$$

Finally these relationships can be generalized to determine the parametric values corresponding to the segment of the line that resides inside the clipping window.

$$p_i \cdot t \le q_i \qquad i = 1,..,4 \tag{2.9}$$

where

$$p_1 = \Delta x \qquad q_1 = x_{right} - x_0$$

$$p_2 = -\Delta x \qquad q_2 = x_0 - x_{left}$$

$$p_3 = \Delta y \qquad q_3 = y_{top} - y_0$$

$$p_4 = -\Delta y \qquad q_4 = y_0 - y_{bottom}$$

It is observed that when p_i is positive, the orientation of the extended line is from the visible side of a particular boundary line to its invisible side. This will result in an upper limit for the visible portion of the line.

$$t \le \frac{q_i}{p_i} \tag{2.10}$$

When p_i is negative, the orientation of the line is from the invisible side to the visible side, hence a lower bound for the extended line is expected.

$$t \ge \frac{q_i}{p_i} \tag{2.11}$$

Since the portion of the line segment and not the extended line that resides in the clipping window is sought another condition that the bound obtained for t should be between 0 and 1 must also be implemented. Thus for the case when p_i is different than zero; the problem of determining the values of t for which a certain portion of the line segment is within the clipping window becomes a min-max problem in the form as in

$$t \ge t_0 \tag{2.12}$$

$$t \le t_1 \tag{2.13}$$

where

$$t_0 = \max\left(\left\{\frac{q_i}{p_i} \mid p_i < 0, i = 1,2,3,4\right\}, \{0\}\right)$$
$$t_1 = \min\left(\left\{\frac{q_i}{p_i} \mid p_i > 0, i = 1,2,3,4\right\}, \{1\}\right)$$

The t_0 and t_1 values obtained as a result of this min-max problem should satisfy the following equation

$$t_0 \le t \le t_1 \Rightarrow t_0 \le t_1 \tag{2.14}$$

Finally, the case when p_i is zero should be considered. The case p_i equals to zero corresponds to a vertical or a horizontal line. For this case a relationship independent of t is obtained as

$$0 \leq q_i \tag{2.15}$$

The validity of this statement is solely dependent on the value of q_i. If q_i is positive, the line segment is visible for that boundary line else it is invisible. This is referred to as the trivial reject case.

2.3 Mesh Generation

The mesh generation is performed in three main steps. The first one is the uniform mesh generation where a mesh of uniform sized elements of the desired level is obtained. The second one is the box adaptation in which cells around an imaginary box (rectangle) of given dimensions around the input bodies are refined till they reach a desired size. The type of the cells; cut-cell, inside, outside, are determined at this stage. The final step is to refine the cells around the places where there are large gradients on the bodies. The procedure followed is similar to the one outlined in (14).

2.3.1 Uniform Mesh Generation

An initial uniform mesh is formed in the solution domain which will be refined in the later stages to form the mesh on which the solution is to be performed. The reason for forming this initial mesh is to have a prescribed resolution in the outer boundaries of the domain.

Uniform mesh generation is fairly straightforward; starting from the root cell, refinement is performed when the cell level is less than the desired level. If a cell is to be refined, first the level of the edge and vertex neighbours must be investigated. If a neighbour is at a lower level, then that neighbour must be refined prior to the refinement of the cell. In this way, the one level rule is preserved in the process of

mesh generation. The one level rule states that the difference in the levels of two neighbouring cells cannot exceed one. This rule enforces a smooth mesh and also eases the calculations for the fluxes. When a cell is to be refined, it is simply divided into its four quadrants which are its children. Then the level of the children can be set to be one more than that of their parent and their centres can be calculated from the centre coordinate of their parent's, the overall size of the domain, and its level as (2.16) to (2.19)

$$x_c = x_{parent} + \frac{(d/2)}{2^l} \quad , \quad y_c = y_{parent} + \frac{(d/2)}{2^l} \tag{2.16}$$

$$x_c = x_{parent} - \frac{(d/2)}{2^l} \quad , \quad y_c = y_{parent} + \frac{(d/2)}{2^l} \tag{2.17}$$

$$x_c = x_{parent} - \frac{(d/2)}{2^l} \quad , \quad y_c = y_{parent} - \frac{(d/2)}{2^l} \tag{2.18}$$

$$x_c = x_{parent} + \frac{(d/2)}{2^l} \quad , \quad y_c = y_{parent} - \frac{(d/2)}{2^l} \tag{2.19}$$

for the 1st quadrant to 4th quadrant children, respectively. Where d is the domain size and l is the level of the cell.

Once this information is obtained, the neighbours of each cell must also be determined. The procedure followed is similar to the one outlined by De Zeeuw (14). For any cell two edge neighbours and one vertex neighbour will be known automatically since they will be the children of the cell's parent. The other two edge neighbours and one vertex neighbour will be associated with the parent's edge neighbours while the last vertex neighbour will be related to a neighbour of a neighbour of the parent cell. Thus, similar operations will be performed for each group of cells.

The neighbour search can be explained in detail for a first quadrant child exemplifying the process for the other quadrant children. For a first quadrant child,

the first group of neighbours, ones known automatically, will be the west, south and southwest neighbours. They are the second, fourth and the third quadrant children of the cell's parent and they are at the same level. This can be depicted as in Figure 2.5.

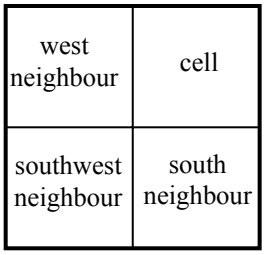

Figure 2.5- Automatically known neighbours of a cell

For the second group of neighbours, associated with the parent's neighbours, the children of the parent's neighbours must be evaluated. For a first quadrant child these are the east and north neighbours of the parent specifically. Due to the one level rule there are three possibilities for these neighbours of the parent; they might be leaf cells hence they are at a lower level than the cell, they might have leaf cell children at the same level as the cell and they might have children with leaf cell children at one level more than the cell. These cases are illustrated in Figure 2.6 for the east neighbour of the parent.

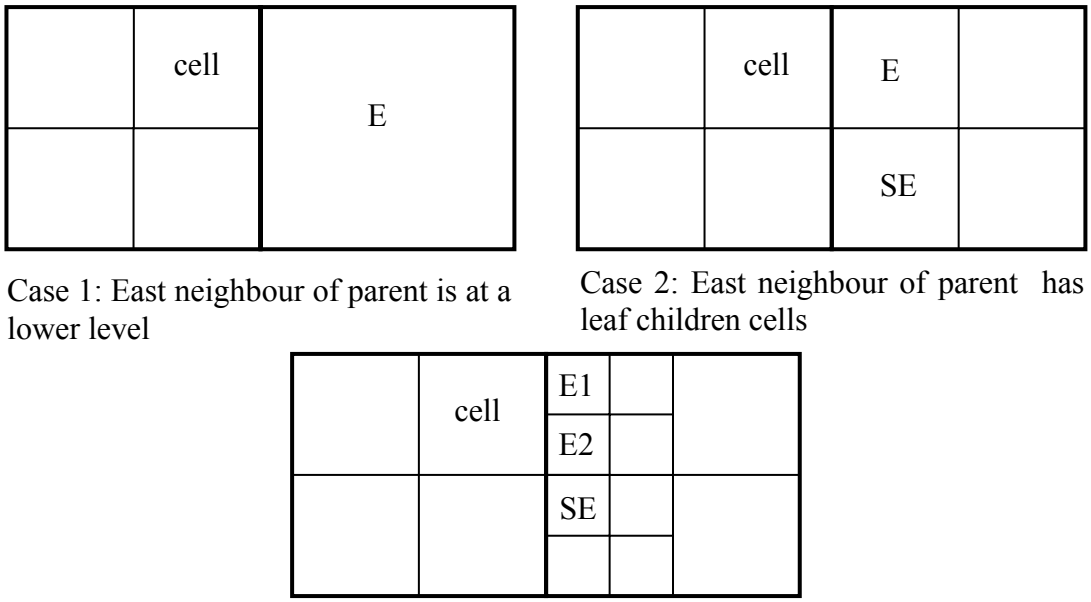

Case 1: East neighbour of parent is at a lower level

Case 2: East neighbour of parent has leaf children cells

Case 3: East neighbour of parent has children with leaf children cells

Figure 2.6- Neighbours associated with the parent cell's edge neighbours

In Case 1, the east neighbour of the cell is directly the east neighbour of the parent and there is no southeast neighbour due to the fact that this cell does not have any children. In Case 2, the east neighbour is the second quadrant child of the parent's east neighbour while the southeast neighbour is the third quadrant child of the parent's east neighbour. In Case 3, there are two actual east neighbours; the second and third quadrant children of the parent's east neighbour's second quadrant child. Since it is not desirable to complicate the data structure by storing the east neighbours separately, their parent, the second quadrant child of the cell's parent's east neighbour, is stored as the east neighbour. During the calculations it is always checked to see if a neighbour has children to identify the cells that are marked as E1 and E2 in Figure 2.6. Following the same convention, the third quadrant child of the cell's parent's east neighbour is stored as the southeast neighbour even though the second quadrant child of this cell stored is the only actual southeast neighbour. Hence, it can be said that, as a general rule, the cell stored as the neighbour will be either at a lower level than the cell or it will be at the same level.

With similar reasoning, the north neighbour of a first quadrant child will be its parent's north neighbour when this cell is a leaf cell, in which case there will be no distinct northwest neighbour. When the cell's parent's north neighbour has children, the fourth and the third quadrant children of this cell will be stored as the north and the northwest neighbours of the cell regardless of them having children.

The only remaining neighbour for the first quadrant child is the northeast neighbour. This neighbour is the north neighbour of the parent's east neighbour if this cell has no children otherwise it is the third quadrant child of this cell. The same search is also performed through the north neighbour of the parent in case its east neighbour resides within an input geometry. In this case, this neighbour is the east neighbour of the parent's north neighbour if this cell has no children; otherwise it is the third quadrant child of this cell.

With the same line of reasoning, the rules for determining each neighbour of any quadrant child can be devised.

2.3.2 Box Adaptation & Cell-types

The next step in mesh generation is the box adaptation. Box adaptation will allow the mesh to have a desired resolution in regions around the input geometries. This step consists of two stages for input geometries that are comprised of more than one body. The first step is to refine cells that are in contact with an imaginary rectangular box around the collection of the bodies, while the second step is to refine the cells that are in contact with rectangular boxes around individual bodies until the input size criterion for each body is satisfied. The rectangular box around each one of the bodies spans from the minimum to maximum coordinate of a specific body in both of the Cartesian directions which will be used in the second stage of the box adaptation. Similarly a rectangular box around the collection of the bodies can be formed. This box is then stretched by an input proportion. The latter described imaginary boxes for a three element airfoil configuration can be depicted as in the figure below.

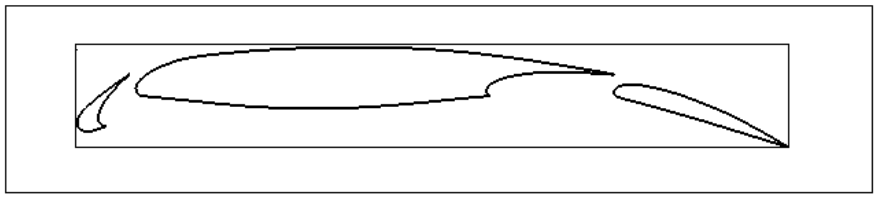

Figure 2.7- Imaginary boxes around a three element airfoil

For the first stage of box adaptation, the outer box depicted in Figure 2.7 is used. Any cell that is in contact with the box is refined until the resulting leaf cells satisfy the largest one of the input refinement criterion for each body. The input refinement criteria for each body denote the maximum size of a cell as a proportion of the maximum dimension of that body. In the first stage of box adaptation, this largest criterion is taken to be the proportion of the maximum dimension of the collection of bodies. The maximum dimensions are the larger of the differences of the maximum and minimum x or y coordinates of a body or the collection of all bodies.

In the second stage, the cells that are in contact with the boxes around each body is refined until the given refinement criterion for that body is satisfied. The second stage allows the mesh to have differing resolutions around each body. Figure 2.8 illustrates how a mesh of different resolutions around the slat and the airfoil is obtained by applying the second stage of box adaptation.

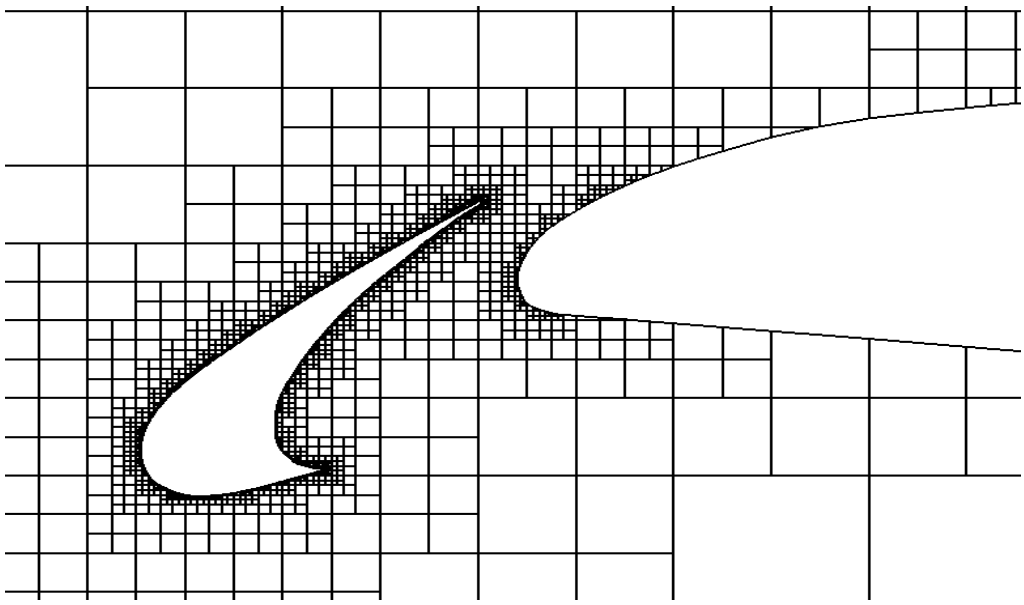

Figure 2.8- Mesh around the slat and the airfoil

After the box adaptation, the next step in mesh generation is curvature adaptation. But before the curvature adaptation, the cells that are cut by the geometry lines must be determined. All the cells in the mesh will be marked as one of the types outside, inside or cut-cell. For the cut-cells, information regarding the edges cut by the geometry and the portions of the edges through which fluxes pass must be stored.

To determine the cell types, first the relative location of each cell with respect to the large box around the collection of the bodies used for box adaptation is employed. The cells that are in contact with this box have the possibility of being inside or outside the bodies or they might be cut by one of the bodies. Line clipping discussed earlier is performed to determine the exact configuration. Through line clipping, the line portions that cut the cell will be determined if the cell is cut. A cell that is cut by only one geometry line is a regular cut-cell and it can be handled easily. However a cell cut by more than one line must be converted to either a regular cut-cell, an outside or an inside cell by means of modifying the body.

2.3.2.1 Regular Cut-cells

Regular cut-cells are the ones that are cut by only one geometry line portion. For these cells, the coordinates of the end points of the cutting geometry line will be known after the line clipping process. The only remaining thing is to determine on which edges these points lay and through which portion of each edge the flux passes through. In other words through which portion of the edge the cell exchanges information with another neighbour cell. Before going any further, the naming convention of the edges and the corners can be defined as in Figure 2.9.

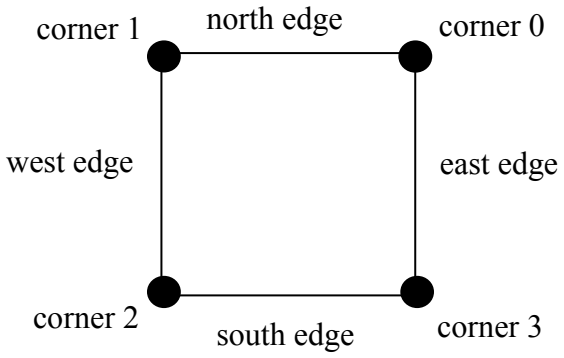

Figure 2.9- Naming convention of a cell

The first step is to detect a special subgroup of regular cut-cells, the ones with the geometry line lying on one of the edges of the cell. If the *x* coordinates of both of the cutting end points are equal then there is a chance that the line comprising of these points lays on one of the east or the west edges. Hence if the *x* coordinate of one of the cutting end points is equal to the *x* coordinate of corner 0, then it means that the line lays on the east face, in which case the edge cut is stored as *east* and no information is stored for the flux. If the *x* coordinate of one of the cutting end points is equal to the *x* coordinate of corner 2 then it means that the line lays on the west face, in which case the edge cut is stored as *west* and no information is stored for the flux once again. A similar check is also performed on the *y* coordinates of the cutting

edge; if they are equal to each other and to one of the *y* coordinates of corner 0 or corner 2, then the edge cut is stored as *north* or *south* respectively and no flux information is stored. Thus for the special subgroup of regular cut-cells only one edge is marked as cut while no information on the flux is stored.

Once the subgroup of special cells is detected the information for the other regular cut-cells can be determined by edge based tests. Starting from the east edge and going counter-clockwise, it is checked whether any of the edges is cut by one of the end points of the geometry line or not. For the east face, it is checked whether the *x* coordinates of the end points of the line are equal to the *x* coordinate of corner 0. If one of them is equal then the east edge is marked as being cut, making corner 0, corner 3 and any point in between along the east edge a candidate for the location of the cutting end point. To determine the flux information, a point along the east edge whose location relative to the cutting end point is known must be tested to see if it is inside the body or outside it. The inside-outside test employed is based on the simple point location test described in (15). The two possible points are corner 0 and corner 3. If the cutting end point is not on corner 0 this point is tested. If it is outside, the flux for the east edge is marked as *larger* indicating that the flux passes through the portion of the east edge with *y* coordinates greater than the one of the cutting end point. Otherwise *smaller* is stored for the east face flux indicating that the flux passes through the portion of the east edge with *y* coordinates less than the one of the cutting end point. If the cutting end point is on corner 0 then corner 3 is tested and if it is outside *smaller* is stored if it is inside *larger* is stored. If the east edge is not cut then the centre of the edge is put to the inside-outside test, and if this point is outside any of the bodies then the flux information is stored as *all*, indicating that the flux passes through the whole face and otherwise it is stored as *none*, indicating that no flux passes through the face.

Once the configuration of the east face is determined it is checked whether any of the cutting end points lay on the north face. If a point is detected to be on the north face the possible locations for it are either corner 1 or anywhere along the north edge between corner 0 and corner 1. For the inside-outside test corner 0 is used since it is already known that the cutting edge cannot be on this point. If corner 0 is outside,

then the flux is stored as *larger*, meaning that it passes through the portion of the edge with x coordinates greater than the cutting edge otherwise *smaller* is stored indicating that flux passes through the portion with x coordinates less than that of the cutting edge. If the north edge is not cut then the centre of the edge is tested to see if the flux passes through the whole face or it doesn't pass at all.

After the north face the west face is examined. If this edge is cut, corner 1 is sent to the inside-outside test as the only point along west edge on which the cutting end point may not lay. The flux information is stored as *larger* if this point is outside otherwise it is stored as *smaller*. If the edge is not cut, the centre of the edge is tested to see if the flux passes through the face.

Finally, if the south face is cut either one of the corner 2 and corner 3 can be tested to fill the flux information accordingly. If the edge is not cut, the centre of the edge is tested to see if the flux passes through the face. In Figure 2.10, exemplifying cases for regular cut-cells are illustrated.

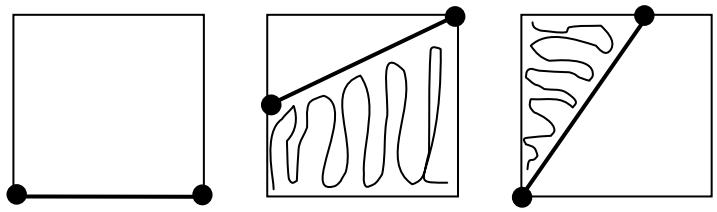

Figure 2.10- Examples of regular cut-cells

In Figure 2.10, the scribbled parts represent the portion of the cell that is occupied by a body. Case 1 is an example of the special subgroup of regular cells. In this particular example the only cut edge is stored as the south edge and no flux information is stored. In Case 2 the cut edges are detected as the east and west edges. For the east face, the flux information is stored as *larger* even though no flux passes through the face. The north flux information is *all* while for the west face it is *larger*

and for the south face it is *none*. In Case 3, the edges cut are the north and west edges. The flux information for the east and the south faces are *all*, it is *larger* for the north face and *smaller* for the west face.

2.3.2.2 Irregular Cut-cells

The cut-cells that are cut by more than one geometry line are termed as irregular cut-cells. To convert these cells into regular cut-cells, refinement is the first measure taken. The cells that are cut by more than two geometry lines and those that are cut by two lines that do not have a common end point are refined until their children are cells of acceptable types or until they are refined to the maximum allowable level in the mesh. It can safely be said that there will be no cells cut by more than two geometry lines as a result of this refinement process, since the maximum level a cell can reach will make it much smaller than the dimensions of the body. The cells that are cut by two lines that do not have a common end point will eventually become regular cut-cells if they are refined unconditionally. But sometimes they will require very extensive refinement reaching levels much higher than the maximum allowable one especially in the presence of very acute angles. These cases along with the cells that are cut by two lines that have a common end point are treated separately.

In contrast to the other types, cells that are cut by two lines that have a common end point are not refined unconditionally until they reach the maximum allowable level. Instead they are refined, only when their distinct end points lay on the same face of the cell as in Case 2 and Case 5 of Figure 2.11. The reason for this is that since the bodies are represented as lines with specified end points, there would be a clustering of highly refined cells around each of the specified points if these cells were to be refined unconditionally. Those cells that are refined, the ones that have their distinct end points on the same edges, are tested to see if they are concave or convex. If they are convex, then they are simply converted to inside cells as in Case 2 of Figure 2.11.

At the end of this refinement process, the cells that were not converted are classified into two groups; convex-united and concave-split and treated accordingly. The first

group is formed of cells that are cut by two lines without a common end point with a single convex area (Case 3 of Figure 2.11), and the cells that are cut by two lines with a common end point with the distinct end points on separate edges forming a single convex cell area (Case 4 of Figure 2.11). The second group of cells are the ones that are cut by two lines without a common end point with two separate convex cell areas (Case 5 of Figure 2.11), cells that are cut by two lines with a common end point forming a single concave area (Case 6 of Figure 2.11). The grouping and the treatment of the irregular cut-cells can be depicted as in Figure 2.11.

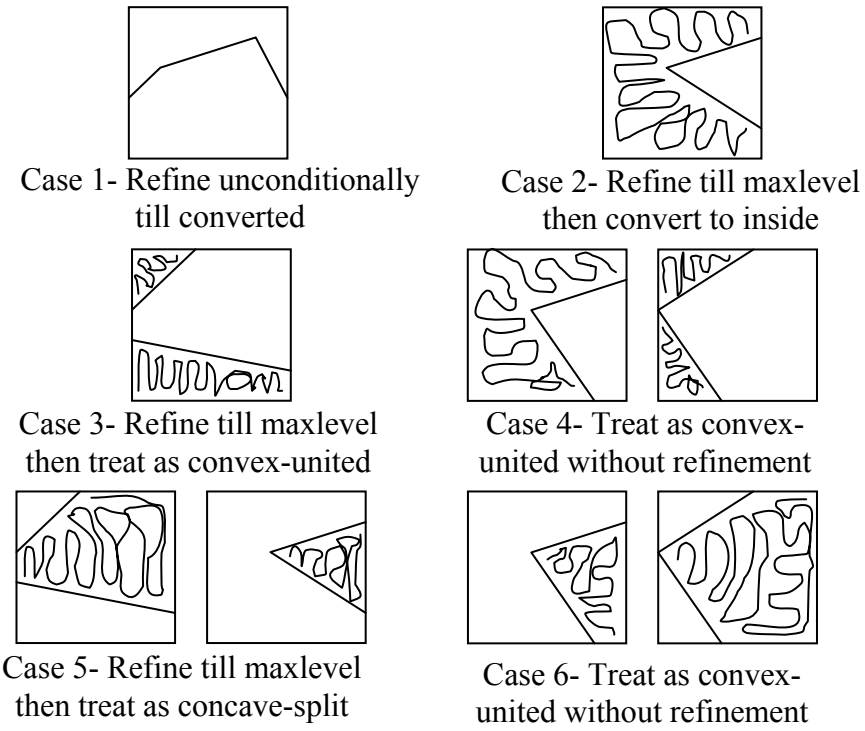

Figure 2.11- Grouping and treatment of irregular cut-cells

2.3.2.2.1 Concave-Split

The concave-split cells are converted to regular cut-cells by making modifications on the body. The location of the end points on the edges and the direction towards which the lines converge is of essential importance in the conversion process. The basic idea is to trim the body towards the direction in which the cutting lines

converge. Hence the geometry line cutting the cell will be the connection of the end points in the diverging direction. The direction towards which the lines converge can be determined by placing one coordinate of the end points of a line to the equation of the other line to obtain the corresponding other coordinate. Then the line converges towards the direction in which the difference between the calculated coordinate and the coordinate of the end point is smaller. This can be represented more clearly graphically as in Figure 2.12.

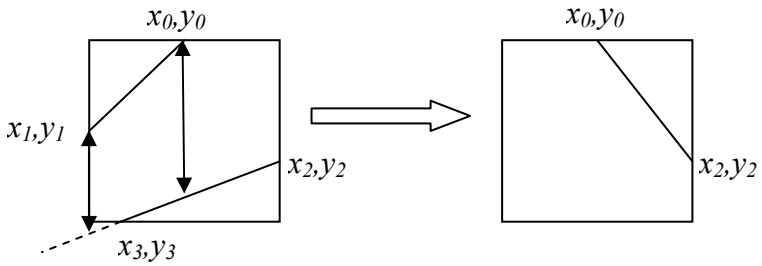

Figure 2.12- Conversion of an irregular cut-cell

The criterion for the above conversion is expressed mathematically in the following equation.

$$\left| y_0 - \left[\frac{(x_2 - x_0)}{(x_2 - x_3)} (y_3 - y_2) + y_2 \right] \right| > \left| y_1 - \left[\frac{(x_2 - x_1)}{(x_2 - x_3)} (y_3 - y_2) + y_2 \right] \right| \qquad (2.20)$$

This trimming process will result in obtaining a member of the special subgroup of regular cut-cells in some cases, while regular cut-cells are obtained in some cases. The special subgroup will be obtained for cells that are cut by lines with a common end point having their distinct end points on the same edge, cells having two pairs of end points on the same edge and cells that have one pair of end points on the same edge while converging towards the end points that are on different edges. These cases and their conversion are illustrated in Figure 2.13.

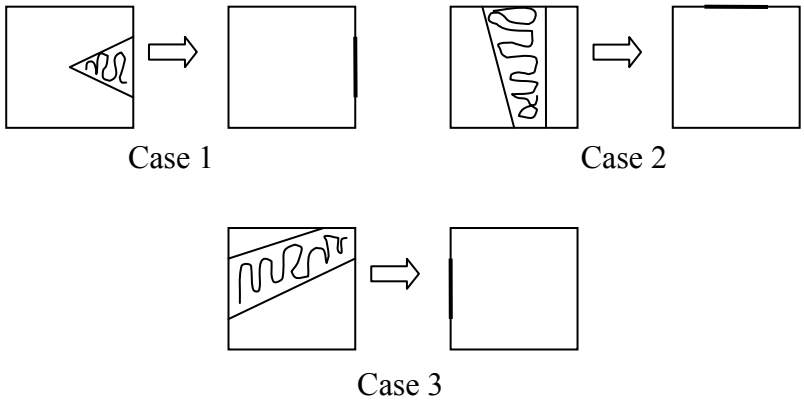

Figure 2.13- Concave-split to special subgroup of regular cut-cells conversion

In Case 1 of Figure 2.13, since there is a common end point, the remaining end points will be connected to obtain a cell that is cut on its east edge. In Case 2, there are two pairs of end points that are on the same edge. In this case since the lines diverge towards the north face, this face will be marked as being cut. In Case 3, there is one pair of end points on the same face. Since the lines diverge towards this face, the west face is marked as being cut.

The cells that convert into regular cut-cells as in Figure 2.14 are the ones that have common cutting end points with the other end points on different edges, cells with all cutting end points on different edges, and the cells that have one pair of end points on different edges converging towards a pair of end points that are on the same edge.

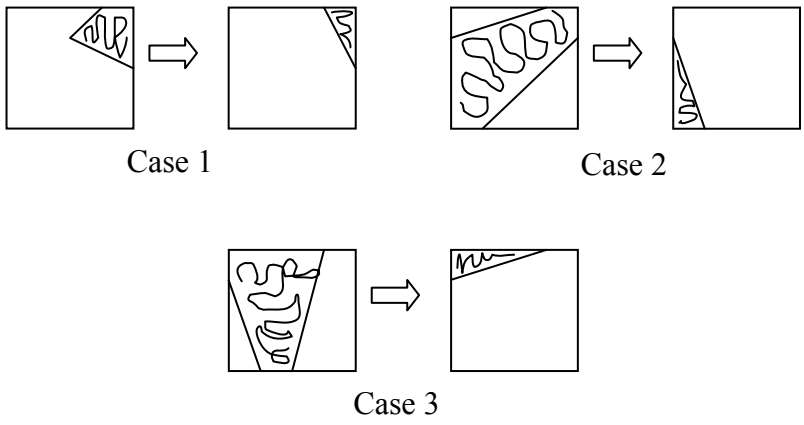

Figure 2.14- Concave-split to regular cut-cells conversion

In Case 1 of Figure 2.14, there is a common end point and the other end points are connected automatically to form a regular cut-cell. In Case 2, all the end points are on distinct edges. Since the distance between the ones on the west and the south edges is greater than the distance between the others the cut locations on these edges are connected to form a regular cut-cell. In Case 3, since the lines diverge towards the end points that are on different edges in contrast to Case 3 of Figure 2.13, a regular cut-cell is formed by the connection of the cut location on these edges.

2.3.2.2.2 Convex-United

The procedure followed for the convex-united cells are similar to the ones for concave-split cells. Once again the end points towards which the cutting lines diverge are connected to form the new cutting edge. In the case of the convex-united cells conversion is made to either an inside cell or to a regular cut-cell. The cells that have two pairs of cutting end points on the same faces, and the cells that have a pair of end points on the same edge with the lines converging towards the end points that are on different edges are converted to inside cells. These cases are illustrated in Figure 2.15.

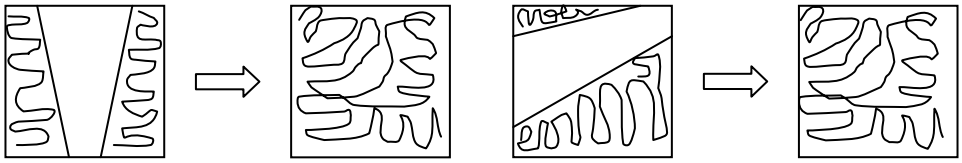

Case 1 Case 2

Figure 2.15- Convex-united to inside cells conversion

Case 1 and Case 2 of Figure 2.15 are analogous to those presented in Figure 2.13. With the difference that they convert to inside cells, and there is no special sub-group of inside cells.

The cells that are converted to regular cut-cells are the ones that have common cutting end points with the other end points on different edges, cells with all cutting end points on different edges, and the cells that have one pair of end points on different edges converging towards a pair of end points that are on the same edge. These cases are illustrated in Figure 2.16.

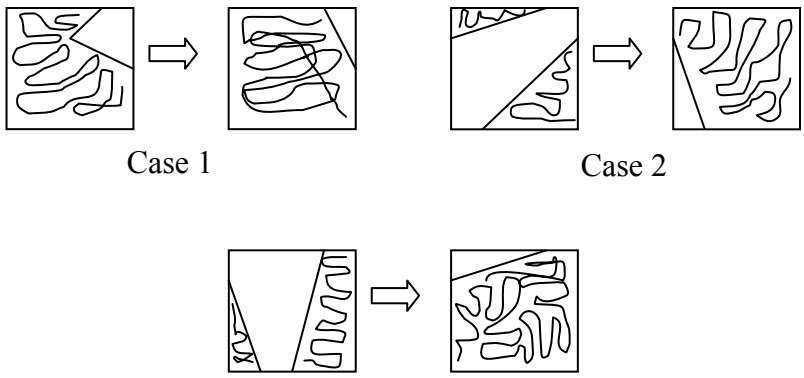

Case 1 Case 2

Case 3

Figure 2.16- Convex-united to regular cut-cells conversion

The Case 1, Case 2 and Case 3 of Figure 2.16 are analogous to those in Figure 2.14. The difference between them is the portions of the cells that are marked as inside and outside are opposite in these cases.

Since each irregular cell is converted individually into a cut-cell, at the end of the process some cut-cells that are not part of any body will be obtained. Hence, at the end of the conversion process, the mesh has to be traversed to find these unconnected cells and convert them into either outside cells, if they were processed as concave-split cells, or into inside cells if they were treated as convex-united cells.

2.3.3 Curvature Adaptation

The last step in the mesh generation process is the curvature adaptation. The purpose of the curvature adaptation is to ensure that regions of a body that have high curvatures are resolved enough to be represented accurately and also since these regions will be associated with high gradients.

In curvature adaptation, the cutting edges of neighbouring cut-cells are evaluated to decide on whether to refine a cell or not. So firstly neighbouring cut-cells should be detected then curvature must be quantified to develop a criterion for refinement. In order to quantify the curvature, the angle between the normals of the cutting edges pointing towards the fluid domain is used. If this quantity exceeds a threshold value then the cell is refined. This can be illustrated as in Figure 2.17.

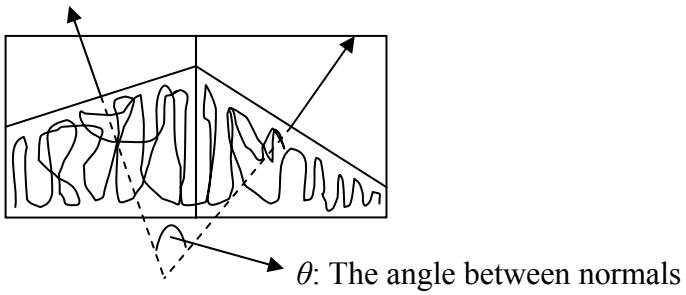

Figure 2.17- The normals of two neighbouring cut-cells

The normal for a cutting edge of a cell can be determined through the flux information stored for a cut edge.

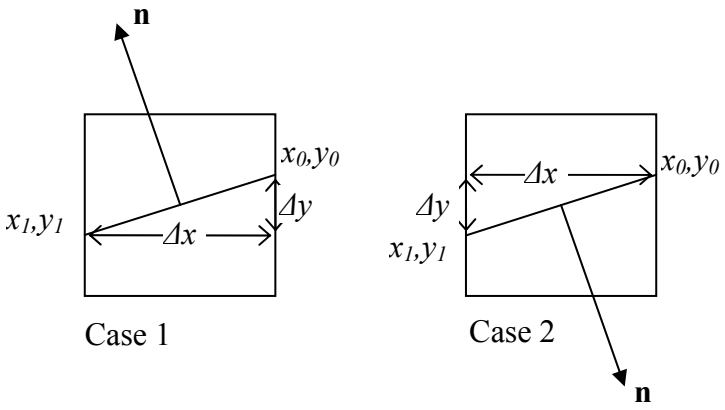

Figure 2.18- Calculation of the normal

In Case 1 of Figure 2.18, the first edge that is cut is the east edge and the flux information associated is *larger*. In this case, the normal is given by the following equation.

$$\vec{n} = -\Delta y\vec{i} + \Delta x\vec{j} = -(y_0 - y_1)\vec{i} + (x_0 - x_1)\vec{j} \qquad (2.21)$$

In Case 2, the first edge cut is east as in the previous case but this time the associated flux information is *smaller* making the normal;

$$\vec{n} = \Delta y\vec{i} - \Delta x\vec{j} = (y_0 - y_1)\vec{i} - (x_0 - x_1)\vec{j} \tag{2.22}$$

Hence, it is possible to express each normal pointing to the fluid domain using the first edge cut and the flux information associated with it for the neighbouring cells. Then, a relation for the angle between the normals can be obtained by their dot multiplication as

$$\vec{n}_1 \bullet \vec{n}_2 = n_{1x}n_{2x} + n_{1y}n_{2y} = |\vec{n}_1||\vec{n}_2|\cos\theta \Rightarrow \cos\theta = \frac{(n_{1x}n_{2x} + n_{1y}n_{2y})}{|\vec{n}_1||\vec{n}_2|} \tag{2.23}$$

Then a cell is to be refined, if this θ value is greater than a threshold value.

$$\cos\theta = \frac{(n_{1x}n_{2x} + n_{1y}n_{2y})}{|\vec{n}_1||\vec{n}_2|} < \cos\theta_{th} \tag{2.24}$$

CHAPTER 3

NUMERICAL METHOD

3.1 Governing Equations

In the code developed, solution to the compressible Euler equations in the conserved form is sought. Hence, the governing equations can be represented as

$$\frac{\partial}{\partial t}\iiint \mathbf{U} dV + \oiint \mathbf{F} \bullet \vec{n} dA = 0 \tag{3.1}$$

where, $\mathbf{U}$ and $\mathbf{F}$ are the vectors of conserved variables and the flux respectively, while $\vec{n}$ is the normal to the differential area element dA. This equation can be descritised in 2-D as

$$\frac{\partial \mathbf{U}}{\partial t} + \frac{1}{A_{cell}} \sum_{edges} \mathbf{F} \bullet \vec{n} \Delta s = 0 \tag{3.2}$$

$\vec{n}$ being the face normal, Δs the edge length and A_{cell} the cell area. The vector of conserved variables and the flux vector can be written as

$$\mathbf{U} = \begin{bmatrix} \rho \\ \rho u \\ \rho v \\ \rho e_t \end{bmatrix} \qquad \mathbf{F} \bullet \vec{n} = \begin{bmatrix} \rho u \cos\theta + \rho v \sin\theta \\ \rho u^2 \cos\theta + \rho uv \sin\theta + p\cos\theta \\ \rho v^2 \sin\theta + \rho uv \cos\theta + p\sin\theta \\ \rho u h_t \cos\theta + \rho v h_t \sin\theta \end{bmatrix} \tag{3.3}$$

In this equation θ is the angle between the normal direction of the edge and the Cartesian x-direction. The variables ρ, u, v, p, e_t and h_t are the density, velocity in

the x and y direction, the pressure, the total energy and the total enthalpy respectively.

In the solution method used, determination of the fluxes through the faces of the cells require a pseudo one dimensional form of the flux vector represented in Equation (3.3). This form will be equivalent to the Euler equations written in terms of the normal and tangential velocities. At this point, the rotational invariance of the Euler equations (16) can be employed as

$$\mathbf{F}\bullet\vec{n} = \mathbf{T}^{-1}\mathbf{F}(\mathbf{TU}) = \mathbf{T}^{-1}\hat{\mathbf{F}}(\hat{\mathbf{U}}) \tag{3.4}$$

The transformation matrix and its inverse; $\mathbf{T}$ and $\mathbf{T}^{-1}$, appearing in Equation (3.4) can be written explicitly as

$$\mathbf{T} = \begin{bmatrix} 1 & 0 & 0 & 0 \\ 0 & \cos\theta & \sin\theta & 0 \\ 0 & -\sin\theta & \cos\theta & 0 \\ 0 & 0 & 0 & 1 \end{bmatrix} \quad \mathbf{T}^{-1} = \begin{bmatrix} 1 & 0 & 0 & 0 \\ 0 & \cos\theta & -\sin\theta & 0 \\ 0 & \sin\theta & \cos\theta & 0 \\ 0 & 0 & 0 & 1 \end{bmatrix} \tag{3.5}$$

Hence, the conserved quantities and the flux vector in terms of normal and tangential velocities can be given

$$\hat{\mathbf{U}} = \begin{bmatrix} \rho \\ \rho\hat{u} \\ \rho\hat{v} \\ \rho e_t \end{bmatrix} \qquad \hat{\mathbf{F}}(\hat{\mathbf{U}}) = \begin{bmatrix} \rho\hat{u} \\ \rho\hat{u}^2 + p \\ \rho\hat{u}\hat{v} \\ \rho\hat{u}h_t \end{bmatrix} \tag{3.6}$$

In Equation (3.6) $\hat{u}$ and $\hat{v}$ are the normal and tangential velocities, while $\hat{\mathbf{U}}$ and $\hat{\mathbf{F}}$ are the vectors of conserved variables and the flux, in terms of the normal and tangential velocities. The normal and the tangential velocities can be expressed in terms of the Cartesian velocities as

$$\hat{u} = u\cos\theta + v\sin\theta, \quad \hat{v} = -u\sin\theta + v\cos\theta \tag{3.7}$$

Using this transformation, the governing equations can be expressed as

$$\frac{\partial \mathbf{U}}{\partial t} + \frac{1}{A_{cell}} \sum_{edges} \mathbf{T}^{-1} \hat{\mathbf{F}}(\hat{\mathbf{U}}) \Delta s = 0 \tag{3.8}$$

The general solution strategy is to estimate the flux in terms of the normal and tangential directions, rotate them to Cartesian coordinates with the inverse transformation matrix for each face, and then use an appropriate method for time integration.

3.2 One Dimensional Riemann Problem for Linear Systems

Before discussing the solution algorithm for the Euler equations, the one dimensional Riemann problem for a linear system of equations should be discussed (17) (16). The model equation for the one dimensional linear system is represented by Equation (3.9). This equation is linear if the Jacobian of the flux vector is comprised of constant elements, that is

$$\frac{\partial \mathbf{U}}{\partial t} + \frac{\partial \mathbf{F}}{\partial x} = \frac{\partial \mathbf{U}}{\partial t} + \frac{\partial \mathbf{F}}{\partial \mathbf{U}} \frac{\partial \mathbf{U}}{\partial x} = \frac{\partial \mathbf{U}}{\partial t} + \mathbf{A} \frac{\partial \mathbf{U}}{\partial x} = 0 \tag{3.9}$$

where $\mathbf{A}$ is the Jacobian matrix. The initial conditions for the model equation are given as

$$\mathbf{U}(x,0) = \begin{cases} \mathbf{U_L} & x_0 < 0 \\ \mathbf{U_R} & x_0 > 0 \end{cases} \tag{3.10}$$

where subscripts **L** and **R** refer to the left and right states respectively. The first step in the solution process is to diagonalize the Jacobian matrix using the **Q** matrix appearing in the following equation. Each column of this matrix is a right eigenvector of the Jacobian matrix and the rows of its inverse are the left eigenvectors of the Jacobian matrix (18). The elements of the resulting diagonal matrix $\mathbf{\Lambda}$ are the eigenvalues of the Jacobian matrix.

$$\mathbf{Q}^{-1}\mathbf{A}\mathbf{Q} = \mathbf{\Lambda} \tag{3.11}$$

Using this diagonalization and multiplying Equation (3.9) by $\mathbf{Q}^{-1}$, the linear set of equations can be converted to a set of independent equations in terms of the new characteristic variable vector $\mathbf{V}$.

$$\mathbf{Q}^{-1}\frac{\partial \mathbf{U}}{\partial t} + \mathbf{Q}^{-1}\mathbf{A}\mathbf{Q}\mathbf{Q}^{-1}\frac{\partial \mathbf{U}}{\partial x} = \frac{\partial \mathbf{V}}{\partial t} + \mathbf{\Lambda}\frac{\partial \mathbf{V}}{\partial x} = 0 \tag{3.12}$$

The relation between the characteristic variables and the conserved quantities in Equation (3.12) can be defined as

$$\mathbf{Q}^{-1}\partial \mathbf{U} = \partial \mathbf{V} \tag{3.13}$$

Since this is a linear system and the elements of $\mathbf{Q}^{-1}$ are constant, Equation (3.13) can be written in an alternative form as

$$\mathbf{Q}^{-1}\mathbf{U} = \mathbf{V} \Rightarrow \mathbf{Q}^{-1}\Delta\mathbf{U} = \Delta\mathbf{V} \tag{3.14}$$

where;

$$\Delta\mathbf{V} = \mathbf{V_R} - \mathbf{V_L} \qquad \Delta\mathbf{U} = \mathbf{U_R} - \mathbf{U_L}$$

After the diagonalization, the governing equations obtained in terms of the characteristic variables, λ 's, in Equation (3.12) can be written explicitly as

$$\begin{bmatrix} v_1 \\ . \\ . \\ . \\ v_n \end{bmatrix}_t + \begin{bmatrix} \lambda_1 & 0 & . & . & 0 \\ 0 & . & & & . \\ . & & . & & . \\ . & & & . & 0 \\ 0 & . & . & 0 & \lambda_n \end{bmatrix} \begin{bmatrix} v_1 \\ . \\ . \\ . \\ v_n \end{bmatrix}_x = 0 \tag{3.15}$$

The equations represented by Equation (3.15) are *n* independent equations for the *n* characteristic variables. In other words, *n* independent scalar equations are obtained for *n* characteristic variables, v's , (17) as

$$\frac{\partial v_i}{\partial t} + \lambda_i \frac{\partial v_i}{\partial x} \qquad i = 1, ..., n \tag{3.16}$$

For the solution of each one of the equations in Equation (3.16), the definition of the total derivative is employed as

$$\frac{\mathrm{d}v_i}{\mathrm{d}t} = \frac{\partial v_i}{\partial t} + \frac{\partial v_i}{\partial x}\frac{\mathrm{d}x}{\mathrm{d}t} \tag{3.17}$$

Hence with the application of the condition presented in Equation (3.18), a straight line along which the characteristic variable remains constant and the governing equation is satisfied, is obtained.

$$\frac{\mathrm{d}x}{\mathrm{d}t} = \lambda_i \Rightarrow \frac{\mathrm{d}v_i}{\mathrm{d}t} = 0 \text{ along line } x = x_0 + \lambda_i t \tag{3.18}$$

The solution obtained in terms of the characteristic lines can be represented graphically as in Figure 3.1.

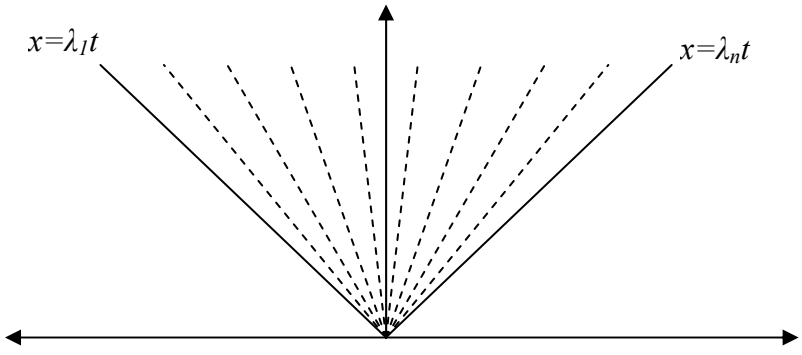

Figure 3.1- Solution of a 1-D Riemann problem for a set of linear equations

In Figure 3.1, when one of the characteristic lines is crossed the respective value of the characteristic variable changes conforming to the given initial conditions. The form in which the solution is presented is of crucial importance in the development of numerical methods while it doesn't make a difference in the analytical sense. Hence the solution can be presented in several formats (17). First representation is in terms of the characteristic variables as

$$\mathbf{V}\left(\frac{x}{t}\right)=\begin{cases}\mathbf{V_L}=\mathbf{V_R}-\Delta\mathbf{v_1}-\ldots-\Delta\mathbf{v_n} & x/t<\lambda_1<\ldots<\lambda_n\\ \mathbf{V_L}+\Delta\mathbf{v_1}=\mathbf{V_R}-\Delta\mathbf{v}_2-\ldots-\Delta\mathbf{v_n} & \lambda_1<x/t<\lambda_2<\ldots<\lambda_n\\ \quad\vdots & \quad\vdots\\ \mathbf{V_L}+\Delta\mathbf{v_1}+\ldots+\Delta\mathbf{v_n}=\mathbf{V_R} & \lambda_1<\ldots<\lambda_n<x/t\end{cases} \tag{3.19}$$

The difference vectors appearing in Equation (3.19) can be written explicitly as

$$\Delta\mathbf{v_1}=\begin{bmatrix}\Delta v_1\\0\\\vdots\\0\end{bmatrix}\quad\Delta\mathbf{v_i}=\begin{bmatrix}0\\\vdots\\\Delta v_i\\\vdots\\0\end{bmatrix}\quad\Delta\mathbf{v_n}=\begin{bmatrix}0\\\vdots\\0\\\Delta v_n\end{bmatrix}\Rightarrow\Delta v_1+\ldots+\Delta v_n=\Delta\mathbf{V} \tag{3.20}$$

It is possible to express the solution in terms of the conserved variables as well by employing the relation between the characteristic variables and the conserved variables given in Equation (3.14). Here it should be remembered that each column of matrix **Q** is an eigenvector of the Jacobian matrix. This will promote the relation presented in the following equation

$$\mathbf{Q}\Delta\mathbf{v_i}=\mathbf{r_i}\Delta v_i \tag{3.21}$$

where $\mathbf{r_i}$ is the i^{th} eigenvector of the Jacobian matrix.

Hence by multiplying Equation (3.19) by the matrix **Q,** the solution in terms of the conserved variables is obtained as

$$\mathbf{U}\left(\frac{x}{t}\right)=\begin{cases}\mathbf{U_L}=\mathbf{U_R}-\mathbf{r_1}\Delta v_1-\ldots-\mathbf{r_n}\Delta v_n & x/t<\lambda_1<\ldots<\lambda_n\\ \mathbf{U_L}+\mathbf{r_1}\Delta v_1=\mathbf{U_R}-\mathbf{r}_2\Delta v_2-\ldots-\mathbf{r_n}\Delta v_n & \lambda_1<x/t<\lambda_2<\ldots<\lambda_n\\ \quad\vdots & \quad\vdots\\ \mathbf{U_L}+\mathbf{r_1}\Delta v_1+\ldots+\mathbf{r_n}\Delta v_n=\mathbf{U_R} & \lambda_1<\ldots<\lambda_n<x/t\end{cases} \tag{3.22}$$

At this point, it should be noted that for the numerical method that is used for the solution of the Euler equations, the flux at a face of a certain cell will be of interest rather than the value of the conserved variable. It should also be noted that the flux vector appearing in the differential model equation is equivalent to the flux term that would appear in its integral formulation. Also the fluxes of each face will be investigated separately so the x/t can be considered to be zero for the respective face of the cell. Taking these points into consideration one can derive expressions for the fluxes as a solution.

$$\mathbf{F}(0)=\begin{cases}\mathbf{AU_L}=\mathbf{AU_R}-\mathbf{r_1}\lambda_1\Delta v_1-\ldots-\mathbf{r_n}\lambda_n\Delta v_n & 0<\lambda_1<\ldots<\lambda_n\\ \mathbf{AU_L}+\mathbf{r_1}\lambda_1\Delta v_1=\mathbf{AU_R}-\mathbf{r}_2\lambda_2\Delta v_2-\ldots-\mathbf{r_n}\lambda_n\Delta v_n & \lambda_1<0<\lambda_2<\ldots<\lambda_n\\ \quad\vdots & \quad\vdots\\ \mathbf{AU_L}+\mathbf{r_1}\lambda_1\Delta v_1+\ldots+\mathbf{r_n}\lambda_n\Delta v_n=\mathbf{AU_R} & \lambda_1<\ldots<\lambda_n<0\end{cases} \tag{3.23}$$

Equation (3.23) has been obtained by exploiting the fact that $\mathbf{Ar_i}=\lambda_i\mathbf{r_i}$.

Even though Equation (3.23) is a perfectly valid representation of the solution, it is desirable to present the solution in a more compact form as in one of the following equivalent forms:

$$\mathbf{F}(0) = \mathbf{A}\mathbf{U}_{\mathbf{L}} + \sum_{i=1}^{n} \mathbf{r_i} \lambda_i^{-} \Delta v_i$$
$$\mathbf{F}(0) = \mathbf{A}\mathbf{U}_{\mathbf{R}} - \sum_{i=1}^{n} \mathbf{r_i} \lambda_i^{+} \Delta v_i \tag{3.24}$$

where;

$$\lambda_i^{-} = \min(0, \lambda_i)$$
$$\lambda_i^{+} = \max(0, \lambda_i)$$

Since the representation is dependent on the sign of the eigenvalues in Equation (3.24), a final form for the solution can be obtained by averaging the equivalent solutions appearing in Equation (3.24).

$$\mathbf{F}(0) = \underbrace{\frac{1}{2}\mathbf{A}(\mathbf{U}_{\mathbf{L}} + \mathbf{U}_{\mathbf{R}})}_{\frac{1}{2}[\mathbf{F}(\mathbf{U}_{\mathbf{L}}) + \mathbf{F}(\mathbf{U}_{\mathbf{R}})]} - \frac{1}{2}\sum_{i=1}^{n} \mathbf{r_i} \left|\lambda_i\right| \Delta v_i \tag{3.25}$$

3.3 The Approximate Riemann Solver of Roe

The flux term in the governing Euler equations in the integral form (3.1) can be estimated by considering the *x*-split form of the two dimensional Euler equations in the differential form as

$$\frac{\partial \mathbf{U}}{\partial t} + \frac{\partial \mathbf{F}}{\partial x} + \frac{\partial \mathbf{G}}{\partial y} = 0 \tag{3.26}$$

where;

$$\mathbf{U} = \begin{bmatrix} u_1 \\ u_2 \\ u_3 \\ u_4 \end{bmatrix} = \begin{bmatrix} \rho \\ \rho u \\ \rho v \\ \rho e_t \end{bmatrix} \quad \mathbf{F} = \begin{bmatrix} f_1 \\ f_2 \\ f_3 \\ f_4 \end{bmatrix} = \begin{bmatrix} \rho u \\ \rho u^2 + p \\ \rho uv \\ \rho u h_t \end{bmatrix} \quad \mathbf{G} = \begin{bmatrix} g_1 \\ g_2 \\ g_3 \\ g_4 \end{bmatrix} = \begin{bmatrix} \rho v \\ \rho uv \\ \rho v^2 + p \\ \rho v h_t \end{bmatrix}$$

As can be observed the flux vector in Equation (3.26) is identical to the one appearing in the transformed form of the governing equations given by Equation (3.6). The theory of the Riemann problem for one dimensional linear systems will be employed to estimate this flux.

To obtain the Jacobian for the *x*-split Euler equations, the flux vector must be written in terms of the conserved variables as

$$\mathbf{F}=\begin{bmatrix} u_2 \\ \dfrac{u_2^2}{u_1}+(\gamma-1)\left(u_4-\dfrac{u_2^2}{2u_1}-\dfrac{u_3^2}{2u_1}\right) \\ \dfrac{u_2u_3}{u_1} \\ \dfrac{u_2u_4}{u_1}+(\gamma-1)\left(\dfrac{u_2u_4}{u_1}-\dfrac{u_2^3}{2u_1^2}-\dfrac{u_3^2u_2}{2u_1^2}\right) \end{bmatrix} \tag{3.27}$$

In Equation (3.27) γ is the specific heat ratio. Noting that the Jacobian matrix is specified in the following form

$$\frac{\partial \mathbf{F}}{\partial \mathbf{U}}=\mathbf{A}=\begin{bmatrix} \partial f_1/\partial u_1 & \partial f_1/\partial u_2 & \partial f_1/\partial u_3 & \partial f_1/\partial u_4 \\ \partial f_2/\partial u_1 & \partial f_2/\partial u_2 & \partial f_2/\partial u_3 & \partial f_2/\partial u_4 \\ \partial f_3/\partial u_1 & \partial f_3/\partial u_2 & \partial f_3/\partial u_3 & \partial f_3/\partial u_4 \\ \partial f_4/\partial u_1 & \partial f_4/\partial u_2 & \partial f_4/\partial u_3 & \partial f_4/\partial u_4 \end{bmatrix} \tag{3.28}$$

it can be obtained by equations (3.27) and (3.28) in terms of the flow variables.

$$\mathbf{A}=\begin{bmatrix} 0 & 1 & 0 & 0 \\ (\gamma-1)h_t-u^2-a^2 & (3-\gamma)u & (1-\gamma)v & \gamma-1 \\ -uv & v & u & 0 \\ u\left[(\gamma-2)h_t-a^2\right] & h_t-(\gamma-1)u^2 & -(\gamma-1)uv & \gamma u \end{bmatrix} \tag{3.29}$$

In Equation (3.29) *a* is the speed of sound. As can be observed from Equation (3.29), the Jacobian matrix does not have constant elements hence the Euler equations are

not linear. For the approximate Riemann solvers this Jacobian matrix is replaced by one that has constant elements since for a non-linear system the characteristic lines of the same family will not be parallel introducing shock waves and expansion fans into the solution (17), (16).

In Roe's approximate Riemann solver (19), the Jacobian matrix is expressed in terms of an intermediate state defined from the right and left states.

First, it is observed that both the flux vector **F** and the vector of conserved quantities **U** are quadratic in terms of a new vector **W** defined as

$$\mathbf{W} = \begin{bmatrix} w_1 \\ w_2 \\ w_3 \\ w_4 \end{bmatrix} = \sqrt{\rho} \begin{bmatrix} 1 \\ u \\ v \\ h_t \end{bmatrix} \tag{3.30}$$

Another useful vector, $\bar{\mathbf{W}}$, is formed by taking the arithmetic mean of the **W** vector for the right and left states.

$$\bar{\mathbf{W}} = \begin{bmatrix} \bar{w}_1 \\ \bar{w}_2 \\ \bar{w}_3 \\ \bar{w}_4 \end{bmatrix} = \begin{bmatrix} \dfrac{\sqrt{\rho_L} + \sqrt{\rho_R}}{2} \\ \dfrac{\sqrt{\rho_L} u_L + \sqrt{\rho_R} u_R}{2} \\ \dfrac{\sqrt{\rho_L} v_L + \sqrt{\rho_R} v_R}{2} \\ \dfrac{\sqrt{\rho_L} h_{tL} + \sqrt{\rho_R} h_{tR}}{2} \end{bmatrix} \tag{3.31}$$

It is now possible to express the difference between the right and the left states for the conserved quantities in terms of the new vector defined as

$$\Delta\mathbf{U} = \mathbf{B}\Delta\mathbf{W} \tag{3.32}$$

where;

$$\mathbf{B}=\begin{bmatrix} 2\overline{w}_1 & 0 & 0 & 0 \\ \overline{w}_2 & \overline{w}_1 & 0 & 0 \\ \overline{w}_3 & 0 & \overline{w}_1 & 0 \\ \dfrac{\overline{w}_4}{\gamma} & \dfrac{\gamma-1}{\gamma}\overline{w}_2 & \dfrac{\gamma-1}{\gamma}\overline{w}_3 & \dfrac{\overline{w}_1}{\gamma} \end{bmatrix}$$

It is also possible to express the differential flux vector in terms of the vector **W** in the same manner as

$$\Delta\mathbf{F}=\mathbf{C}\Delta\mathbf{W} \tag{3.33}$$

where;

$$\mathbf{C}=\begin{bmatrix} \overline{w}_2 & \overline{w}_1 & 0 & 0 \\ \dfrac{\gamma-1}{\gamma}\overline{w}_4 & \dfrac{\gamma+1}{\gamma}\overline{w}_2 & -\dfrac{\gamma-1}{\gamma}\overline{w}_3 & \dfrac{\gamma-1}{\gamma}\overline{w}_1 \\ 0 & \overline{w}_3 & \overline{w}_2 & 0 \\ 0 & \overline{w}_4 & 0 & \overline{w}_2 \end{bmatrix}$$

Using Equations (3.32) and (3.33) it is possible to establish a direct relation between the difference in the flux vector and the vector of conserved quantities in the form

$$\mathbf{C}\mathbf{B}^{-1}\Delta\mathbf{U}=\Delta\mathbf{F} \tag{3.34}$$

Using the homogeneity property of the Euler equations given by the following equation (16) one can recognize the product $\mathbf{C}\mathbf{B}^{-1}$ as the Jacobian matrix.

$$\mathbf{F}=\underbrace{\frac{\partial\mathbf{F}}{\partial\mathbf{U}}}_{\mathbf{A}}\mathbf{U} \tag{3.35}$$

In order to find the eigenvalues of the Jacobian matrix, the following equation must be solved.

$$\det\left(\mathbf{CB^{-1}}-\lambda\mathbf{I}\right)=0\Rightarrow\det\left(\mathbf{C}-\lambda\mathbf{B}\right)=0 \tag{3.36}$$

Dividing Equation (3.36) by $\overline{w}_1$, it is possible to find the eigenvalues of the Jacobian in terms of the new variables defined as

$$\tilde{u}=\frac{\overline{w}_2}{\overline{w}_1}=\frac{\sqrt{\rho_L}u_L+\sqrt{\rho_R}u_R}{\sqrt{\rho_L}+\sqrt{\rho_R}} \tag{3.37}$$

$$\tilde{v}=\frac{\overline{w}_3}{\overline{w}_1}=\frac{\sqrt{\rho_L}v_L+\sqrt{\rho_R}v_R}{\sqrt{\rho_L}+\sqrt{\rho_R}} \tag{3.38}$$

$$\tilde{h}_t=\frac{\overline{w}_4}{\overline{w}_1}=\frac{\sqrt{\rho_L}h_{tL}+\sqrt{\rho_R}h_{tR}}{\sqrt{\rho_L}+\sqrt{\rho_R}} \tag{3.39}$$

$$\tilde{a}=\sqrt{(\gamma-1)\left(\tilde{h}_t-\frac{1}{2}\tilde{V}^2\right)}=\sqrt{\gamma(\gamma-1)\left(\tilde{e}_t-\frac{1}{2}\tilde{V}^2\right)} \tag{3.40}$$

$$\tilde{\rho}=\sqrt{\rho_L\rho_R} \tag{3.41}$$

$$\tilde{\lambda}_1=\tilde{u}-\tilde{a}\quad\tilde{\lambda}_2=\tilde{\lambda}_3=\tilde{u}\quad\tilde{\lambda}_4=\tilde{u}+\tilde{a} \tag{3.42}$$

The corresponding right eigenvectors can also be expressed in terms of the new Roe averaged quantities as

$$\mathbf{r_1}=\begin{bmatrix}1\\ \tilde{u}-\tilde{a}\\ \tilde{v}\\ \tilde{h}_t-\tilde{u}\tilde{a}\end{bmatrix}\quad\mathbf{r}_2=\begin{bmatrix}1\\ \tilde{u}\\ \tilde{v}\\ \frac{1}{2}\tilde{V}^2\end{bmatrix}\quad\mathbf{r}_3=\begin{bmatrix}0\\ 0\\ 1\\ \tilde{v}\end{bmatrix}\quad\mathbf{r}_4=\begin{bmatrix}1\\ \tilde{u}+\tilde{a}\\ \tilde{v}\\ \tilde{h}_t+\tilde{u}\tilde{a}\end{bmatrix} \tag{3.43}$$

With the right eigenvectors defined as in Equation (3.43), it is possible to determine the characteristic variables which can also be termed as the wave strengths by using Equation (3.14).

$$\begin{bmatrix} 1 & 1 & 0 & 1 \\ \tilde{u}-\tilde{a} & \tilde{u} & 0 & \tilde{u}+\tilde{a} \\ \tilde{v} & \tilde{v} & 1 & \tilde{v} \\ \tilde{h}_t-\tilde{u}\tilde{a} & \frac{1}{2}\tilde{V}^2 & \tilde{v} & \tilde{h}_t+\tilde{u}\tilde{a} \end{bmatrix} \begin{bmatrix} \Delta v_1 \\ \Delta v_2 \\ \Delta v_3 \\ \Delta v_4 \end{bmatrix} = \begin{bmatrix} \Delta u_1 \\ \Delta u_2 \\ \Delta u_3 \\ \Delta u_4 \end{bmatrix} \tag{3.44}$$

Due to the proportionality between the coefficients of the first and third relations in Equation (3.44), it is possible to eliminate the third equation by using the first one to obtain the following relation.

$$\Delta v_3 = \Delta u_3 - \tilde{v}\Delta u_1 \tag{3.45}$$

Then a set of three equations is obtained for three wave strengths as

$$\begin{bmatrix} 1 & 1 & 1 \\ \tilde{u}+\tilde{a} & \tilde{u}-\tilde{a} & \tilde{u} \\ \tilde{h}_t+\tilde{u}\tilde{a} & \tilde{h}_t-\tilde{u}\tilde{a} & \frac{1}{2}\tilde{V}^2 \end{bmatrix} \begin{bmatrix} \Delta v_4 \\ \Delta v_1 \\ \Delta v_2 \end{bmatrix} = \begin{bmatrix} \Delta u_1 \\ \Delta u_2 \\ \Delta u_4 + \tilde{v}^2\Delta u_1 - \tilde{v}\Delta u_3 \end{bmatrix} \tag{3.46}$$

It is possible to solve this system using Gauss elimination to obtain the wave strengths as

$$\Delta v_2 = \frac{\gamma-1}{\tilde{a}^2}\left[\Delta u_1\left(\tilde{h}_t-\tilde{u}^2\right)+\tilde{u}\Delta u_2-\Delta u_4+\tilde{v}\left(\Delta u_3-\tilde{v}\Delta u_1\right)\right] \tag{3.47}$$

$$\Delta v_1 = \frac{1}{2\tilde{a}}\left[\left(\tilde{u}+\tilde{a}\right)\Delta u_1-\Delta u_2-\tilde{a}\Delta v_2\right] \tag{3.48}$$

$$\Delta v_4 = \Delta u_1 - (\Delta v_1+\Delta v_2) \tag{3.49}$$

Defining an operator given by the following equation

$$\Delta(pq) = \tilde{p}\Delta q + \tilde{q}\Delta p + O\left(\Delta^2\right) \tag{3.50}$$

neglecting higher order terms and placing the values of the conserved quantities, the wave strengths can be expressed in terms of the flow variables as

$$\begin{aligned} \Delta v_2 &= \frac{\gamma-1}{\tilde{a}^2}\left[\Delta\rho\left(\tilde{h}_t - \tilde{u}^2\right) + \tilde{u}^2\Delta\rho + \tilde{\rho}\tilde{u}\Delta u - \tilde{\rho}\Delta e_t - \tilde{e}_t\Delta\rho + \tilde{v}\left(\tilde{\rho}\Delta v + \tilde{v}\Delta\rho - \tilde{v}\Delta\rho\right)\right] \\ \Rightarrow \Delta v_2 &= \frac{\gamma-1}{\tilde{a}^2}\left[\Delta\rho\left(\tilde{h}_t - \tilde{e}_t\right) + \tilde{\rho}\tilde{u}\Delta u + \tilde{\rho}\tilde{v}\Delta v - \tilde{\rho}\Delta e_t\right] \end{aligned} \tag{3.51}$$

The terms appearing in Equation (3.51) must be treated individually to simplify the expression. For the treatment of the first term in the brackets, Equation (3.40) can be employed as

$$\Delta\rho\left(\tilde{h}_t - \tilde{e}_t\right) = \Delta\rho\left(\frac{\tilde{a}^2}{\gamma-1} + \frac{1}{2}\tilde{V}^2 - \frac{\tilde{a}^2}{\gamma(\gamma-1)} - \frac{1}{2}\tilde{V}^2\right) = \Delta\rho\frac{\tilde{a}^2}{\gamma} \tag{3.52}$$

The last term in the brackets must also be treated individually with the aid of the relation

$$e_t = \frac{1}{\gamma-1}\frac{p}{\rho} + \frac{V^2}{2} \tag{3.53}$$

To obtain

$$\tilde{\rho}\Delta e_t = \tilde{\rho}\left[\frac{1}{\gamma-1}\Delta\left(\frac{p}{\rho}\right) + \frac{1}{2}\Delta\left(u^2+v^2\right)\right] = \frac{\Delta p}{\gamma-1} - \frac{\tilde{a}^2\Delta\rho}{\gamma(\gamma-1)} + \tilde{\rho}\tilde{u}\Delta u + \tilde{\rho}\tilde{v}\Delta v \tag{3.54}$$

Substituting Equations (3.52) and (3.54) into Equation (3.51), a simplified equation for the wave strength can be obtained. Then applying the operator defined in

Equation (3.50) and substituting Equation (3.57) into Equations (3.48) and (3.49) all the wave strengths can be found as

$$\Delta v_1 = \frac{1}{2\tilde{a}^2}\left(\Delta p - \tilde{\rho}\tilde{a}\Delta u\right) \tag{3.55}$$

$$\Delta v_2 = \Delta\rho - \frac{\Delta p}{\tilde{a}^2} \tag{3.56}$$

$$\Delta v_3 = \tilde{\rho}\Delta v \tag{3.57}$$

$$\Delta v_4 = \frac{1}{2\tilde{a}^2}\left(\Delta p + \tilde{\rho}\tilde{a}\Delta u\right) \tag{3.58}$$

In summary, for the approximate Riemann solver of Roe, first the Jacobian matrix for the Euler equations, which are non linear in their true essence, have been replaced by another matrix with constant elements to approximate the governing equations as a linear system. Thereafter the eigenvalues and eigenvectors of this approximate Jacobian matrix are found by following the procedure outlined in (19). Then these are used to find the wave strengths, characteristic variables, and fluxes through a face for which the right and left states are known according to Equation (3.25).

3.3.1 Solution Algorithm

The solution algorithm adopted is similar to the one outlined in (16). The algorithm discussed here is for the determination of the flux through a certain face of the cell under investigation. Once the fluxes through all the faces are determined, an appropriate method for time integration, to be discussed later, is employed to update the values of the conserved variables.

(i) First the conserved variables of the left and right states are obtained by reconstruction which will be explained later on.

(ii) The primitive variables, $\begin{bmatrix} \rho & u & v & P & h_t \end{bmatrix}^T$ for the right and left states are determined from the conserved variables $\begin{bmatrix} \rho & \rho u & \rho v & \rho e_t \end{bmatrix}^T$ simultaneously with the transformation to normal and tangential coordinates. The flux which will be used in Equation (3.25), is calculated from the left and right state variables.

$$\hat{u} = \frac{\rho u \cos\theta + \rho v \sin\theta}{\rho} \tag{3.59}$$

$$\hat{v} = \frac{-\rho u \sin\theta + \rho v \cos\theta}{\rho} \tag{3.60}$$

$$p = (\gamma - 1)\left[\rho e_t - \frac{(\rho u)^2}{\rho} - \frac{(\rho v)^2}{\rho} \right] \tag{3.61}$$

$$h_t = \frac{1}{\rho}(\rho e_t + p) \tag{3.62}$$

(iii) The Roe averaged quantities for the transformed primitive variables and the eigenvalues are calculated from Equations (3.37) through (3.42).

(iv) The wave strengths are calculated from Equations (3.55) through (3.58). The differences are taken as the right minus the left state variables in contrast to Roe's derivation in (19) to be consistent with Equation (3.25).

(v) The right eigenvectors are calculated using the transformed Roe averaged quantities with the formulation provided in Equation (3.43).

(vi) The flux is calculated from Equation (3.25).

(vii) The flux obtained, which is normal to the face, is transformed back to the Cartesian coordinates using the inverse transformation matrix.

$$\mathbf{T}^{-1}\hat{\mathbf{F}} = \mathbf{F} \tag{3.63}$$

where $\mathbf{T}^{-1}$ is given in Equation (3.5).

3.4 Flux Vector Splitting

In addition to using Roe's approximate Riemann solver to evaluate the flux term appearing in Equation (3.8), the flux vector splitting methods such as van Leer (20), AUSM (21) and its derivatives AUSMD, AUSMV (22) have also been employed.

Considering Equation (3.9) it is possible to split the flux vector as

$$\mathbf{F}(\mathbf{U}) = \mathbf{F}^{+}(\mathbf{U}) + \mathbf{F}^{-}(\mathbf{U}) \tag{3.64}$$

The negative and positive components of the flux vector, $\mathbf{F}^{+}$ and $\mathbf{F}^{-}$, can be defined by splitting the Jacobian matrix as follows

$$\mathbf{F}^{+}(\mathbf{U}) = \mathbf{A}^{+}\mathbf{U} \quad , \quad \mathbf{F}^{-}(\mathbf{U}) = \mathbf{A}^{-}\mathbf{U} \tag{3.65}$$

$$\mathbf{A}^{+} = \mathbf{Q}\boldsymbol{\Lambda}^{+}\mathbf{Q}^{-1} \quad , \quad \mathbf{A}^{-} = \mathbf{Q}\boldsymbol{\Lambda}^{-}\mathbf{Q}^{-1} \tag{3.66}$$

The diagonal matrices $\boldsymbol{\Lambda}^{+}$ and $\boldsymbol{\Lambda}^{-}$ can be defined as

$$\boldsymbol{\Lambda}^{+} = \begin{bmatrix} \lambda_1^{+} & 0 & . & . & 0 \\ 0 & . & & & . \\ . & & . & & . \\ . & & & . & 0 \\ 0 & . & . & 0 & \lambda_m^{+} \end{bmatrix} \quad , \quad \boldsymbol{\Lambda}^{-} = \begin{bmatrix} \lambda_1^{-} & 0 & . & . & 0 \\ 0 & . & & & . \\ . & & . & & . \\ . & & & . & 0 \\ 0 & . & . & 0 & \lambda_m^{-} \end{bmatrix} \tag{3.67}$$

where the positive and negative eigenvalues can be defined as in (23) presented as in the following equation.

$$\lambda^{+} = \frac{1}{2}\left(\lambda + |\lambda|\right) \quad , \quad \lambda^{-} = \frac{1}{2}\left(\lambda - |\lambda|\right) \tag{3.68}$$

When the Euler equations are written in normal and tangential coordinates as in Equation (3.8) the positive flux component will be due to the cell itself while the

negative component will be calculated from the neighbour as illustrated in Figure 3.2.

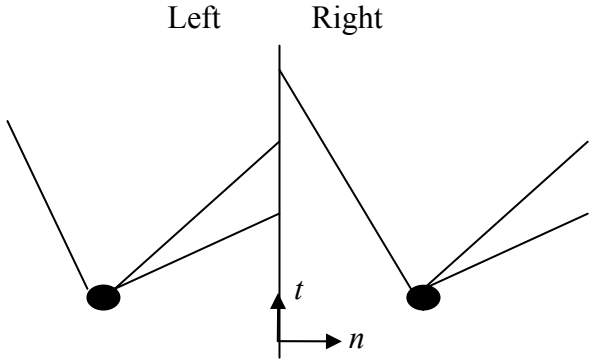

Figure 3.2- Graphical interpretation of flux vector splitting

In Figure 3.2 the left state is the cell under investigation while the right state is the neighbour. The positive eigenvalues of the left state affects the face hence the positive component of the flux is calculated from the left state while the negative component of the flux is calculated from the right state since the negative eigenvalues of this state affects the face. Further details can be found in (16).

3.4.1 Van Leer Flux Vector Splitting

The van Leer flux vector splitting algorithm (20) makes use of the flux represented in terms of the density, tangential velocity, Mach number, $\hat{M}$, and the speed of sound as

$$\hat{\mathbf{F}}(\hat{\mathbf{U}}) = \begin{bmatrix} \rho a \hat{M} \\ \rho a^2 \left(\hat{M}^2 + \dfrac{1}{\gamma} \right) \\ \rho a \hat{M} \hat{v} \\ \rho a \hat{M} \left[\dfrac{1}{2} \left(a^2 \hat{M}^2 + \hat{v}^2 \right) + \dfrac{a^2}{\gamma - 1} \right] \end{bmatrix} \quad , \quad \hat{M} = \frac{\hat{u}}{a} \tag{3.69}$$

The flux can then be split into its positive and negative components as presented in the following equations.

$$\hat{\mathbf{F}}^{+} = \frac{1}{4}\rho a\left(1+\hat{M}\right)^2 \begin{bmatrix} 1 \\ \frac{2a}{\gamma}\left(\frac{\gamma-1}{2}\hat{M}+1\right) \\ \hat{v} \\ \frac{2a^2}{\gamma^2-1}\left(\frac{\gamma-1}{2}\hat{M}+1\right)^2+\frac{1}{2}\hat{v}^2 \end{bmatrix} \tag{3.70}$$

$$\hat{\mathbf{F}}^{-} = -\frac{1}{4}\rho a\left(1-\hat{M}\right)^2 \begin{bmatrix} 1 \\ \frac{2a}{\gamma}\left(\frac{\gamma-1}{2}\hat{M}-1\right) \\ \hat{v} \\ \frac{2a^2}{\gamma^2-1}\left(\frac{\gamma-1}{2}\hat{M}-1\right)^2+\frac{1}{2}\hat{v}^2 \end{bmatrix} \tag{3.71}$$

3.4.2 AUSM (Liou-Steffen) Flux Vector Splitting

The AUSM scheme (21) splits the pressure and the advection terms appearing in the normal momentum flux as

$$\hat{\mathbf{F}}(\hat{\mathbf{U}}) = \frac{1}{2}\left[\hat{M}_{1/2}\left(\boldsymbol{\varphi}_L+\boldsymbol{\varphi}_R\right)-\left|\hat{M}_{1/2}\right|\left(\boldsymbol{\varphi}_R-\boldsymbol{\varphi}_L\right)\right]+\mathbf{p}_{1/2} \tag{3.72}$$

In equation (3.72), $\hat{M}_{1/2}$ is the interface Mach number, $\mathbf{p}_{1/2}$ is the vector of interface pressure and $\boldsymbol{\varphi}$ is the vector of flux defined through the following equations.

$$\hat{M}_{1/2} = \hat{M}_L^{+} + \hat{M}_R^{-} \tag{3.73}$$

$$\mathbf{p}_{1/2} = \begin{bmatrix} 0 \\ p_{1/2} \\ 0 \\ 0 \end{bmatrix} \quad , \quad p_{1/2} = p_L^+ + p_R^- \tag{3.74}$$

$$\boldsymbol{\varphi} = \begin{bmatrix} \rho a \\ \rho \hat{u} a \\ \rho \hat{v} a \\ \rho h_t a \end{bmatrix} \tag{3.75}$$

The split Mach numbers and the split pressures can be defined as in the following equations to complete the algorithm.

$$\hat{M}^{\pm} = \begin{cases} \pm\frac{1}{4}\left(\hat{M} \pm 1\right)^2 & \left|\hat{M}\right| \le 1 \\ \frac{1}{2}\left(\hat{M} \pm \left|\hat{M}\right|\right) & \left|\hat{M}\right| > 1 \end{cases} \tag{3.76}$$

$$p^{\pm} = p\hat{M}^{\pm} \cdot \begin{cases} \pm 2 - \hat{M} & \left|\hat{M}\right| \le 1 \\ \frac{1}{\hat{M}} & \left|\hat{M}\right| > 1 \end{cases} \tag{3.77}$$

3.4.3 AUSMD Flux Vector Splitting

AUSMD flux vector splitting (22) is a derivative of the original AUSM scheme. As in the AUSM scheme the advection and pressure terms are split separately with the difference that instead of estimating the normal velocity at the interface the mass flux is estimated. Also the velocity splitting is modified in the AUSMD method as in the equations to follow.

$$\hat{\mathbf{F}}(\hat{\mathbf{U}}) = \frac{1}{2}\left[\left(\rho\hat{u}\right)_{1/2}\left(\boldsymbol{\Gamma}_L + \boldsymbol{\Gamma}_R\right) - \left|\left(\rho\hat{u}\right)_{1/2}\right|\left(\boldsymbol{\Gamma}_R - \boldsymbol{\Gamma}_L\right)\right] + \mathbf{p}_{1/2} \tag{3.78}$$

$$\left(\rho\hat{u}\right)_{1/2} = \hat{u}_L^+ \rho_L + \hat{u}_R^- \rho_R \tag{3.79}$$

$$\hat{u}_L^+ = \begin{cases} \kappa_L \left[\dfrac{\left(\hat{u}_L + a_{\max}\right)^2}{4a_{\max}} \right] + \left(1-\kappa_L\right) \dfrac{\hat{u}_L + \left|\hat{u}_L\right|}{2} & \left|\hat{u}_L\right| \le a_{\max} \\ \dfrac{\hat{u}_L + \left|\hat{u}_L\right|}{2} & \left|\hat{u}_L\right| > a_{\max} \end{cases} \tag{3.80}$$

$$\hat{u}_R^- = \begin{cases} \kappa_R \left[-\dfrac{\left(\hat{u}_R - a_{\max}\right)^2}{4a_{\max}} \right] + \left(1-\kappa_R\right) \dfrac{\hat{u}_R - \left|\hat{u}_R\right|}{2} & \left|\hat{u}_R\right| \le a_{\max} \\ \dfrac{\hat{u}_R - \left|\hat{u}_R\right|}{2} & \left|\hat{u}_R\right| > a_{\max} \end{cases} \tag{3.81}$$

$$\kappa_L = \frac{2(p/\rho)_L}{(p/\rho)_L + (p/\rho)_R} \ , \ \kappa_R = \frac{2(p/\rho)_R}{(p/\rho)_L + (p/\rho)_R} \ , \ a_{\max} = \max(a_L, a_R) \tag{3.82}$$

Naturally the vector of flux is modified as well as the split pressure as

$$\mathbf{\Gamma} = \begin{bmatrix} 1 \\ \hat{u} \\ \hat{v} \\ h_t \end{bmatrix} \tag{3.83}$$

$$p_{1/2} = p_L^+ + p_R^- \tag{3.84}$$

$$p_L^+ = \begin{cases} p_L \dfrac{\left(\hat{u}_L + a_{\max}\right)^2}{4a_{\max}^2} \left(2 - \dfrac{\hat{u}_L}{a_{\max}} \right) & \left|\hat{u}_L\right| \le a_{\max} \\ p_L \dfrac{\hat{u}_L + \left|\hat{u}_L\right|}{2\hat{u}_L} & \left|\hat{u}_L\right| > a_{\max} \end{cases} \tag{3.85}$$

$$p_R^- = \begin{cases} p_R \dfrac{\left(\hat{u}_R - a_{\max}\right)^2}{4a_{\max}^2} \left(2 + \dfrac{\hat{u}_R}{a_{\max}} \right) & \left|\hat{u}_R\right| \le a_{\max} \\ p_R \dfrac{\hat{u}_R - \left|\hat{u}_R\right|}{2\hat{u}_R} & \left|\hat{u}_R\right| > a_{\max} \end{cases} \tag{3.86}$$

3.4.4 AUSMV Flux Vector Splitting

Another derivative of the AUSM scheme is the AUSMV flux vector splitting scheme (22). Similar to the AUSMD scheme the mass flux at the interface of two cells are estimated as in Equations (3.78) and (3.79) in the AUSMV scheme except for the normal momentum. The normal momentum is estimated at the interface wholly as

$$\left(\rho\hat{u}^2\right)_{1/2} = \hat{u}_L^+\left(\rho\hat{u}\right)_L + \hat{u}_R^-\left(\rho\hat{u}\right)_R \tag{3.87}$$

The definitions of the split velocities and the pressures differs from the AUSMD scheme as can be observed from the following equations

$$\hat{u}^{\pm} = \begin{cases} \pm\dfrac{\left(\hat{u}\pm a\right)^2}{4a} & \left|\hat{u}\right| \le a \\ \dfrac{\hat{u}\pm\left|\hat{u}\right|}{2} & \left|\hat{u}\right| > a \end{cases} \tag{3.88}$$

$$p^{\pm} = p\hat{u}^{\pm}\cdot\begin{cases} \dfrac{1}{a}\left(\pm 2 - \dfrac{\hat{u}}{a}\right) & \left|\hat{u}\right| \le a \\ \dfrac{1}{\hat{u}} & \left|\hat{u}\right| > a \end{cases} \tag{3.89}$$

3.5 Boundary Conditions

The boundary conditions encountered for the external flows considered in the scope of the thesis work are the solid wall and the far-field boundary conditions. For the numerical method adopted, the implementation of either type of the boundary conditions is equivalent to determining the correct right state variables since the left state variables will always be dictated by the cell under investigation.

For the solid wall, the physical boundary condition is that there is no flux into the body. In the inviscid case considered, this means that the velocity at the face can be in the tangential direction.

At this point, one of two methods can be adopted for the determination of the right state variables (14). One is to directly take the flux through the face as zero and to calculate a right flux solely based on pressure that is equal to the pressure calculated for the left state. The reason for this equality is that under steady-state conditions, the pressure force exerted by the fluid will be countered with an equal force. The second method is to construct a ghost right state for which the tangential velocity, pressure and total enthalpy are equal to the left state. The direction of the tangential velocity is the same as the left state as well as the magnitude. For the normal velocity, the magnitude is equal to that of the left state but the direction is opposite to it. The ghost right state is depicted for an example cut-cell in Figure 3.3.

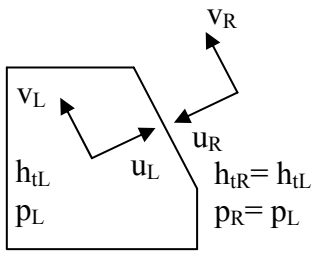

Figure 3.3- Ghost right state at the solid wall

The second method ensures zero flux through the face as well but it also takes into cases where there is a normal velocity component in the presence of high curvatures as stated in (14). In the code developed, the second method has been adopted for the solid wall treatment.

For the far-field boundary conditions the right state is calculated from the conditions received as input and it is irrespective of the left state.

3.6 Reconstruction of the Flow Variables

For the calculation of the fluxes through a face, primitive flow variables have to be estimated on both sides of that face, the right and left states. The simplest approach

would be to take the values from the cell under investigation as the left state and to take the values from the respective neighbour as the right state. This approach being first order does not produce very accurate results. Hence it is desirable to reconstruct the flow variables within the cell to obtain a solution of second order. That is the variation of the flow variables within the cell must be taken into account even though in finite volume methods the flow variables representative of the whole cell is stored at the cell centroid for higher order accuracy.

Three reconstruction schemes have been sighted in the literature. In two of these three schemes, the gradient of the flow variable is estimated at the centre of the cell while the other one makes use of finite differences to estimate the value of a flow variable at certain points within the cell. One of the reconstruction schemes based on the gradient at the centre of the cell is the Green-Gauss reconstruction, the other one is the Least Squares (Minimum Energy) reconstruction. The general design criteria for these reconstruction schemes are discussed in (24) and (25). The details of the linear reconstruction based on these schemes can be found in (26), (27) and (14) while the k^{th} order exact schemes are discussed in (28). The third scheme based on the finite difference method can be found in (29).

3.6.1 Gauss-Green Reconstruction

The Gauss-Green reconstruction is based mainly on the gradient theorem. For a quantity *u* related to the cell this can be formulized as

$$\nabla u = \frac{1}{A_\Omega} \int_\Omega u \vec{n} d\ell \tag{3.90}$$

This integral is evaluated for a region Ω which is bounded by the lines that connect the centroids of the edge and vertex neighbours (support set) of the cell. The integral can be evaluated numerically using the trapezoidal rule given as

$$\nabla u = \frac{1}{A_{cell}} \sum_{i=0}^{N_{sup}} \frac{1}{2} (u_i + u_{i+1}) \vec{n}_i \ell_i \tag{3.91}$$

The boundary of the region Ω is shown for two representative cases for a Cartesian mesh in Figure 3.4.

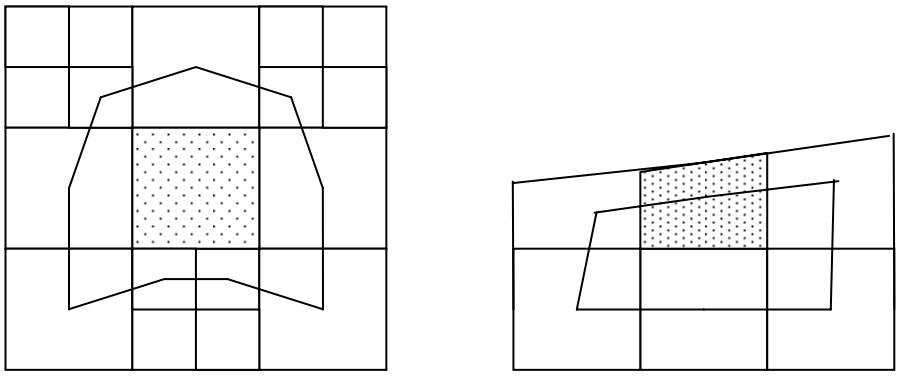

Figure 3.4- Region formed by the support set

3.6.2 Least Squares (Minimum Energy) Reconstruction

The Least Squares reconstruction is basically the inverse of the averaging function for a quantity related to a cell. The average of a quantity u within a cell can be defined with the averaging function presented as

$$Av(u) = \frac{\int_{A_{cell}} udA}{A_{cell}} = \overline{u} \tag{3.92}$$

A k^{th} order polynomial u^k is constructed to represent the quantity u within the cell such that the average of the polynomial will be equal to that of the cell and the polynomial will represent quantity u exactly if u is a polynomial of order k or less. In general, the constructed polynomial can be obtained as

$$u^k = \overline{u} + \sum_{m+n \le k} \alpha_{mn} \left[x^m y^n - Av(x^m y^n) \right] \tag{3.93}$$

where α_{mn} are arbitrary coefficients.

The form given in Equation (3.93) will ensure that the average of the polynomial is equal to that of the cell. For a linear case, this reconstruction takes the form presented in the following equation

$$u^1(x,y) = \bar{u} + \alpha_{10}\left[x - x_c\right] + \alpha_{01}\left[y - y_c\right] \tag{3.94}$$

In Equation (3.94), the centroidal coordinates of the cell appear since by definition the averaging function applied to the polynomials x and y within the cell gives the centroid coordinates of the cell.

The reconstruction problem simplifies once the cell average values are thought to be the values of the flow variables stored at the centroid of the cell (24). Then one could get the expression of the following form for the linear reconstruction.

$$u^1(x,y) = u_c + u_{xc}\left[x - x_c\right] + u_{yc}\left[y - y_c\right] \tag{3.95}$$

In Equation (3.95), the only unknowns are u_{xc} and u_{yc}, which are the components of the gradient of quantity u at the centroid of the cell.

Once the linear polynomial is obtained for the quantity u, the sum of the squares of the averages of the difference between the value of u obtained from constructed polynomial and its actual value is minimized within the region made up of the cells that form the support set to find the unknowns u_{xc} and u_{yc}. The support set is defined in the same way as the Green-Gauss reconstruction shown in Figure 3.4. This constitutes the least squares problem for the reconstruction.

$$S = \sum_{i=1}^{N_{\text{sup}}} \left[Av(u^1 - u_i) \right]^2 \tag{3.96}$$

$$\frac{\partial S}{\partial u_{xc}} = 0 \quad , \quad \frac{\partial S}{\partial u_{yc}} = 0 \tag{3.97}$$

Once the differentiations given in Equation (3.97) are performed, the expressions given in the following equations are obtained.

$$\frac{\partial S}{\partial u_{xc}} = \sum_{i=1}^{N_{\text{sup}}} 2\left\{ Av(u^1 - u_i) \cdot \frac{\partial\left[Av(u^1 - u_i) \right]}{\partial u_{xc}} \right\} = 0 \tag{3.98}$$

$$\frac{\partial S}{\partial u_{yc}} = \sum_{i=1}^{N_{\text{sup}}} 2\left\{ Av(u^1 - u_i) \cdot \frac{\partial\left[Av(u^1 - u_i) \right]}{\partial u_{yc}} \right\} = 0 \tag{3.99}$$

Then the average term over the region constructed by the cells in the support set is evaluated.

$$Av(u^1 - u_i) = \frac{1}{A_i}\left[\int_i u_c dA_i - \int_i u_i dA_i + u_{xc}\int_i (x - x_c) dA_i + u_{yc}\int_i (y - y_c) dA_i \right] \tag{3.100}$$

Once the integrals in Equation (3.100) are evaluated and the expressions simplified, it is possible to arrive at the following equation

$$Av(u^1 - u_i) = (u_c - u_{ci}) + u_{xc}(x_{ci} - x_c) + u_{yc}(y_{ci} - y_c) \tag{3.101}$$

When the expression presented in Equation (3.101) for each cell in the support set is placed in the summations given in Equations (3.98) and (3.99), two equations for the two unknowns can be obtained as

$$\frac{\partial S}{\partial u_{xc}} = \sum_{i=1}^{N_{\text{sup}}} \left[(u_c - u_{ci}) + u_{xc}(x_{ci} - x_c) + u_{yc}(y_{ci} - y_c) \right](x_{ci} - x_c) = 0 \tag{3.102}$$

$$\frac{\partial S}{\partial u_{yc}} = \sum_{i=1}^{N_{\text{sup}}} \left[(u_c - u_{ci}) + u_{xc}(x_{ci} - x_c) + u_{yc}(y_{ci} - y_c) \right](y_{ci} - y_c) = 0 \tag{3.103}$$

Equations (3.102) and (3.103) can be presented in a matrix form as

$$\begin{bmatrix} \sum_{i=1}^{N_{sup}} (x_{ci}-x_c)^2 & \sum_{i=1}^{N_{sup}} (x_{ci}-x_c)(y_{ci}-y_c) \\ \sum_{i=1}^{N_{sup}} (x_{ci}-x_c)(y_{ci}-y_c) & \sum_{i=1}^{N_{sup}} (y_{ci}-y_c)^2 \end{bmatrix} \begin{bmatrix} u_{xc} \\ u_{yc} \end{bmatrix} = \begin{bmatrix} \sum_{i=1}^{N_{sup}} (u_{ci}-u_c)(x_{ci}-x_c) \\ \sum_{i=1}^{N_{sup}} (u_{ci}-u_c)(y_{ci}-y_c) \end{bmatrix} \quad (3.104)$$

This matrix can be solved to obtain the gradients at the centre of the cell from which the value of quantity u can be obtained at any location within the cell. The least squares method is employed for the reconstruction in the code developed.

3.6.3 Gradient Limiting

It is undesirable to introduce new maxima points within the region formed by the support cells and the cell for which the gradient of flow variables are being constructed. Hence, the gradients are multiplied by a limiter to avoid introduction of new maxima points. The linear reconstruction takes the following form with the application of this condition.

$$u^1 = u_c + \Phi\left[u_{xc}(x-x_c) + u_{yc}(y-y_c)\right] \quad (3.105)$$

The value of the limiter Φ is between 0 and 1. To determine the exact value of the limiter, the maximum and the minimum of the values of quantity u are found at the cell centroids.

$$\begin{aligned} u^{\max} &= \max(u_c, u_{ic}) \\ u^{\min} &= \min(u_c, u_{ic}) \qquad i = 1,\ldots, N_{sup} \end{aligned} \quad (3.106)$$

Then the values of the reconstructed polynomial are evaluated at the corners of the cell since these locations will have the maximum and minimum values within the cell for a linear reconstruction. The value of quantity u which deviates the most from the centroidal value will be marked as u^1_{cor} serving as a basis for determining the value

of the limiter with the implementation of the formulation given in the following equation

$$\Phi = \begin{cases} \min\left(1, \dfrac{u^{\max} - u_c}{u^1_{cor} - u_c}\right) & u^1_{cor} - u_c > 0 \\ \min\left(1, \dfrac{u_c - u^{\min}}{u_c - u^1_{cor}}\right) & u^1_{cor} - u_c < 0 \\ 1 & u^1_{cor} - u_c = 0 \end{cases} \tag{3.107}$$

3.7 Temporal Discretization

Once the flux terms in the governing Equation (3.8) is obtained, then the temporal discretization has to be performed to update the values of the conserved quantities. A multi-stage time stepping method is employed for temporal discretization. A detailed discussion of the multi-stage methods can be found in (30).

3.7.1 Explicit Time Stepping Schemes

To apply the multi-stage time stepping method, an alternative representation of the governing Equation (3.8) is employed as

$$\frac{\partial \mathbf{U}}{\partial t} + \frac{1}{A_{cell}} \mathbf{R} = 0 \tag{3.108}$$

In Equation (3.108), the flux terms are presented in a more compact form as residual vector, $\mathbf{R}$, and its value can be determined from the known values of the conserved quantities at a given stage. Hence, Equation (3.108) can be treated as an ordinary differential equation. This equation can be discretized in *m*-stages as described in (31) to obtain the following equation.

$$\begin{aligned} \mathbf{U_0} &= \mathbf{U^n} \\ \mathbf{U_1} &= \mathbf{U_0} - \beta_1 \frac{\Delta t}{A_{cell}} \mathbf{R^0} \\ &\vdots \\ \mathbf{U^{n+1}} = \mathbf{U^m} &= \mathbf{U_0} - \beta_m \frac{\Delta t}{A_{cell}} \mathbf{R^{m-1}} \end{aligned} \tag{3.109}$$

In Equation (3.109), β's are stage coefficients while Δt is the time step. The residuals are evaluated from the values of the conserved variables from the previous stage. Hence, this is an explicit formulation. In contrast to classical Runge-Kutta methods only the values of the zeroth solution and the last residual have to be stored in this formulation (31). It is possible to tune the value of β for stability and to obtain larger time steps.

Table 3.1- Stage coefficients and CFL numbers for the multi-stage method

	first-order scheme			second-order scheme		
stages	3	4	5	3	4	5
σ	1.5	2.0	2.5	0.69	0.92	1.15
β_1	0.1481	0.0833	0.0533	0.1918	0.1084	0.0695
β_2	0.4000	0.2069	0.1263	0.4929	0.2602	0.1602
β_3	1.0000	0.4265	0.2375	1.0000	0.5052	0.2898
β_4		1.0000	0.4414		1.0000	0.5060
β_5			1.0000			1.0000

Table 3.1 taken from (31) shows the optimised values of the stage coefficients and CFL numbers for three, four and five stage methods of first and second order accuracy. The CFL number is a factor that governs how large the time step can be with respect to the cell area. In the code developed, three and four stage second order schemes are used.

3.7.2 Determination of the Time Step

In Equation (3.109), the value of the time step is not determined. The value of the time step, if taken to be too large, will introduce stability problems. If this value is taken to be too small then the convergence will be very slow and unnecessary amount of computations will be performed.

The mesh generated for an arbitrary geometry will contain cells that have different sizes and since the time step is dependent on the cell size, every cell will have a different maximum time step. As a result, a different time step will be used for each cell since a steady state solution is sought.

The time step is calculated in terms of the area of the cell under investigation as in the following formulation given in (31).

$$\frac{\Delta t}{A_{cell}} = \frac{\sigma}{\Psi^x + \Psi^y} \tag{3.110}$$

where σ is the CFL number and Ψ is the spectral radius.

The spectral radii Ψ that appear in Equation (3.110) can be calculated using the length of the edge projections of the cell in both *x*-*y* directions, S^x and S^y.

$$\Psi^x = \frac{1}{2}\left(|u| + a\right)\sum_{edges} S^x \tag{3.111}$$

$$\Psi^y = \frac{1}{2}\left(|v| + a\right)\sum_{edges} S^y \tag{3.112}$$

The time step obtained thus is multiplied by a safety factor in some cases to promote stable solutions. If Equation (3.110) is investigated, this equation is in one sense a division of a characteristic length by a characteristic speed. The characteristic speed is the maximum speed with which information is carried for a cell. Hence, the time

step is obtained by constricting the distance information travels from a cell within the field.

3.8 Solution Refinement

Once a certain level of convergence is achieved, the cells are refined according to the gradient of the solution. The purpose of this refinement is to provide enough resolution at the places where there might be discontinuities due to shocks or there are large gradients in the solution (e.g. around the stagnation point).

The solution refinement criterion used is based on the one outlined in (14). This method is based on both the curl of the velocity, for detecting shear layers, and the gradient of the velocity, for detecting shocks. The curl and gradient of the velocity is multiplied by some characteristic length of the cell as

$$\tau = \sqrt{A_{cell}}^{\frac{3}{2}} \left(\nabla \cdot \vec{V} \right) \ , \ \zeta = \sqrt{A_{cell}}^{\frac{3}{2}} \left(\nabla \times \vec{V} \right) \tag{3.113}$$

The standard deviations of the quantities defined in Equation (3.113) are calculated and the cells exceeding the standard deviation are refined.

$$\begin{cases} \tau_j > \sigma_\tau = \sqrt{\dfrac{\left(\sum_{i=1}^{n_{cell}} \tau_i \right)^2}{n_{cell}}} & \text{Refine cell j} \\ \zeta_j > \sigma_\zeta = \sqrt{\dfrac{\left(\sum_{i=1}^{n_{cell}} \zeta_i \right)^2}{n_{cell}}} & \text{Refine cell j} \end{cases} \tag{3.114}$$

CHAPTER 4

RESULTS &DISCUSSIONS

To test the validity of the code developed, the flow around a NACA0012 airfoil and an NLR7301 with a flap has been solved for different conditions. Besides demonstrating the characteristic features of the flows, different methods for handling the flux terms in the governing equations have been compared.

4.1 NACA0012

The NACA0012 tests have been performed for a subsonic case and a transonic case. In the subsonic tests the aim is to show the importance of reconstruction to obtain second order solutions and to discuss the role of first order solution on the stability.

The transonic tests have been performed to demonstrate the shock capturing capabilities of the various methods used to evaluate the flux terms. Also they are compared in terms of computational efficiency.

4.1.1 Subsonic Tests

The far-field boundary condition of the first case for the subsonic tests is a free stream Mach number of 0.6 and an angle of attack of 0˚. The experimental data for this case can be found in (32) which were extracted from (33). For this case a total of six runs have been performed. All the runs are performed using Roe's method. The convergence criterion for all of the runs is that the standard deviation of the residual calculated for the continuity equation should drop five levels on a log scale. Two of the six runs are first order solutions. One of these solutions is with solution refinement while the other is not. Two runs are performed second order with and

without solution refinement, while the last two are run first order until the residuals drop four levels then they switch to second order.

The pressure coefficient vs. the chord graph for the first order solutions are presented in Figure 4.1.

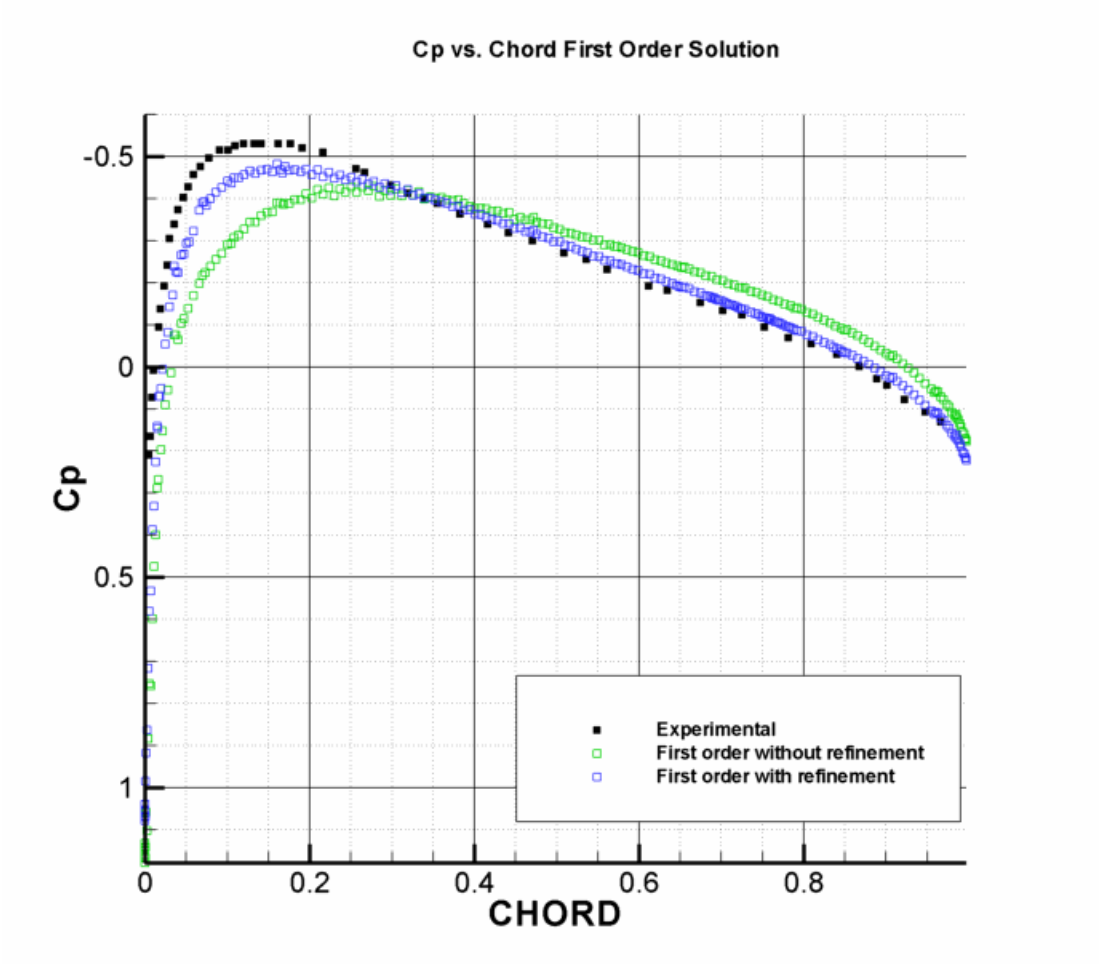

Figure 4.1- Cp vs. chord for first order solution

As can be seen from Figure 4.1, the first order solution without solution refinement performs poorly. It is not possible to catch the peak of the pressure coefficient with this solution. However, solution refinement introduces a considerable improvement

to the solution. But even with solution refinement the peak of the pressure coefficient graph is not captured accurately.

The pressure coefficient vs. chord graph can also be illustrated for the second order solution as in Figure 4.2.

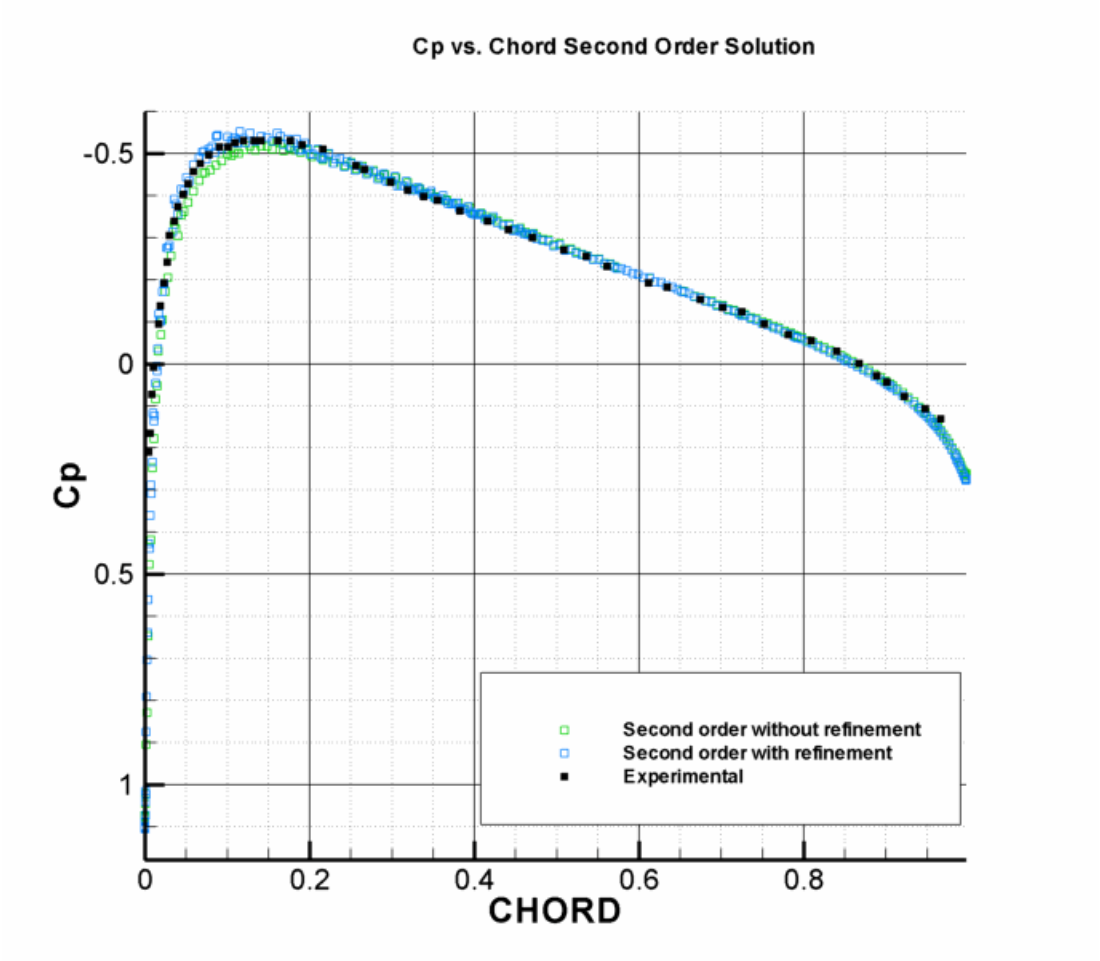

Figure 4.2- Cp vs. chord for second order solution

As can be seen from Figure 4.2, the second order solution provides a much more accurate solution than the first order method as expected. The peak of the pressure coefficient is captured accurately for both of the solutions with and without solution

refinement although the solution with solution refinement is slightly better on this aspect.

The effect of solution refinement can be illustrated by examining the differences between a refined and non-refined mesh.

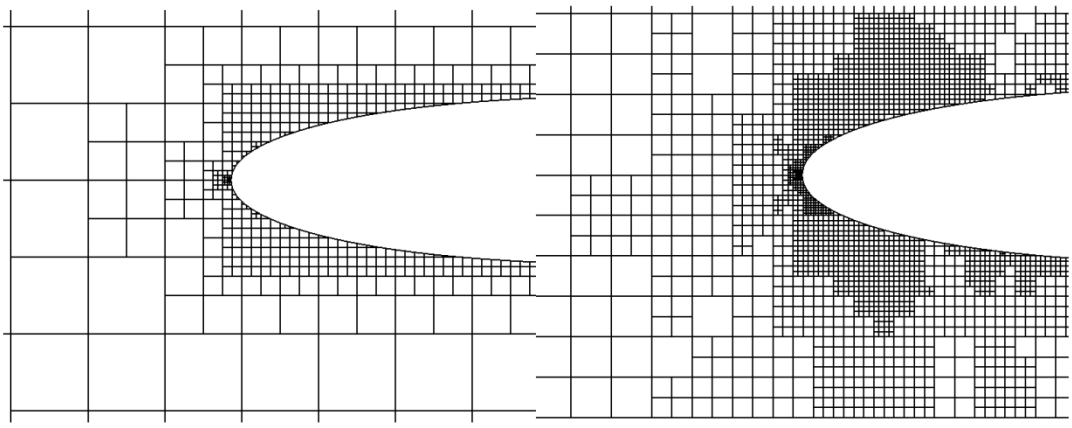

Figure 4.3- A refined and non-refined mesh around stagnation point

In Figure 4.3, the mesh on the right belonging to a solution with refinement has a considerably denser mesh around the stagnation point than the one without refinement. This is an expected result since there are large gradients around this region.

Finally the results obtained with the solution where first order is used until some convergence is obtained and then it is switched to second order, can be compared with the fully second order solution.

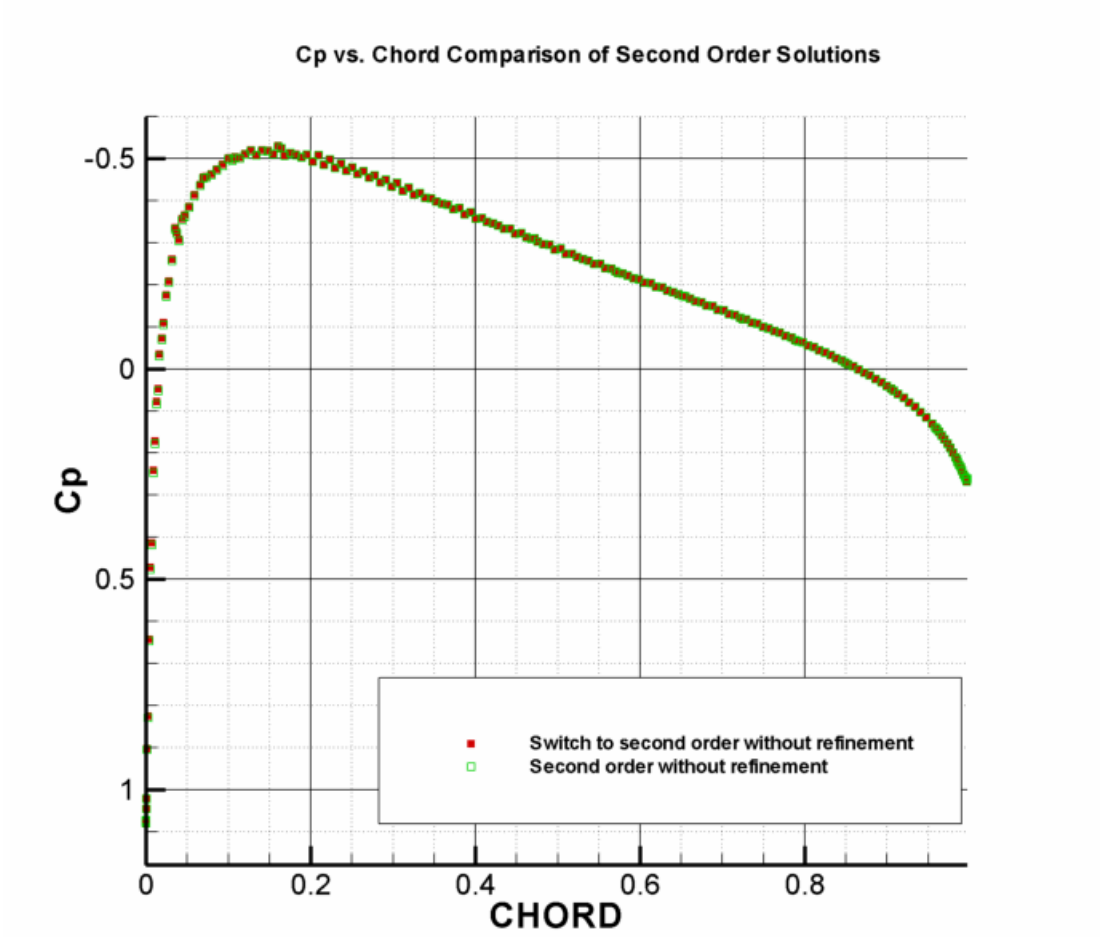

Figure 4.4- Comparison of the second order solutions

In Figure 4.4, it is almost impossible to distinguish between the two solutions. The same situation also prevails for a solution with refinement. Hence it can be said that in terms of accuracy there is no difference between the two solutions.

The Mach contours for the second order solution can be depicted as in Figure 4.5.

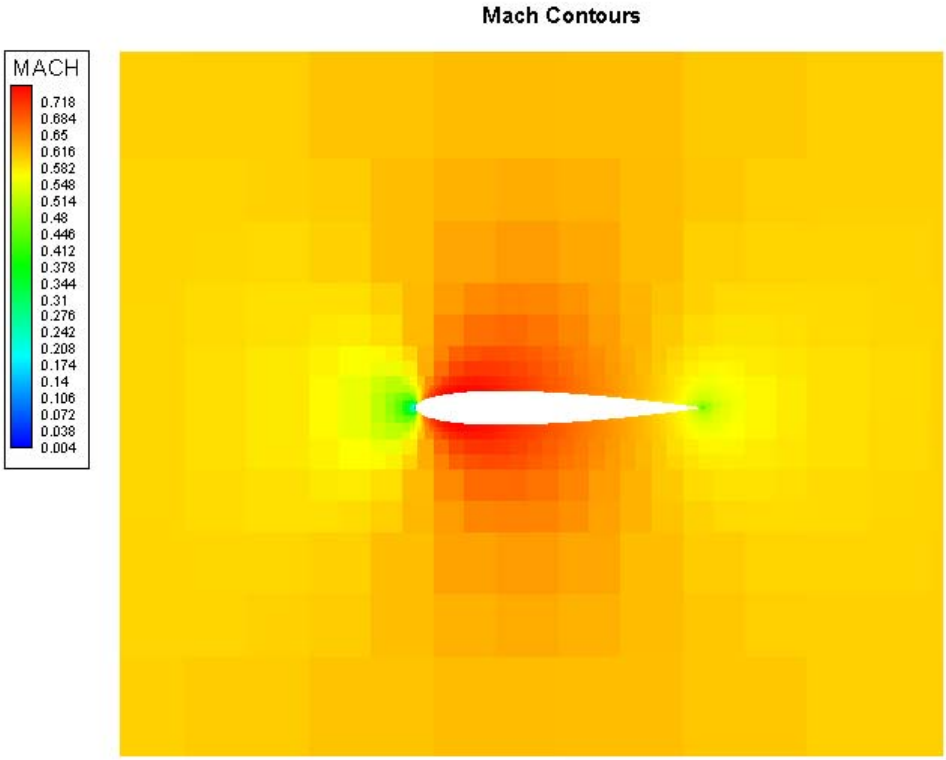

Figure 4.5- Mach contours for NACA0012 subsonic flow

After comparing the first and second order methods in terms of accuracy, their computational performances can also be compared as in Table 4.1.

Table 4.1- Comparison of first and second order solutions

Method	Number of Iterations	Time
First order without refienement	1938	45sec
First order with refienement	2691	2min 37sec
Second order without refinement	4325	11min 23sec
Second order with refinement	7490	1hr 1min 36sec
Switch to second order without refinement	3236	6min 57sec
Switch to second order with refinement	4425	25min 24sec

Naturally the first order solution converges much faster than the second order methods, but it would not be reasonable to obtain a solution with this method due to poor accuracy. As observed from Table 4.1, starting the solutions first order then switching to second order after some level of convergence, decreases the computation time considerably compared to full second order solution. Also as illustrated in Figure 4.4, there is almost no difference between these solutions.

The calculations for the second case of subsonic flow around the NACA0012 airfoil were performed with a Mach number of 0.4167. By changing the angle of attack values a lift coefficient vs. angle of attack graph was constructed. To obtain the solution Roe's method was used and solution refinement wass not employed.

Since the pressure is the main factor determining the lift force at high speeds, it is expected to get a good agreement with the experimental data extracted from (34) until flow separation, a viscosity governed phenomena, is encountered. This expectation is realized as can be seen from Figure 4.6 within the region where there is no separation.

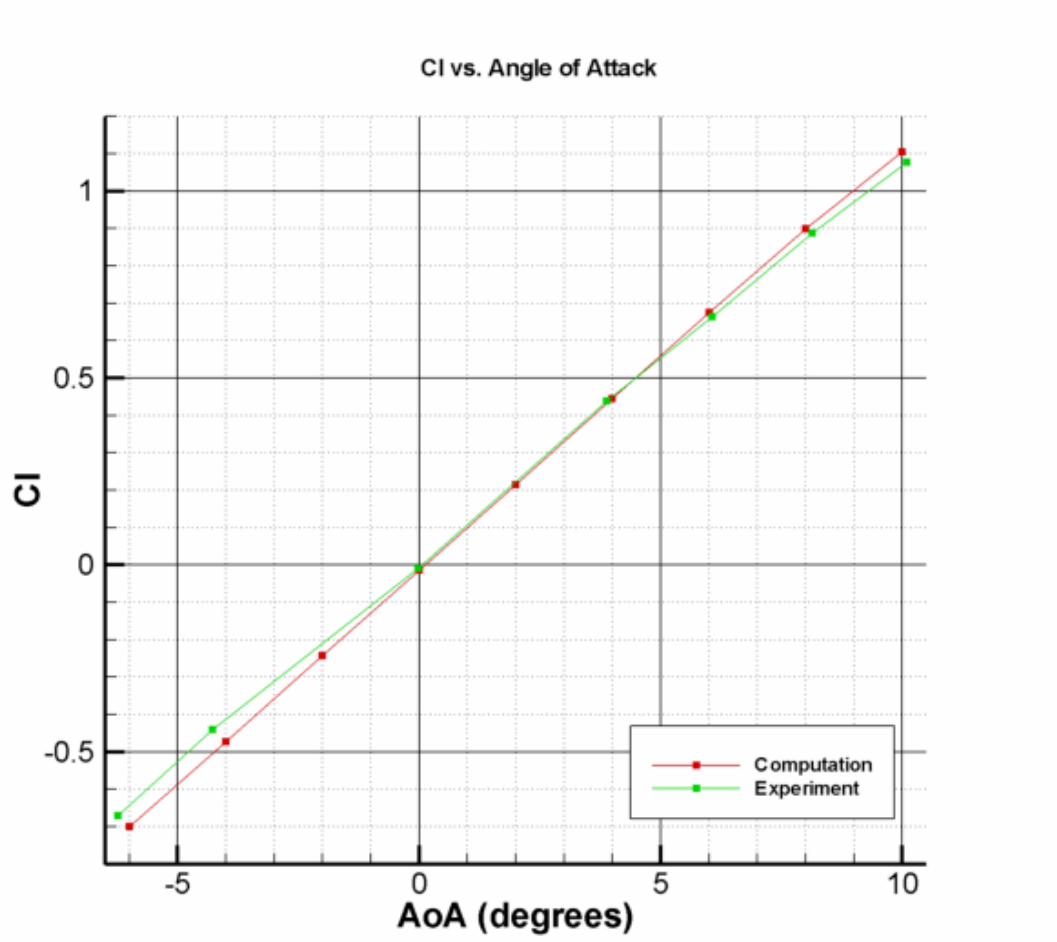

Figure 4.6- Lift coefficient vs. angle of attack graph

To obtain the results presented in Figure 4.6, first order calculations are performed until some level of convergence is obtained then the solution is switched to second order. As discussed earlier this method decreases computation time while there is no loss in terms of accuracy.

It was also attempted to use a fully second order solution to obtain the results. It was possible to get solutions within the range of angle of attacks from -6˚ to 8˚. However for larger angle of attack values than 8˚, divergence in the calculations was observed. Using the first order solution then switching to second order provided results for angle of attack values of 10˚, 12˚ and 16˚ also. The results obtained for 12˚ and 16˚

are not presented in Figure 4.6 since they are related to a flow with separation and this case must be treated with a viscous solver. However this fact still indicates that the first order solution is more stable than the second order one. When the residual plots for first and second order solutions are investigated, an indication of this fact can be seen. In Figure 4.7, it is observed that the residuals decrease smoothly for the first order solution while for the second order one there are a lot of scattering and oscillations as the residuals decrease.

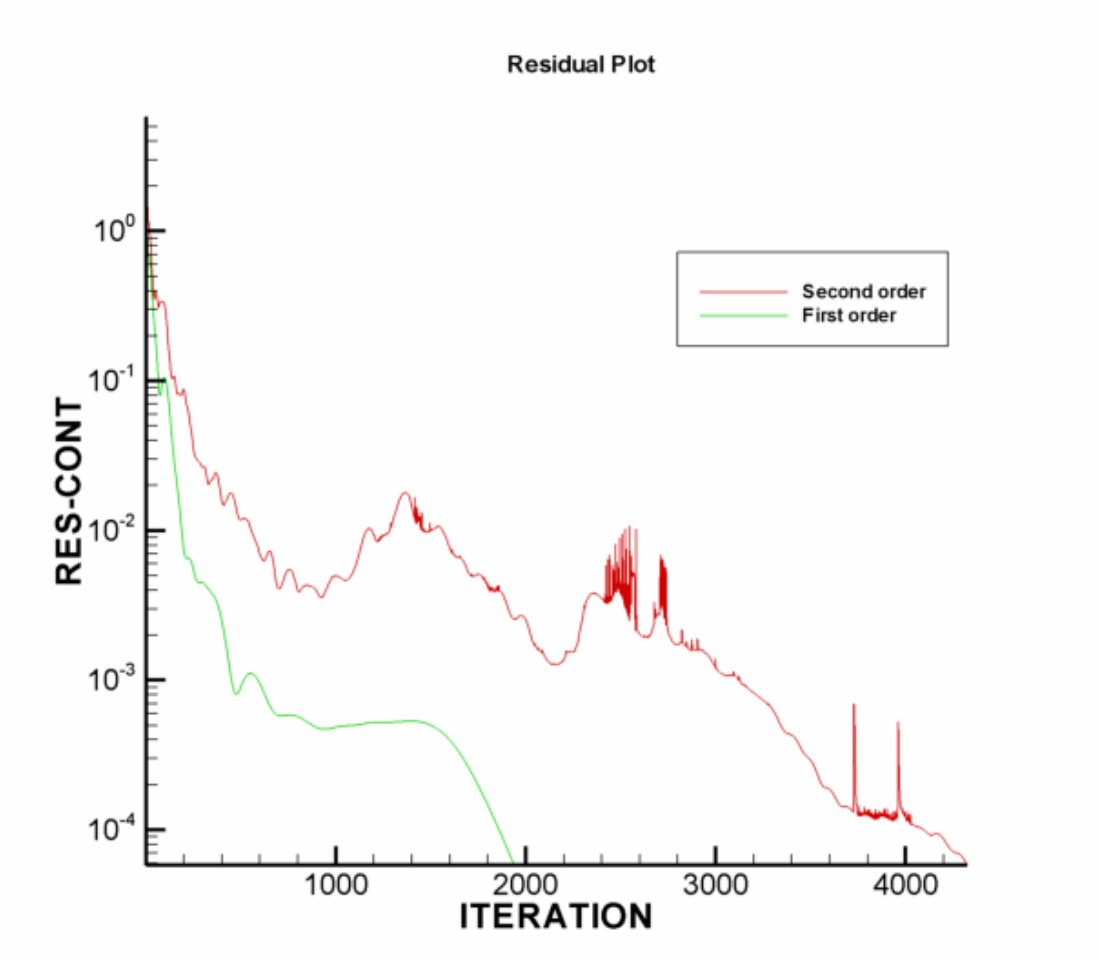

Figure 4.7- Residual plot for first and second order solutions

By employing the first order method until some level of convergence is obtained, a first order accurate initialization of the field variables is obtained which eases the

convergence of the second order solution. This procedure will be used by default for the rest of the calculations that will be presented.

4.1.2 Transonic Tests

The far-field conditions for the transonic flow tests around the NACA0012 profile are a free stream Mach number of 0.85 and an angle of attack of 1˚. For this flow shocks on the upper and lower surface of the airfoil is expected, the one on the upper surface being stronger. Each one of the five methods implemented for the evaluation of the flux terms in the governing equations has been employed in the solution to compare these methods. The most crucial point in the tests performed is the location of the shocks. The transonic flow is a more challenging case than the subsonic flow. Hence the performance of different methods to evaluate the flux terms is compared for this case. The calculations have been performed both with and without solution refinement. To verify the computational solution, AGARD data (35) has been extracted from (14).

To compare the accuracy of the different methods for evaluating the fluxes, calculations with solution refinement have been performed. First the results obtained from the AUSM and its derivative methods are compared amongst themselves. The pressure coefficient vs. the chord graph for these methods is illustrated in Figure 4.8.

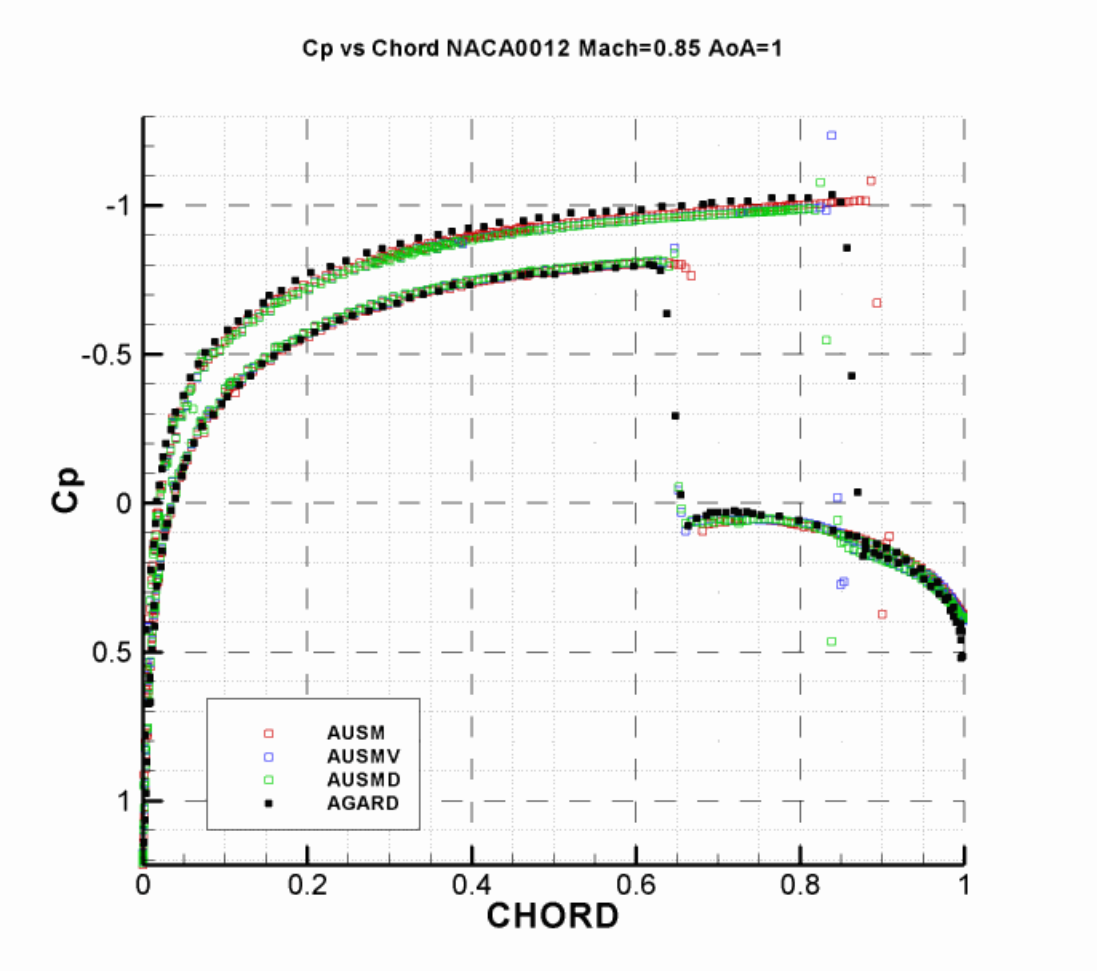

Figure 4.8- Pressure coefficient vs. chord graph for the AUSM methods

It is observed from Figure 4.8 that the AUSMD and AUSMV methods capture the location of the weaker shock on the lower surface while the AUSM predicts this location slightly downstream. On the upper surface none of the methods were able to capture the shock location exactly. The AUSMD and the AUSMV methods provide a closer estimation of the shock location on this surface than the AUSM method. All of the methods exhibit oscillations around the shock location, the ones on the upper surface being more marked. This is due to the performance of the limiter in the calculation of the fluxes.

The Roe's method and the van Leer method can be compared with one of the representative AUSM methods. The AUSMV method providing the most accurate results among the AUSM methods is chosen as the representative AUSM method and the pressure coefficient vs. chord graph for these methods is illustrated in Figure 4.9.

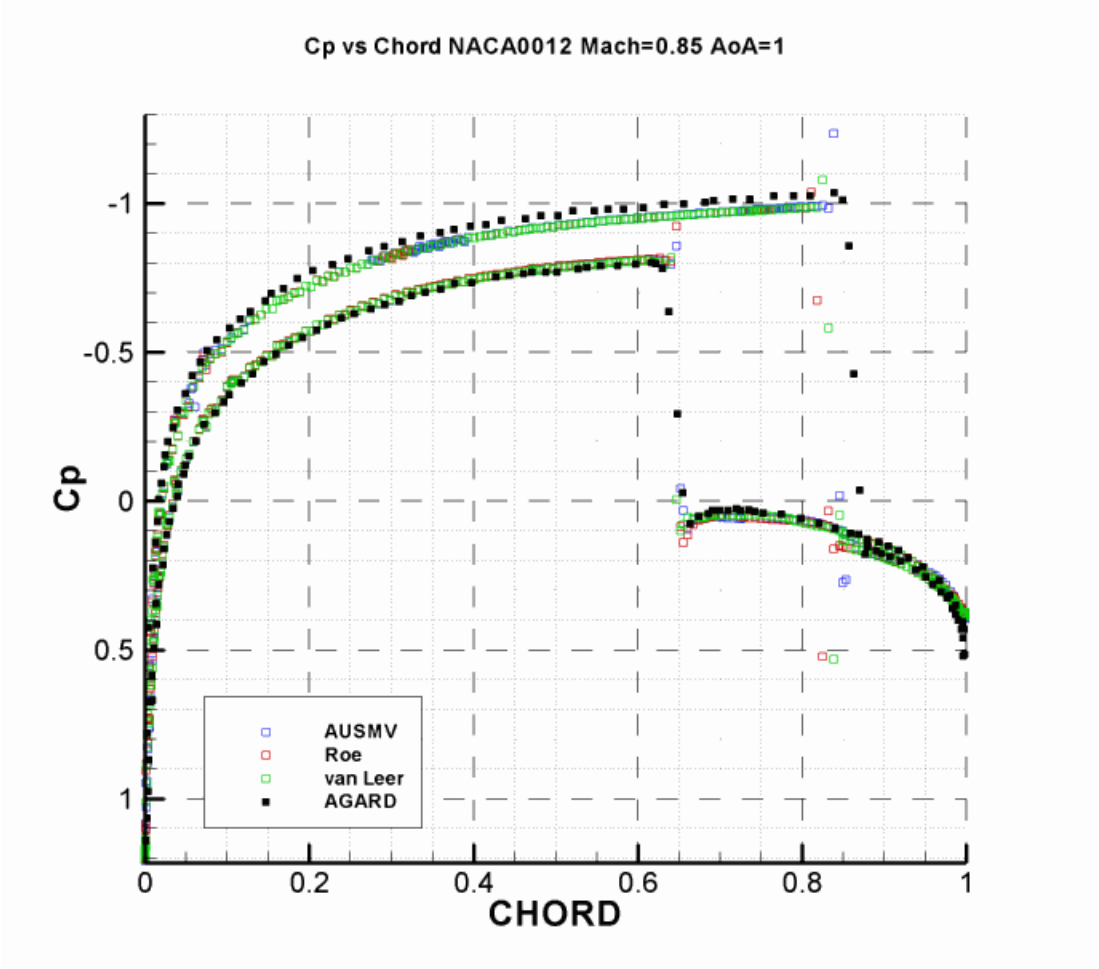

Figure 4.9- Pressure coefficient vs. chord graph for Roe, van Leer and AUSMV

It is seen that both the Roe's method and the van Leer's method estimate the shock location at a slightly upstream position on the upper surface while there is good agreement on the lower surface. The oscillations around the shock locations are also

inherent in these methods. In terms of accuracy AUSMD, AUSMV and the van Leer's methods provide the best results for this particular test case.

Besides the accuracy of the methods, their convergence characteristics should also be examined. The convergence criterion is that the residual for the continuity equation calculated in the first step should drop five levels on a log scale. None of the methods were able to provide a five level drop in the residual for solution adaptive calculations. Hence to compare the convergence characteristics calculations without solution refinement have been performed. The calculations were performed with four different CFL safety coefficients; 1.0, 0.5, 0.2 and 0.1, four each one of the five methods. In Table 4.2, the results for the solution with the maximum CFL safety factor providing a convergent solution has been presented.

Table 4.2- Computational characteristics of the methods for evaluating fluxes

Method	Convergence	Number of Iterations	Calculation Time	CFL Safety Coefficient
AUSM	converges	5555	9min 1sec	1.0
AUSMD	oscillates	100000	3hr 35min 4sec	0.1
AUSMV	converges	9646	16min 19sec	0.5
Roe	converges	5207	9min 15sec	1.0
van Leer	diverges	-	-	-

The AUSM and the Roe's methods converged with a CFL safety coefficient of 1.0 while the AUSMV method converged with a CFL safety factor of 0.5. For the AUSMD method with a CFL safety factor of 0.1, the residual of the continuity equation oscillates around $8x10^{-4}$ corresponding to a residual drop of about four levels after about 60000 steps till the maximum number of iterations of 100000. The van Leer method diverges when solution refinement is not applied implying a relation between the method and the mesh size. The residual plots for the convergent solutions can be depicted as in Figure 4.10.

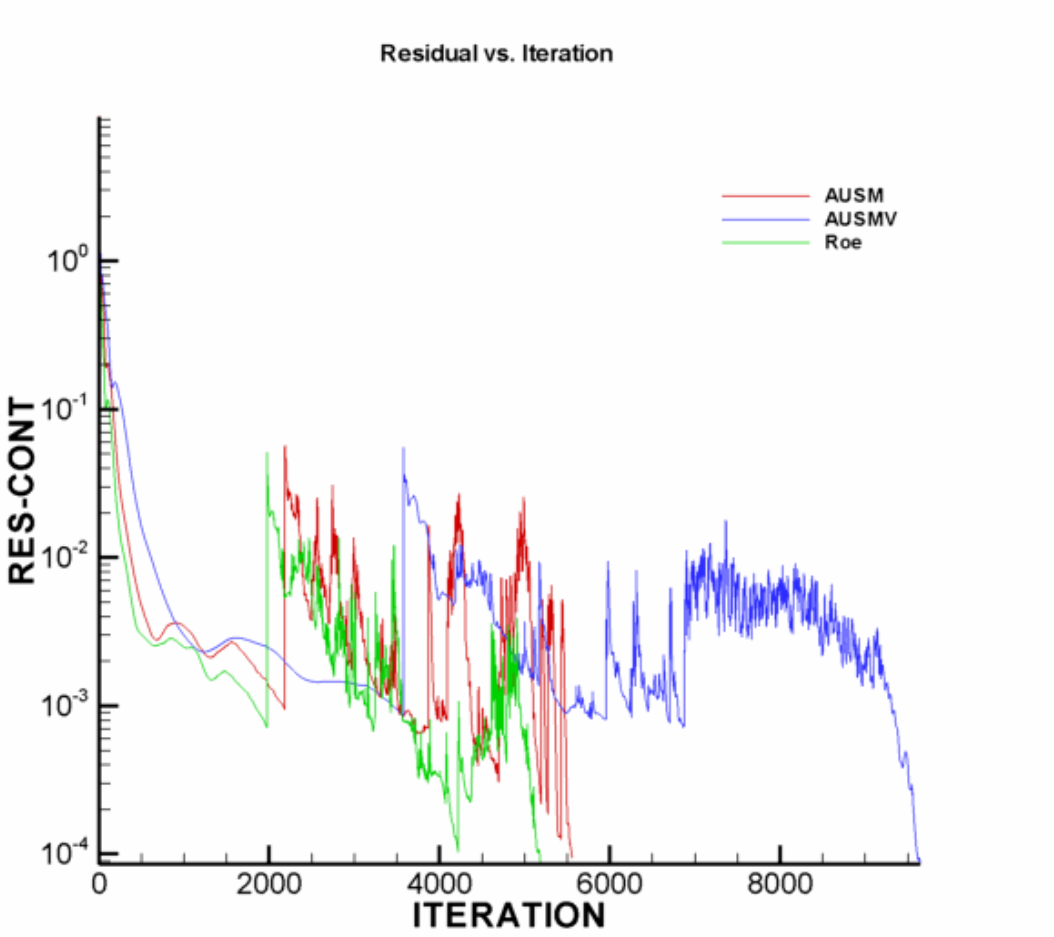

Figure 4.10- Residual plot for transonic flow

It is also possible to show the effect of solution adaptation on the mesh generated initially. The solution refinement has been performed every time the residuals dropped to one twentieth of the initial residual which is updated just before solution adaptation is performed. The effect of mesh generation in the critical regions around the airfoil is illustrated in Figure 4.11.

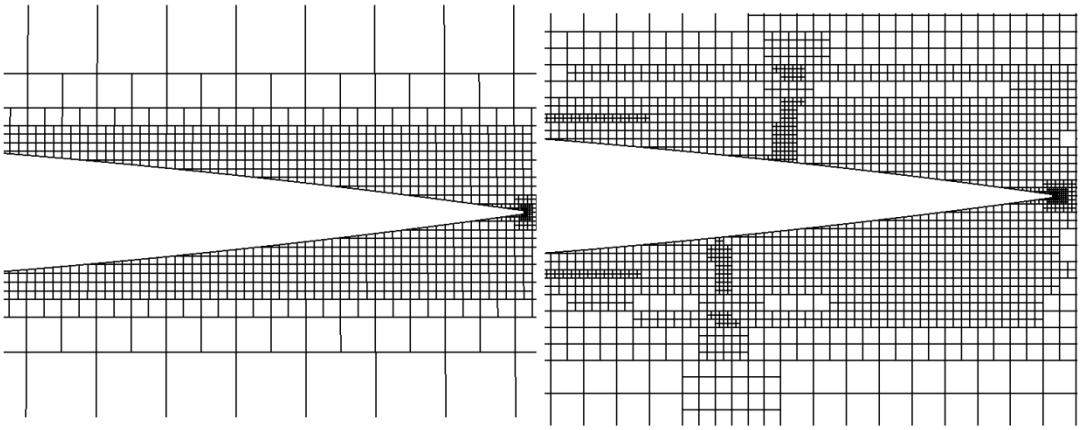

Figure 4.11- Effect of refinement at shock location

As can be seen from Figure 4.11, the mesh is refined around the location of the shock since there are large gradients in the flow variables at this location. Another region where large gradients are observed is at the nose of the airfoil around the stagnation point. The effect of solution refinement in this region is illustrated in Figure 4.12.

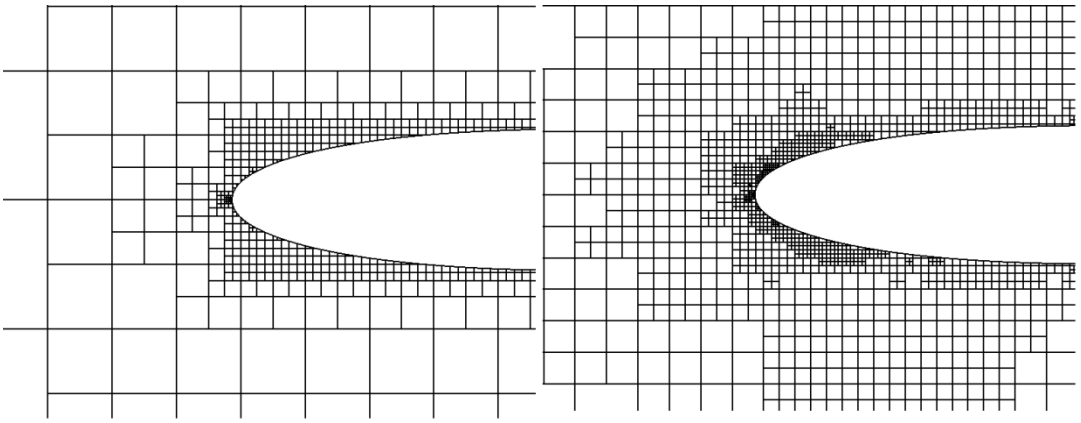

Figure 4.12- Effect of refinement around stagnation point

The effect of solution adaptation can be illustrated by plotting the Mach contours for a refined and non-refined solution.

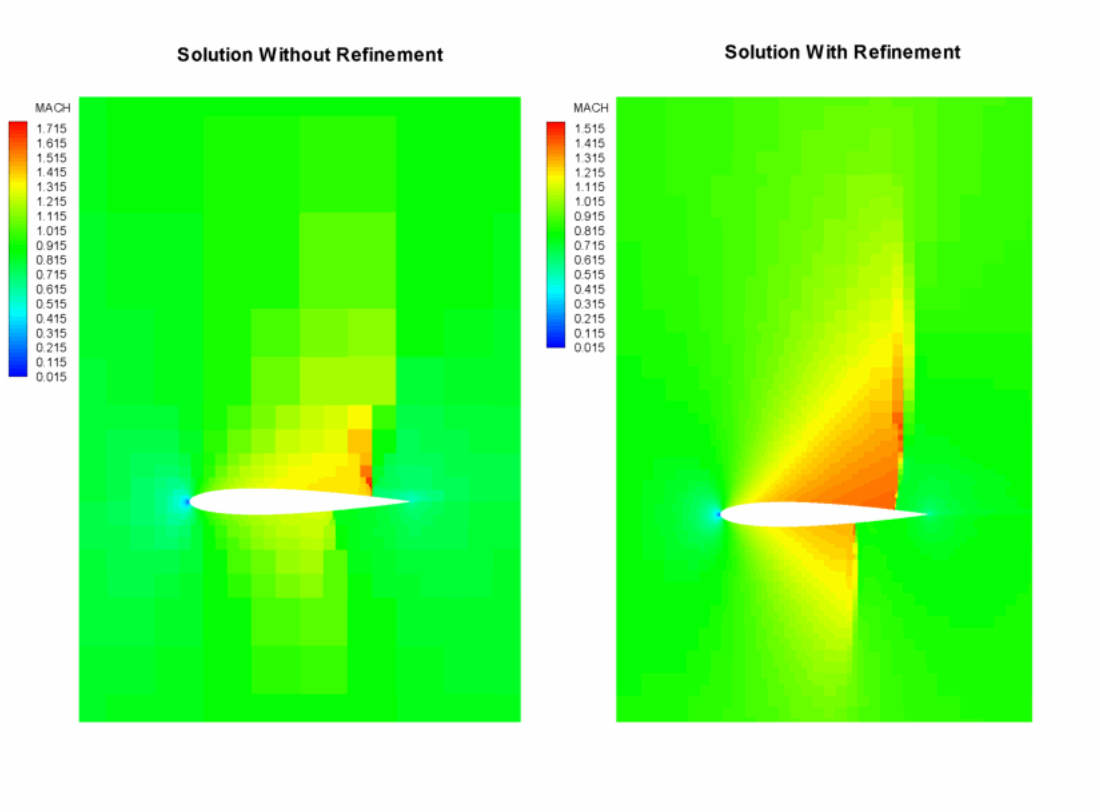

Figure 4.13- Mach contours for transonic flow around NACA0012 airfoil

In Figure 4.13, the Mach contours obtained with the AUSMV method are displayed. As can be observed for the solution without refinement, the shocks are smeared. The pressure coefficient vs. chord graphs of these solutions can also be displayed. In Figure 4.14, it is seen that the solution obtained without refinement is able to capture both the pressure distribution on the airfoil and the shock locations with refinement introducing a slight improvement on both aspects. However in Figure 4.13, it is seen that the overall flow field is not represented accurately without solution refinement. Hence it can be said that if the main concern is obtaining the forces on the airfoil, the solution without refinement will provide a good estimation in a considerably shorter amount of time.

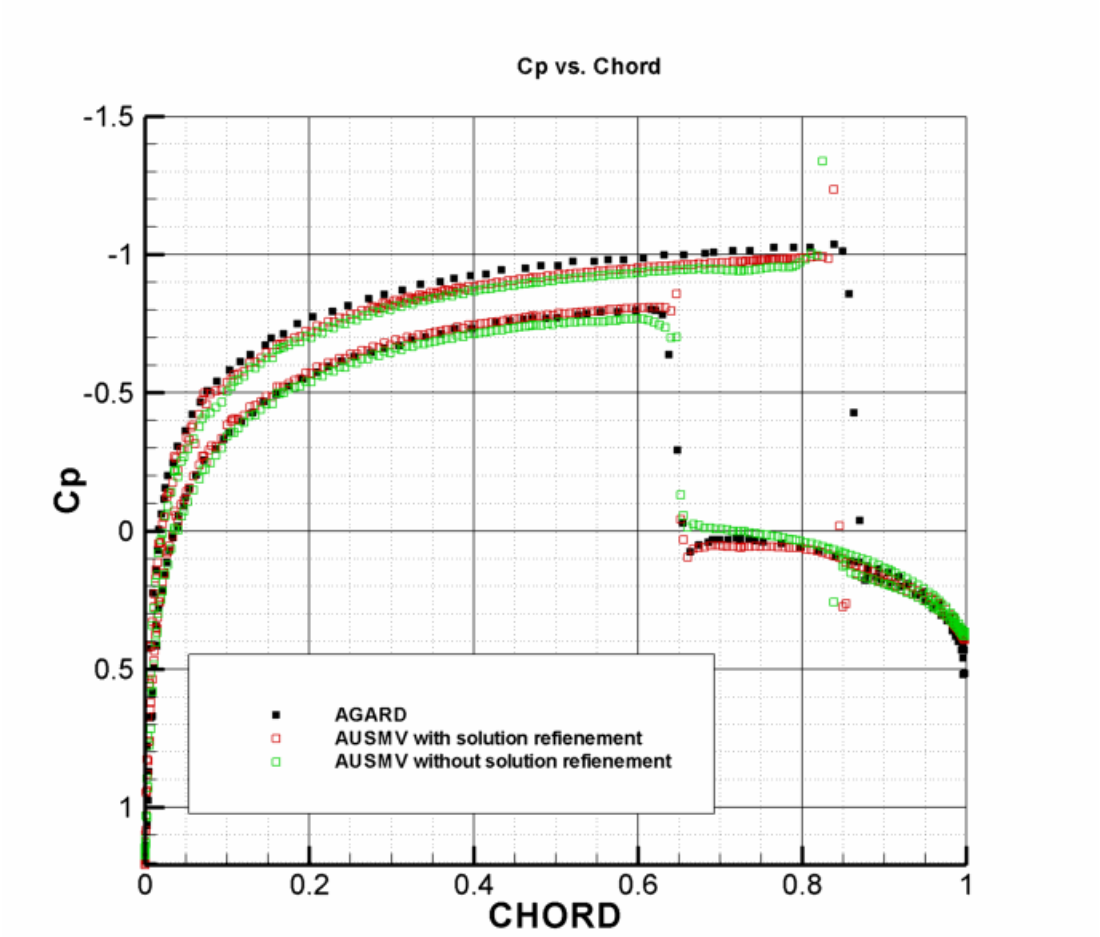

Figure 4.14- Pressure coefficient vs. chord for AUSMV with and without refinement

4.2 NLR 7301 with Flap

The NLR 7301 tests have been performed for a gap of 2.6% percent of chord length, an overlap of 5.3% of chord length and a flap angle of 20˚. The definition of these variables can be shown as in Figure 4.15.

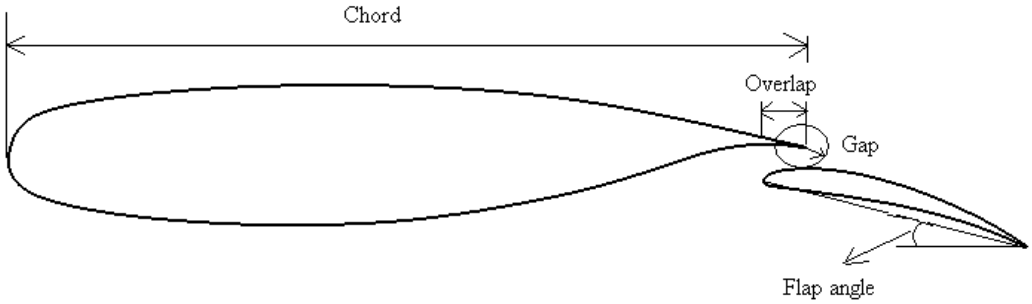

Figure 4.15- Definition of geometry variables for NLR 7301 with flap

Tests were performed at three different angle of attack values; 6˚, 10.1˚ and 13.1˚. The free stream Mach number for all the cases was 0.185. The five methods; Roe, van Leer, AUSM, AUSMD, AUSMV, have been employed in the calculations. To verify the results computed, data obtained from (36) has been used.

The pressure coefficient vs. chord graph for angle of attack of 6˚ is presented for the AUSM methods in Figure 4.16. All of the AUSM methods are able to capture pressure distribution with good accuracy for the most part. But in terms of capturing the peak of the pressure coefficient on the upper surface of the main airfoil, AUSM method is superior to the others. The AUSMD method performs better than the AUSMV method on this aspect.

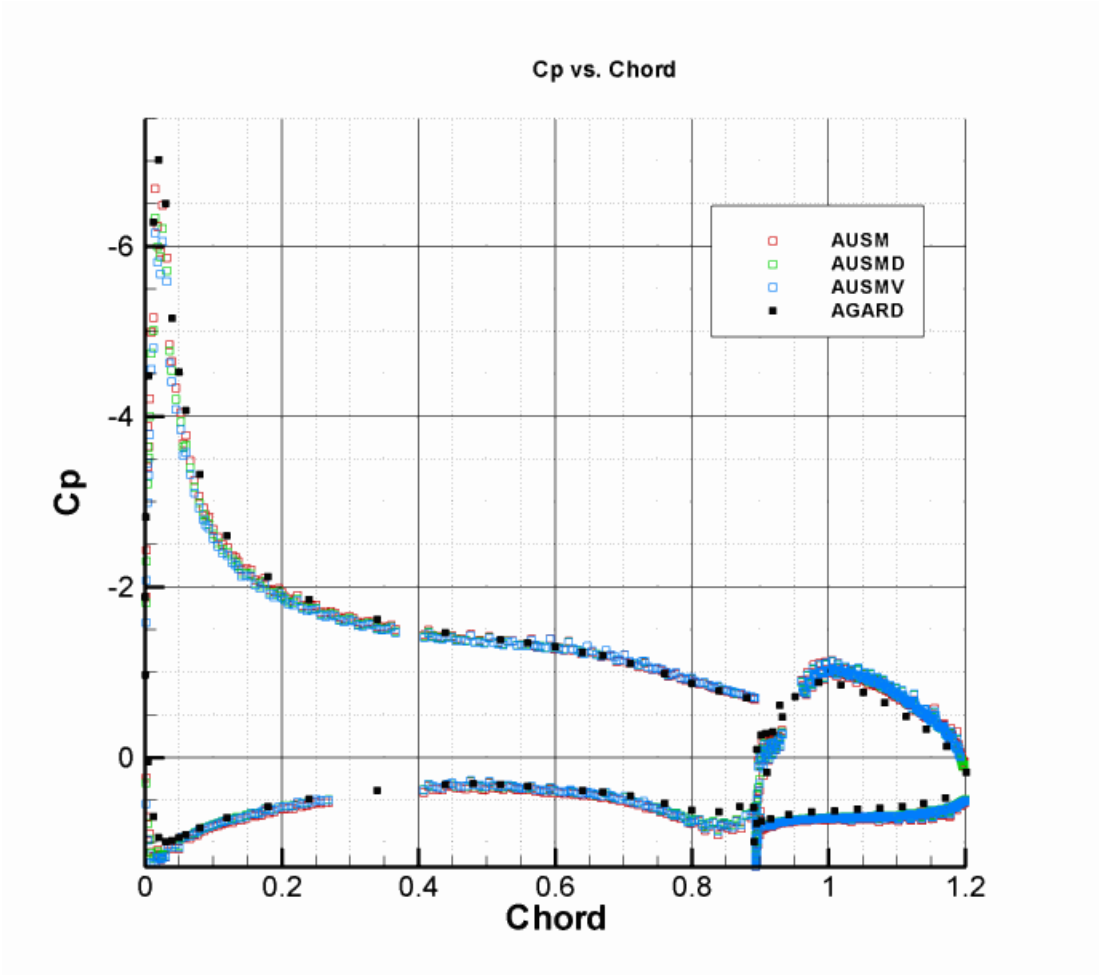

Figure 4.16- Pressure coefficient vs. chord graph (AUSM methods AoA 6˚)

The pressure coefficient vs. chord graph can also be constructed for the Roe's, van Leer's and AUSM methods. In Figure 4.17, it is seen that the AUSM method provides better results than both the Roe's and van Leer's methods. The solution by Roe's method is comparable to the other AUSM methods. In terms of capturing the peak of the pressure coefficient on the upper surface of the main element, Roe's method performs similar to the other method while van Leer provides the poorest result in terms of accuracy.

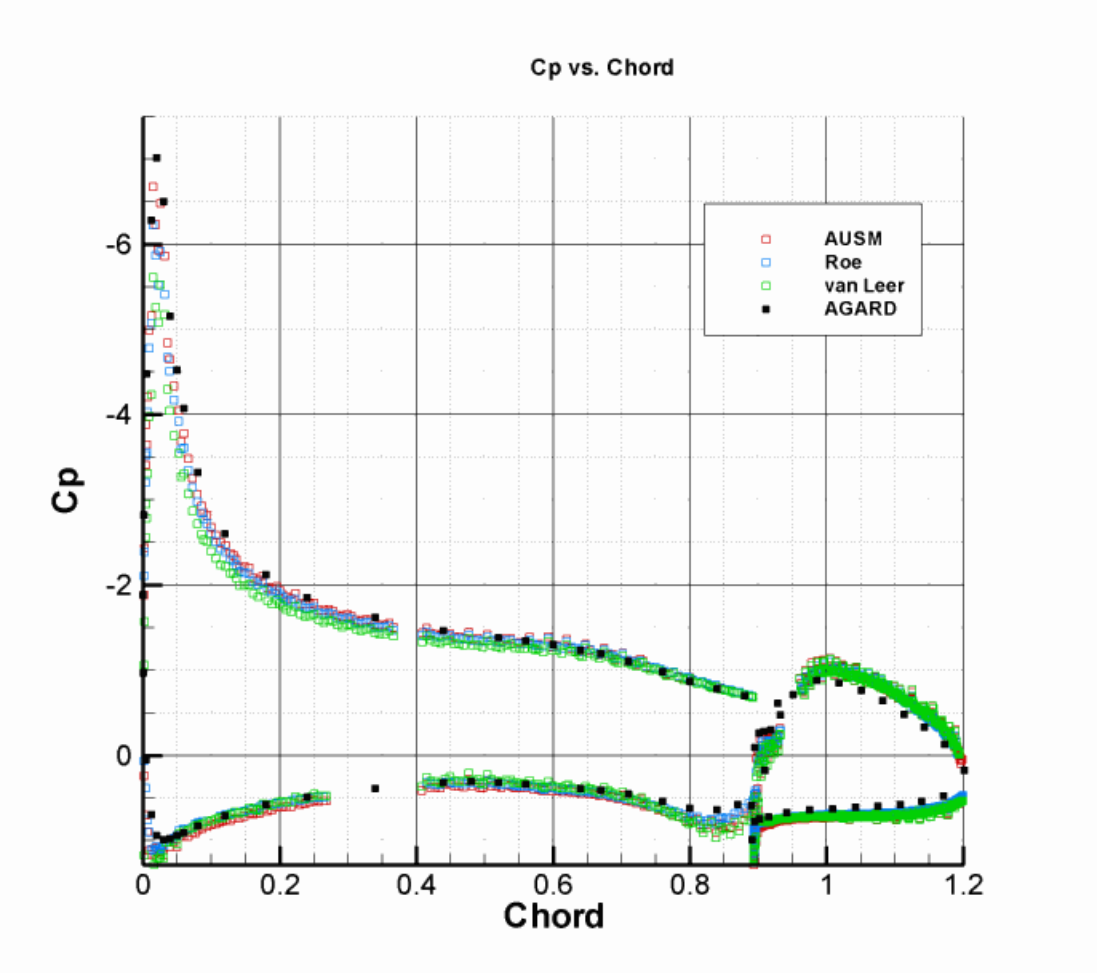

Figure 4.17- Pressure coefficient vs. chord graph (AUSM, Roe, van Leer AoA 6˚)

The computational performances of each method can be tabulated to obtain a comparison.

Table 4.3- Computational performance of the methods for NLR 7301 AoA 6°

Method	Convergence	Number of Iterations	Time	Lift Coefficient
AUSM	converges	7072	41min 47sec	2.51
AUSMD	oscillates	100000	10hr 21min 49sec	2.46
AUSMV	oscillates	100000	10hr 14min 0sec	2.45
Roe	oscillates	100000	10hr 56min 15 sec	2.42
van Leer	converges	4172	22min 53sec	2.35

It is observed from Table 4.3 that the van Leer's method converges faster than the AUSM method. The other methods; AUSMD, AUSMV and Roe, do not converge, that is the residuals in the continuity equation do not drop five levels but they fluctuate until the maximum number of iterations is reached. Also it can be seen that the highest lift coefficient is found with the AUSM method. This is an expected result as the AUSM method captures the peak of the pressure distribution on the upper surface of the main airfoil better than the other methods. The AUSMD, AUSMV and Roe's methods provide a similar result on this aspect while van Leer's method gives the smallest estimate as it was the worst in capturing the peak.

The pressure coefficient vs. chord graph for the angle of attack value of 10.1 can be presented for the AUSM methods. From Figure 4.18, it is seen that the performance of the AUSM method is better than both the AUSMD and the AUSMV methods. The AUSMV method starts to deviate from the AGARD data which is especially apparent on the upper surface of the flap. The peak of the pressure coefficient is captured accurately with the AUSM method.

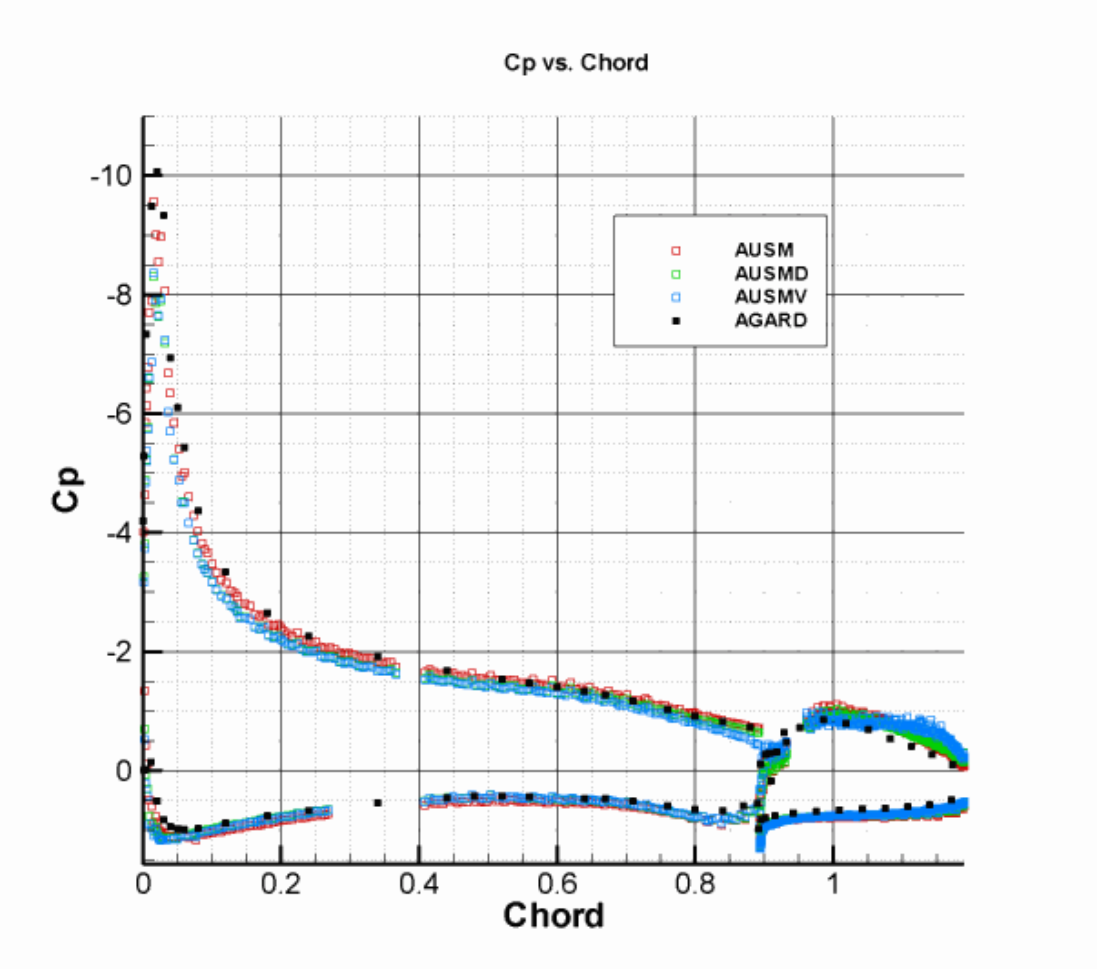

Figure 4.18- Pressure coefficient vs. chord graph (AUSM methods AoA 10.1˚)

The pressure coefficient vs. the chord graph can be presented for the AUSM, Roe and van Leer methods as in Figure 4.19.

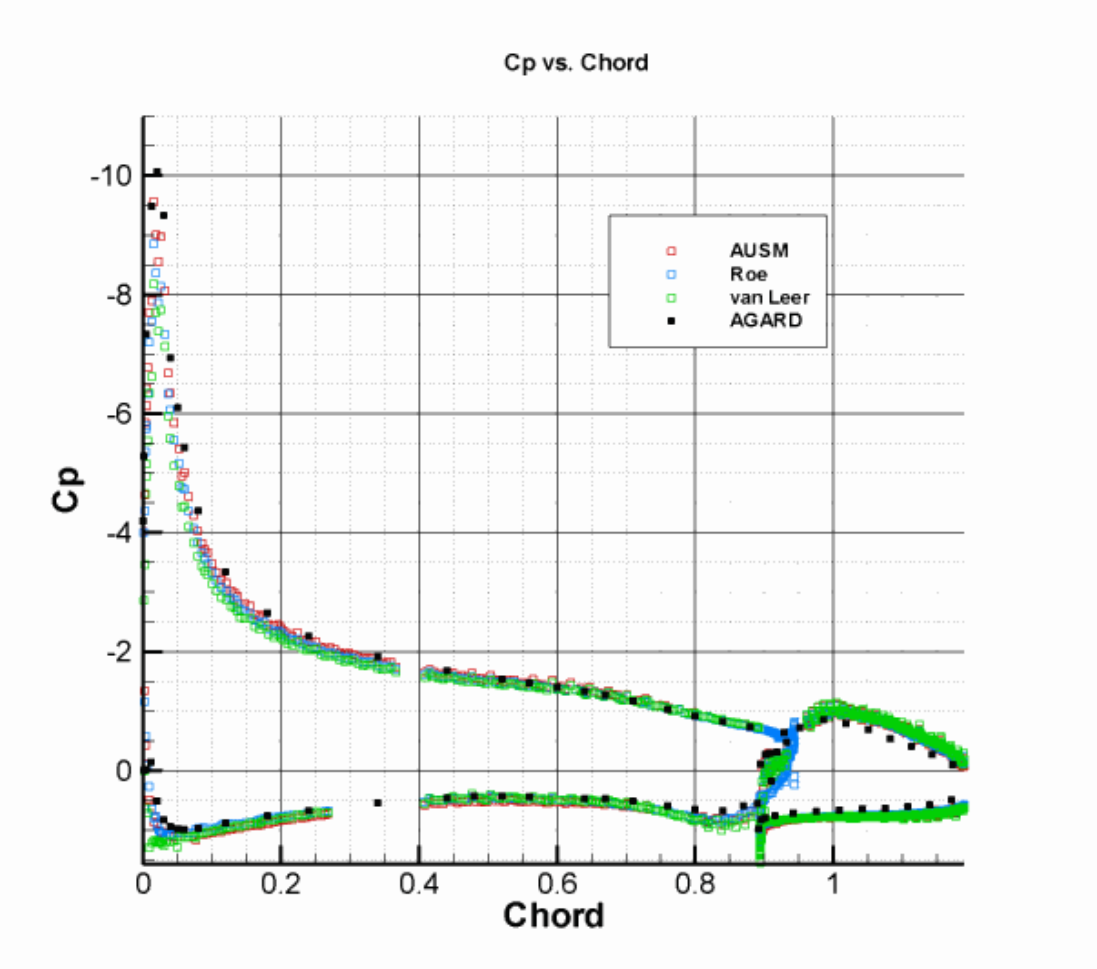

Figure 4.19- Pressure coefficient vs. chord graph (AUSM, Roe, van Leer AoA 10.1˚)

As can be seen from Figure 4.19, AUSM method provides a better solution. It is also observed that the Roe's method provides a better estimation of the peak in the pressure distribution on the upper surface of the main element than the AUSMD and AUSMV methods.

The computational performance of the methods can also be compared from Table 4.4.

Table 4.4- Computational performance of the methods for NLR 7301 AoA 10.1˚

Method	Convergence	Number of Iterations	Time	Lift Coefficient
AUSM	converges	11567	1hr 10min 43sec	2.98
AUSMD	oscillates	100000	10hr 21min 5sec	2.76
AUSMV	oscillates	100000	10hr 13min 2sec	2.75
Roe	converges	78924	8hr 15min 47 sec	2.86
van Leer	converges	4175	22min 50sec	2.83

It is observed from Table 4.4 that as the angle of attack is increased Roe's method converges like the AUSM and the van Leer methods. The performances of the van Leer, AUSMD and AUSMV methods essentially remain the same computationally. The Roe's method being able to capture the pressure peak better for this case, estimates a relatively higher lift coefficient than the previous case. The AUSM method still being the best one to capture the peak provides the highest estimate of the lift coefficient.

The pressure coefficient vs. the chord graph can be constructed for the angle of attack of 13.1˚ for the AUSM methods. From Figure 4.20, it is seen that the AUSMV method fails at this angle of attack. Once again the AUSM method provides a considerably better estimate of the pressure peak on the upper surface of the main element.

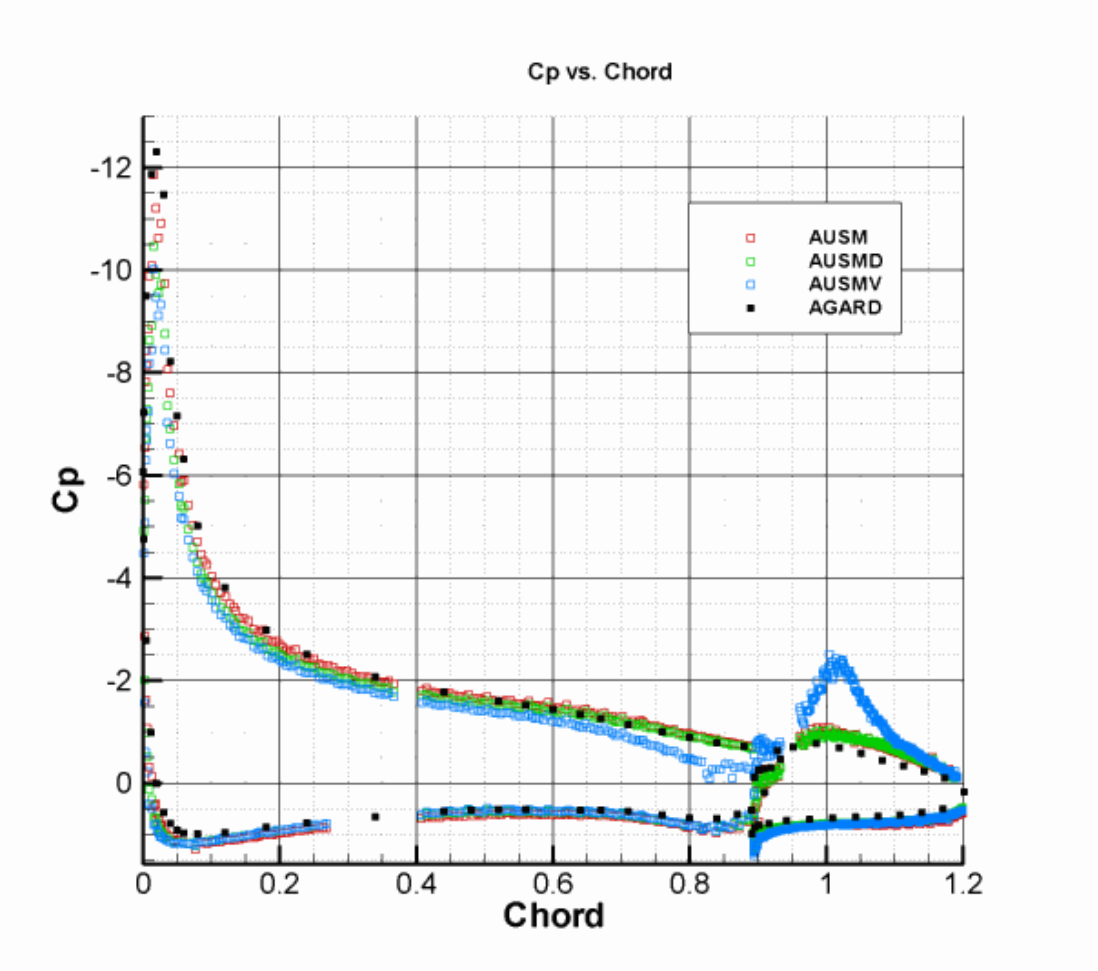

Figure 4.20- Pressure coefficient vs. chord graph (AUSM methods AoA 13.1˚)

In Figure 4.21 the pressure coefficient vs. chord graph for the AUSM, Roe and van Leer methods are depicted. The AUSM method providing the best of the solutions, the Roe's method provides a better solution than van Leer's method. As in the case of angle of attack of 10.1˚, the Roe's method gives a better solution than the AUSMD and AUSMV method which fails.

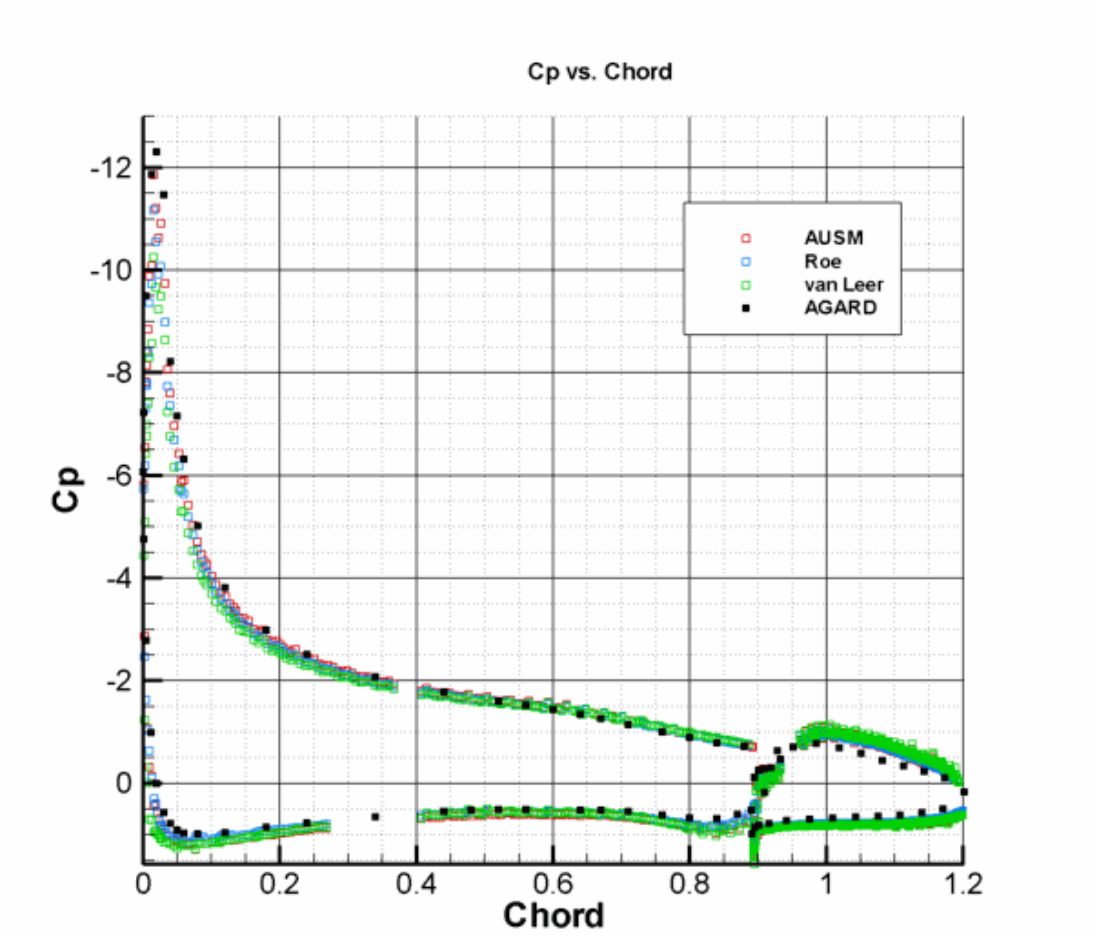

Figure 4.21- Pressure coefficient vs. chord graph (AUSM, Roe, van Leer AoA 13.1˚)

The computational performance of the methods for the case of angle of attack of 13.1˚ can be compared with the aid of Table 4.5.

Table 4.5- Computational performance of the methods for NLR 7301 AoA 13.1˚

Method	Convergence	Number of Iterations	Time	Lift Coefficient
AUSM	converges	12182	1hr 14min 5sec	3.29
AUSMD	oscillates	100000	10hr 20min 30sec	3.08
AUSMV	oscillates	100000	10hr 13min 5sec	3.03
Roe	converges	87222	9hr 11min 9sec	3.17
van Leer	converges	4396	24min 12sec	3.16

The computational performance of the methods is pretty similar to the case of angle of attack of 10.1˚ with the exception that AUSMV method fails totally. It can be concluded that AUSM method provides the best results in all the cases considered. Roe's and van Leer's methods do improve as the angle of attack increases which may be due to the fact that as the angle of attack increases so does the velocities around the airfoil, which makes the problem shift closer to the compressible range. The performance of the AUSMD method remains constant while the AUSMV method fails as the angle of attack is increased.

Solution adaptive calculations have also been performed for the van Leer method to improve the results. The effect of solution refinement on the mesh can be shown as in Figure 4.22 and Figure 4.23.

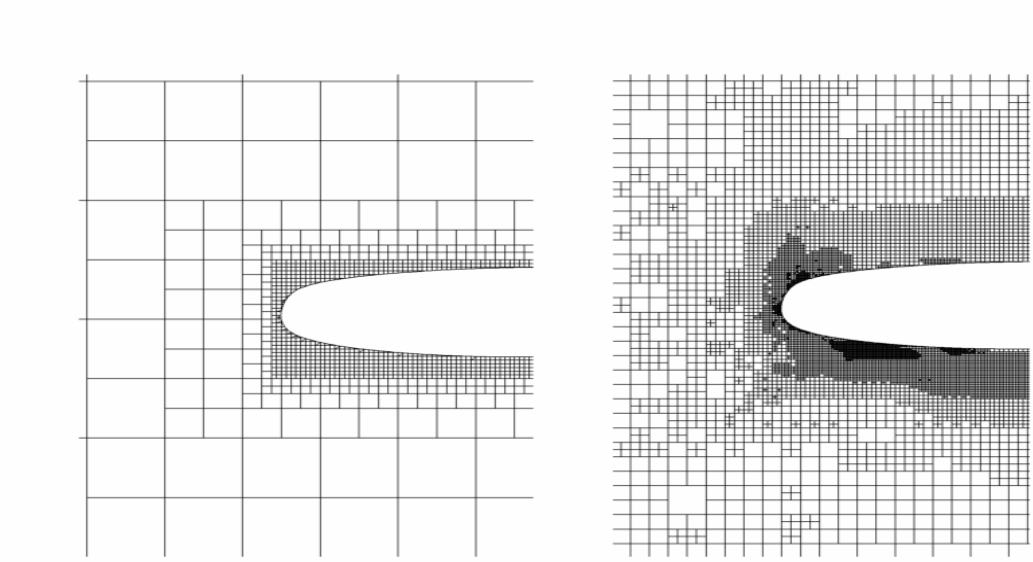

Figure 4.22- Effect of solution refinement around stagnation region of NLR 7301

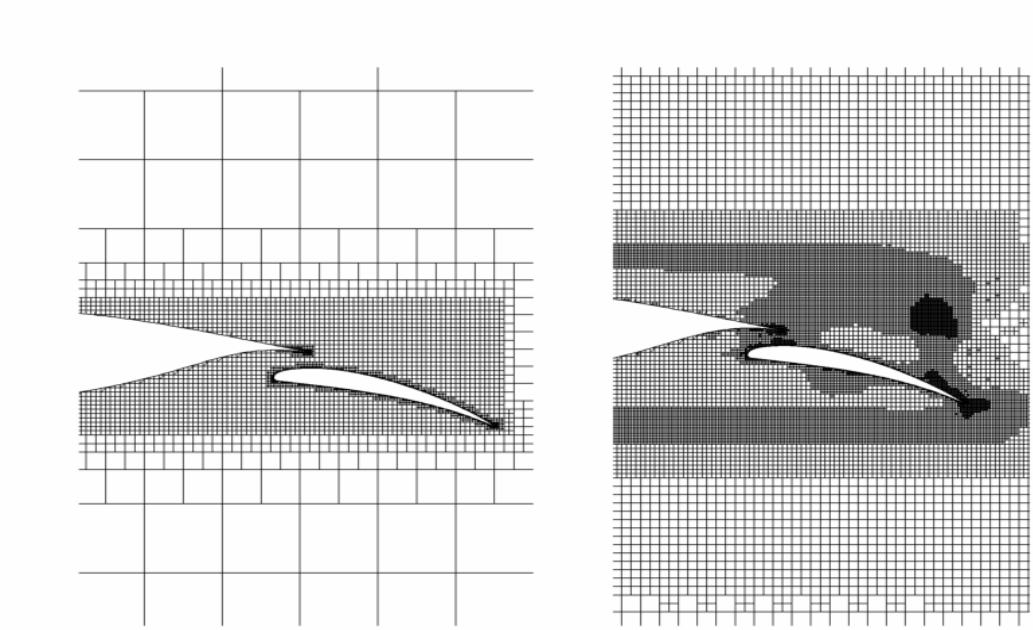

Figure 4.23- Effect of solution refinement around the flap

The pressure coefficient vs. the chord graphs for the solution with and without refinement can be constructed for a comparison at 6˚.

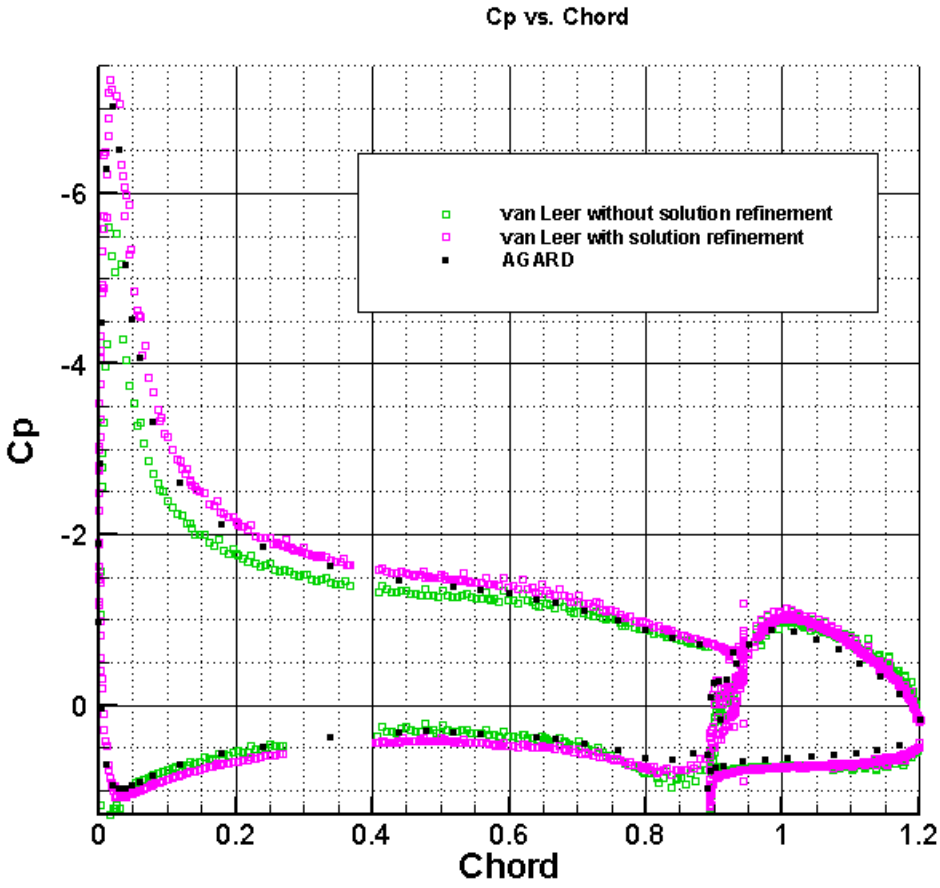

Figure 4.24- Pressure coefficient vs. chord for van Leer AoA 6˚

In Figure 4.24, it is seen that the adapted solution performs better at capturing the peak of the pressure distribution on the upper surface of the main element. In fact the solution is improved around this region as a whole. The estimate of the lift coefficient increases from 2.35 to 2.49. This is much closer to the one predicted by the AUSM method.

The pressure coefficient vs. the chord graph for a solution with and without refinement for angle of attack of 10.1˚ is presented in Figure 4.25.

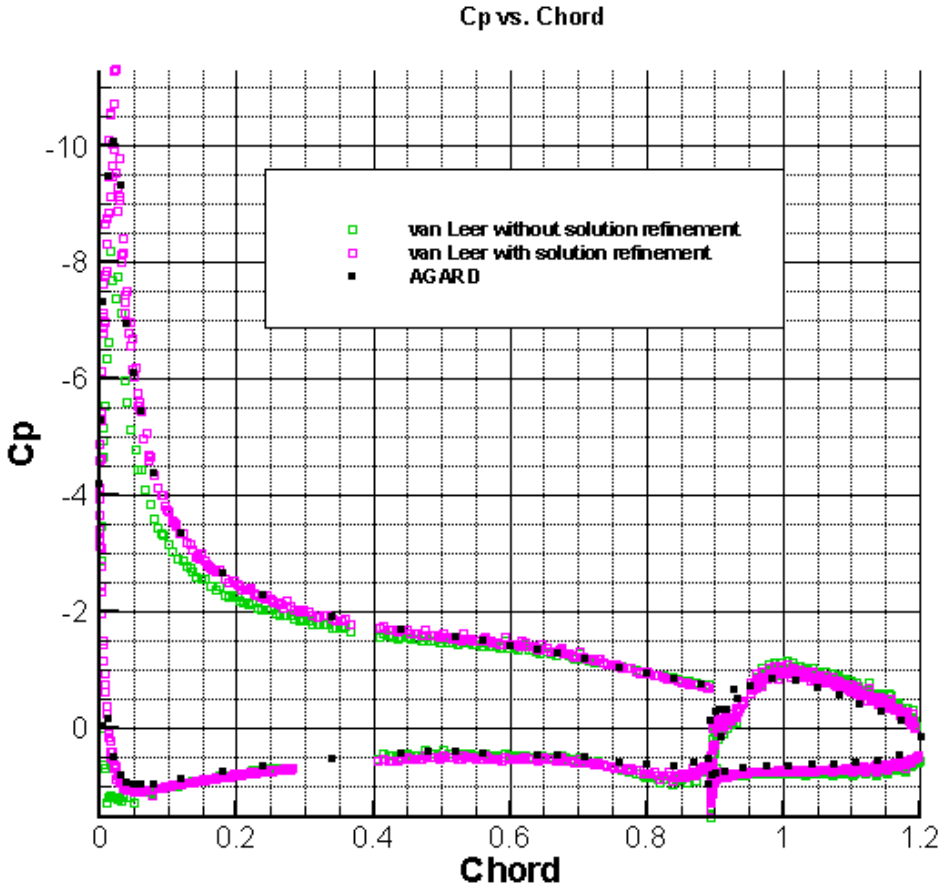

Figure 4.25- Pressure coefficient vs. chord for van Leer AoA 10.1˚

There is an overall improvement of the solution with the introduction of refinement, but this time there is a considerable over estimation of the peak of the pressure coefficient on the upper surface of the main element. In fact the estimation for the lift coefficient becomes 3.05 which is greater than predicted by the AUSM method.

Lastly, the pressure coefficient vs. the chord graph for a solution with and without refinement for angle of attack of 13.1˚ is presented in Figure 4.26.

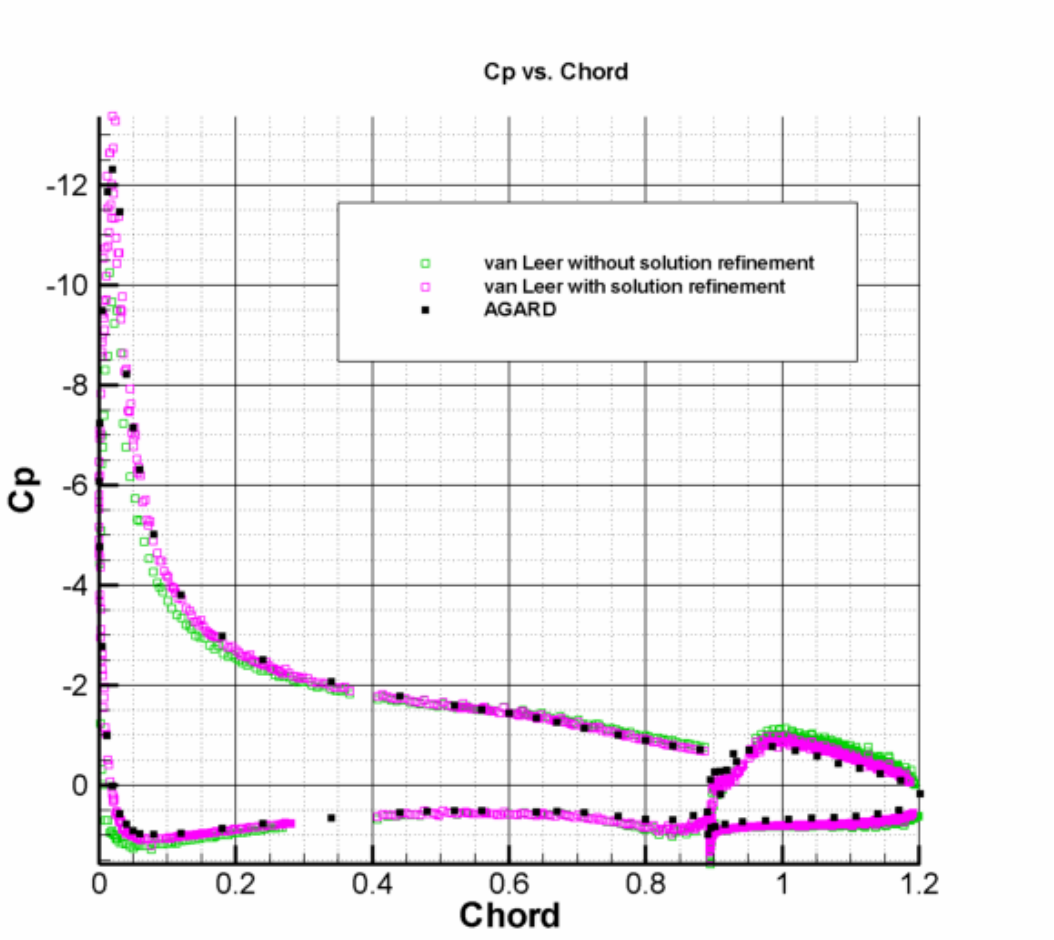

Figure 4.26- Pressure coefficient vs. chord for van Leer AoA 13.1˚

Once again the overall solution does improve, but there is an over prediction of the pressure coefficient peak on the upper surface of the main element.

Figure 4.27, Figure 4.28 and Figure 4.29 illustrate the flow fields obtained for angle of attack values of 6˚, 10.1˚, 13.1˚ respectively.

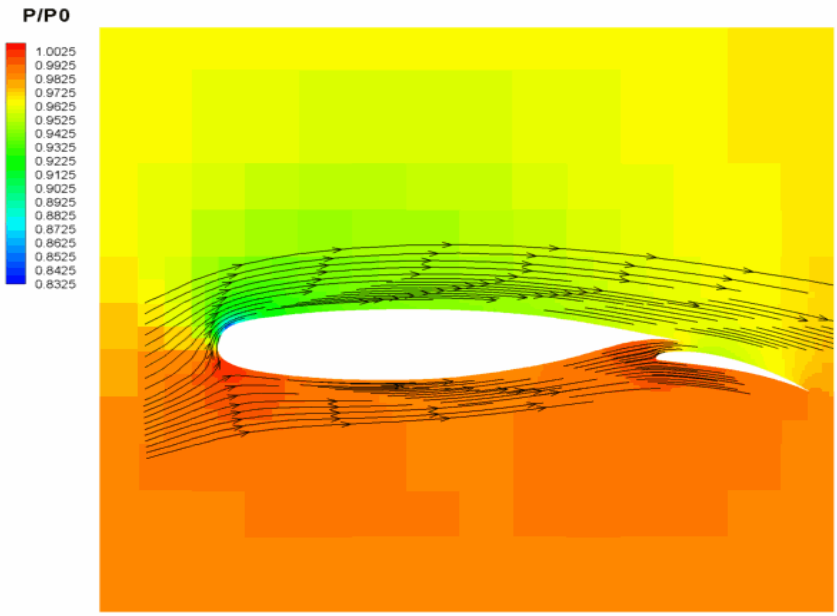

Figure 4.27- Flow field for NLR 7301 with flap AoA 6˚

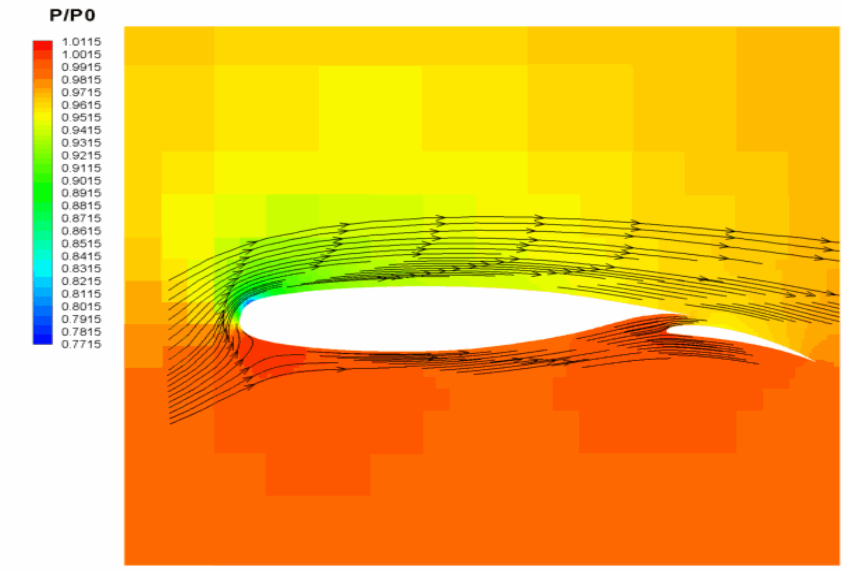

Figure 4.28- Flow field for NLR 7301 with flap AoA 10.1˚

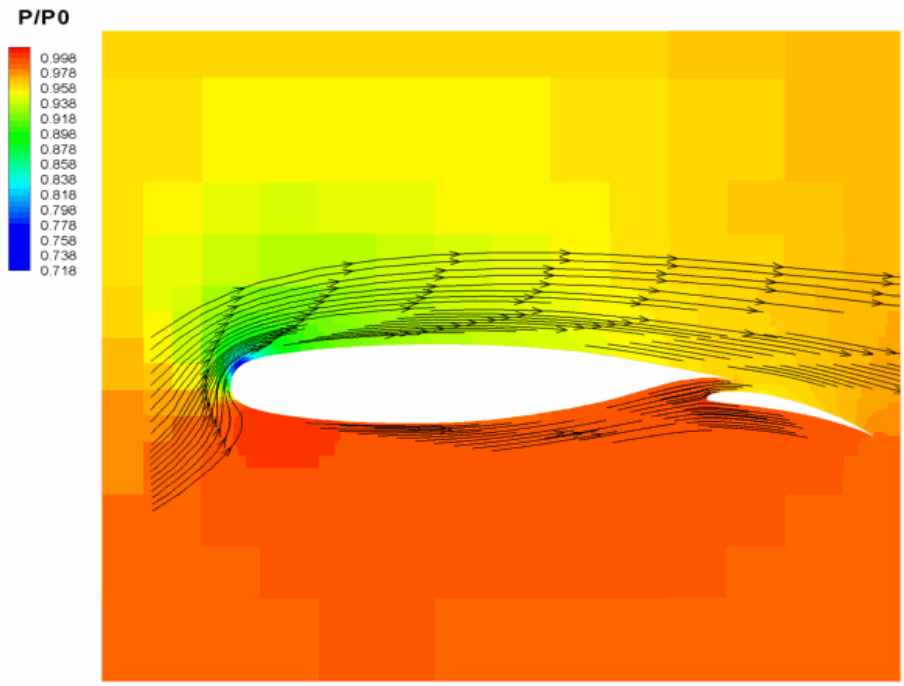

Figure 4.29- Flow field for NLR 7301 with flap AoA 13.1˚

As the angle of attack increases, the acceleration of the flow on the upper surface of the main element increases also. This makes the streamlines more compact, and also the pressure drop on the upper surface of the main element increases. In addition, with the increasing angle of attack the region of high pressure on the lower surface of the main element becomes larger. This promotes higher lift forces, which is consistent with the computations. An important feature of the NLR 7301 airfoil is the region between its lower surface and the flap. There were no vortex formations in this region for the flows considered. If there were a vortex formation in this region, due to the pressure drop associated with it, there would be decrease in the lift force accompanied by an increase in the drag force since the orientation of the face normal

of the main element is towards increasing the lift and decreasing the drag in this region. Hence viscous calculations are of great importance in this region because of a possibility of separation.

CHAPTER 5

CONCLUSIONS

In the subsonic calculations, the difference between the accuracy of a first order and a second order formulation has been illustrated. The first order method is inadequate in capturing the flow characteristics such as the peak of the pressure distribution for the relatively simple problem of subsonic flow. There is however a considerable improvement of the solution with the introduction of solution refinement. This is due to the fact that with solution refinement, the mesh around the regions of high gradients, the stagnation region in case of NACA0012 subsonic flow, is refined and the accuracy in this region increases as the peak of the pressure distribution can be captured more accurately.

Even though solution refinement did introduce an improvement on the first order solution, it still wasn't accurate enough. The second order method performed much better than a first order solution with refinement. When solution refinement was performed for a second order formulation, there was little improvement in the solution for NACA0012 subsonic flow, since the non-adapted solution performed reasonably well, to capture the peak of the solution refinement.

The second order method was superior to the first order one in terms of accuracy, but it did call for a much increased computation time. To resolve this issue, first order calculations would be performed until some level of convergence is obtained then the solution would switch to a second order formulation. This resulted in up to more than 50% decrease in the computation time while there was no virtual loss in terms of accuracy. Also as the angle of attack was varied to construct a lift coefficient vs. chord graph it was seen that at certain angles it was not possible to get a solution with fully second order calculations. This and the fact that second order solutions

provided residual plots with considerable scattering and oscillations indicated that the first order formulation is more stable than the second order one. Hence by starting with first order calculations, the field is initialized more accurately which promotes the second order method to converge as it is sensitive to the initial conditions.

The transonic flow around the NACA0012 profile was a more challenging case than the subsonic flow, providing grounds to test the performance of different methods for evaluating the flux terms. The main challenge was to catch the shock locations, especially the stronger one on the upper surface of the airfoil. The AUSMD, AUSMV and van Leer's methods were the ones that showed the best performance on this aspect.

For the transonic flow solution refinement is a must to get an accurate representation of the flow field since it is already known that there will be large gradients at shock locations in addition to the stagnation region. If solution refinement is not used smeared shocks are obtained. It was however possible to get an accurate pressure distribution on the airfoil as the mesh elements in this region are small in size. Hence just to analyze the forces on the airfoil a solution without refinement can be employed to get quick results.

It was not possible to compare the computational performance of the methods with a solution with refinement, so calculations were also performed without refinement. For the solutions without refinement it was seen that, the Roe's method and the AUSM method converged easily with a CFL safety coefficient of 1. The AUSMV method converged with a CFL safety coefficient of 0.5 while the van Leer's method diverged.

Another important feature of the solutions for the transonic flow was the oscillations seen at the shock locations, the one on the upper surface of the airfoil with the stronger shock being more apparent. This is due to the poor performance of the limiters used in the calculations. A limiter that won't hamper the convergence while preventing oscillations should be implemented to improve the solution.

The NLR 7301 with a flap was also a challenging case to test the performance of the various methods implemented for evaluating the flux terms. The AUSM method was superior in terms accuracy and it was second to van Leer's method in terms of computational performance. The van Leer's method with the poorest performance for the case with an angle of attack of 6˚ did improve with the application of solution refinement.

The performance of both the Roe's and van Leer's methods improved for the cases with higher angle of attacks. This might be due to the flow shifting closer to the compressible range with the increasing angle of attacks promoting higher velocities in the field. The performance of the AUSMD method was consistent throughout the calculations while the AUSMV method failed for large angle of attack values.

From the pressure coefficient vs. chord graphs, it was observed that the estimation of the peak pressure on the upper surface of the main element was crucial in the prediction of the lift coefficient. van Leer's method with solution refinement and AUSM method performed well on this aspect, while AUSMD, AUSMV, and Roe's method performed worse with similar results at an angle of attack 6˚. For the angle of attack values of 10.1˚ and 13.1˚, AUSM was the superior method once again while the performance of Roe's method improved considerably. The van Leer method with solution refinement provided over estimations of the pressure peak.

BIBLIOGRAPHY

1. **Wendt, John F, et al.** *Computational Fluid Dynamics An Introduction.* Berlin : Springer_Verlag, 1996.

2. **Versteeg, H K and Malalasekera, W.** *An Itroduction to Computational Fluid Dynamics The Finite Volume Method.* Malaysia : Prentice Hall, 1995.

3. **Liseikin, Vladimir D.** *Grid Generation Methods.* Berlin : Springer-Verlag, 1999.

4. **Thompson, Joe F, Soni, Bharat K and Wheatherill, Nigel P.** *Handbook of Grid Generation* : CRC Press, 1998.

5. **Hirsch, Charles.** *Numerical Computation of Internal and External Flows.* New York : John Wiley & Sons, 1988.

6. **Reddy, J N.** *An Introduction to the Finite Element Method.* Singapore : McGraw-Hill, 1993.

7. **Hoffmann, Klaus A and Chiang, Steve T.** *Computational Fluid Dynamics for Engineers.* Wichita : Enginnering Education System, 1995.

8. *Reentrant Polygon Clipping.* **Sutherland, I E and Hodgeman, G W.** January 1974, Communications of the ACM, pp. 32-42.

9. *A New Concept and Method for Line Clipping.* **Liang, Y D and Barsky, B A.** 1, January 1984, ACM Transactions on Graphics, Vol. 3, pp. 1-22.

10. **Sproull, R F and Sutherland, I E.** *A Clipping Divider.* Washington D. C. : Thompson Books, 1968.

11. *An Efficent Algorithm for 2-D Line Clipping: Its Development and Analysis.* **Nicholl, Tina M, Lee, D T and Nicholl, Robin A.** July 1987, Computer Graphics, pp. 253-262.

12. *A New Two Dimensional Line Clipping Algorithm for Small Windows.* **Day, J D.** 1992, Computer Graphic Forums, pp. 241-245.

13. *A Fast Two-Dimensional Line Clipping Algoritm via Line Encoding.* **Sobkow, M S, Pospisil, P and Yang, Y H.** 1987, Computer Graphics, pp. 459-467.

14. **De Zeeuw, Darren L.** *A Quad-Tree Based Adaptively-Refined Cartesian-Grid Algorithm for the Solution of The Euler Equations.* Michigan : The University of Michigan, 1993. PhD thesis.

15. **Preparata, P Franco and Shamos, Michael Ian.** *Computational Geometry an Introduction.* New York : Springer-Verlag, 1985.

16. **Toro, E F.** *Riemann Solvers and Numerical Methods for Fluid Dynamics.* Berlin : Springer-Verlag, 1999.

17. **Laney, Culbert B.** *Computational Gas Dynamics.* Cambridge : Cambridge University Press, 1998.

18. **Greenberg, Michael D.** *Advanced Engineering Mathematics.* New Jersey : Prentice Hall, 1998.

19. *Approximate Riemann Solvers, Parametrized Vectors, and Difference Schemes.* **Roe, P L.** 1981, Journal of Computational Physics, Vol. 43, pp. 357-372.

20. *Flux Vector Splitting for the Euler Equations.* **van Leer, B.** s.l. : Springer-Verlag, 1982. Proceedings of the 8th International Conference on Numerical Methods in Fluid Dynamics.

21. *A New Flux Splitting Scheme.* **Liou, M S and Steffen, C J.** s.l. : Journal of Computational Physics, 1993, Vol. 107, pp. 23-39.

22. *An Accurate and Robust Vector Splitting Scheme for Shock and Contact Discontinuities.* **Wada, Yasuhiro and Liou, M S.** 3, s.l. : Siam J. Sci. Comput., 1997, Vol. 18, pp. 633-657.

23. *Flux Vector Splitting of the Inviscid Gasdynamic Equations with Applications to Finite Difference Methods.* **Steger, J L and Warming, R F.** s.l. : Journal of Computational Physics, 1981, Vol. 40, pp. 263-293.

24. **Barth, Timothy J.** *Simplified Numarical Methods for Gasdynamic Systems on Triangulated Domains.* Stanford : Stanford University, 1998. PhD thesis.

25. **Barth, Timothy J and Frederickson, Paul O.** *Higher Order Solution of the Euler Equations.* Reno : AIAA paper AIAA-90-0013, 1990. 28th Aerospace Sciences Meeting.

26. **Barth, Timothy J and Jespersen, Dennis C.** *The Design and Application of Upwind Schemes on Unstructured Meshes.* Reno : AIAA paper AIAA-89-0366, 1989. 27th Aerospace Sciences Meeting.

27. **Coirier, William John.** *An Adaptively Refined, Cartesian, Cell-Based Scheme for the Euler and Navier Stokes Equations.* Michigan : The University of Michigan, 1994. PhD thesis.

28. **Barth, Timothy J.** *Recent Developments in High Order K-Exact Reconstruction on Unstructured Meshes.* Reno : AIAA paper AIAA-93-0668, 1993. 31st Aerospace Sciences Meeting.

29. *Gerris: A Tree-Based Adaptive Solver for the Incompressible Euler Equations in Complex Geometries.* **Popinet, Stéphane.** 2003, Journal of Computational Physics, Vol. 190, pp. 572-600.

30. **Lambert, J D.** *Computational Methods in Ordinary Differential Methods.* London : Wiley, 1973.

31. **Blazek, J.** *Computational Fluid Dynamics: Principles and Applications.* St Augustin : Elsevier, 2001.

32. **Amick, J L.** *Comparison of the Experimental Pressure Distribution on an NACA0012 Profile at High Speeds with that Calculated by the Relaxation Method.* s.l. : National Advisory Committee for Aeronautics, 1950. Technical note.

33. **Özdemir, Enver Doruk.** *Implementation of Rotation into a 2-D Euler Solver.* Ankara : METU, 2005. Masters thesis.

34. **Abbott, Ira H and von Doenhoff, Albert E.** *Theory of Wing Sections,Including a Summary of Airfoil Data.* New York : Dover Publications, 1959.

35. **AGARD Subcommittee C.** *Test Cases for Inviscid Flow Field Methods.* 1986 : AGARD Advisory Report 211.

36. **Advisory Group for Aerospace Research& Development.** *A Selection of Experimental Test Cases for the Validation of CFD Codes* . s.l. : AGARD Advisory Report No 303, 1994.

APPENDIX A

COORDINATES OF NACA0012

Table A.1- Coordinates of NACA0012 Profile

x	y
0.999753	0.001295
0.999013	0.001398
0.997781	0.001571
0.996057	0.001812
0.993844	0.002120
0.991144	0.002496
0.987958	0.002937
0.984292	0.003443
0.980147	0.004012
0.975528	0.004642
0.970440	0.005333
0.964888	0.006082
0.958877	0.006887
0.952414	0.007746
0.945503	0.008658
0.938153	0.009619
0.930371	0.010628
0.922164	0.011681
0.913540	0.012778
0.904508	0.013914
0.895078	0.015088
0.885257	0.016297
0.875056	0.017539
0.864484	0.018809
0.853553	0.020107
0.842274	0.021429
0.830656	0.022773
0.818712	0.024135

Table A.1- Coordinates of NACA0012 Profile (continued)

0.806454	0.025514
0.793893	0.026905
0.781042	0.028307
0.767913	0.029717
0.754521	0.031131
0.740877	0.032547
0.726995	0.033962
0.712890	0.035374
0.698574	0.036778
0.684062	0.038172
0.669369	0.039553
0.654508	0.040917
0.639496	0.042263
0.624345	0.043585
0.609072	0.044882
0.593691	0.046149
0.578217	0.047383
0.562667	0.048581
0.547054	0.049739
0.531395	0.050854
0.515705	0.051923
0.500000	0.052940
0.484295	0.053904
0.468605	0.054810
0.452946	0.055655
0.437333	0.056436
0.421783	0.057148
0.406309	0.057789
0.390928	0.058355
0.375655	0.058844
0.360504	0.059251
0.345492	0.059575
0.330631	0.059812
0.315938	0.059960
0.301426	0.060017
0.287110	0.059980
0.273005	0.059848
0.259123	0.059619
0.245479	0.059292
0.232087	0.058866

Table A.1- Coordinates of NACA0012 Profile (continued)

0.218958	0.058340
0.206107	0.057714
0.193546	0.056987
0.181288	0.056160
0.169344	0.055233
0.157726	0.054207
0.146447	0.053083
0.135516	0.051863
0.124944	0.050547
0.114743	0.049138
0.104922	0.047638
0.095492	0.046049
0.086460	0.044374
0.077836	0.042615
0.069629	0.040776
0.061847	0.038859
0.054497	0.036867
0.047586	0.034803
0.041123	0.032671
0.035112	0.030473
0.029560	0.028213
0.024472	0.025893
0.019853	0.023517
0.015708	0.021088
0.012042	0.018607
0.008856	0.016078
0.006156	0.013503
0.003943	0.010884
0.002219	0.008223
0.000987	0.005521
0.000000	0.000000

APPENDIX B

COORDINATES OF NLR 7301 & FLAP

Table B.1- The coordinates of NLR 7301

x	y
0.94360	0.01499
0.94267	0.01519
0.93988	0.01580
0.93524	0.01690
0.92878	0.01830
0.92051	0.02008
0.91047	0.02241
0.89870	0.02512
0.88524	0.02819
0.87015	0.03162
0.85349	0.03536
0.83532	0.03941
0.81572	0.04368
0.79476	0.04814
0.77253	0.05273
0.74911	0.05735
0.72459	0.06191
0.69908	0.06628
0.67267	0.07038
0.64547	0.07410
0.61758	0.07737
0.58912	0.08015
0.56019	0.08248
0.53092	0.08438
0.50141	0.08590
0.47178	0.08704
0.44216	0.08781
0.41265	0.08826
0.38337	0.08838
0.35444	0.08818
0.32598	0.08768

Table B.1- The coordinates of NLR 7301 (continued)

0.29809	0.08687
0.27098	0.08577
0.24448	0.08440
0.21897	0.08276
0.19445	0.08087
0.17103	0.07874
0.14880	0.07638
0.12784	0.07381
0.11786	0.07245
0.10824	0.07103
0.09897	0.06958
0.09007	0.06807
0.08155	0.06650
0.07341	0.06488
0.06567	0.06317
0.05832	0.06137
0.05139	0.05943
0.04487	0.05731
0.03877	0.05506
0.03309	0.05268
0.02786	0.05009
0.02305	0.04717
0.01870	0.04373
0.01479	0.03978
0.01133	0.03544
0.00832	0.03076
0.00577	0.02582
0.00368	0.02064
0.00206	0.01516
0.00089	0.00959
0.00019	0.00422
-0.00004	-0.00080
0.00019	-0.00552
0.00089	-0.00992
0.00206	-0.01417
0.00368	-0.01804
0.00577	-0.02173
0.00832	-0.02521
0.01133	-0.02851
0.01479	-0.03158
0.01870	-0.03445

Table B.1- The coordinates of NLR 7301 (continued)

0.02305	-0.03717
0.02786	-0.03972
0.03310	-0.04215
0.03877	-0.04443
0.04487	-0.04661
0.05139	-0.04873
0.05832	-0.05073
0.06567	-0.05263
0.07341	-0.05446
0.08155	-0.05622
0.09007	-0.05791
0.09897	-0.05954
0.10824	-0.06109
0.11786	-0.06259
0.12784	-0.06402
0.14880	-0.06672
0.17103	-0.06917
0.19445	-0.07132
0.21897	-0.07317
0.24448	-0.07470
0.27089	-0.07585
0.29809	-0.07666
0.32598	-0.07704
0.35444	-0.07701
0.38337	-0.07652
0.41265	-0.07550
0.44216	-0.07385
0.47178	-0.07144
0.50141	-0.06819
0.53092	-0.06417
0.56019	-0.05959
0.58912	-0.05459
0.61758	-0.04921
0.64547	-0.04355
0.67267	-0.03750
0.69908	-0.03080
0.72459	-0.02362
0.74911	-0.01597
0.77253	-0.00824
0.79476	-0.00080
0.81572	0.00585

Table B.1- The coordinates of NLR 7301 (continued)

0.83532	0.01115
0.85349	0.01472
0.87015	0.01702
0.88524	0.01818
0.89870	0.01843
0.91047	0.01807
0.92051	0.01733
0.92878	0.01645
0.93524	0.01530
0.93988	0.01460
0.94267	0.01423
0.94360	0.01410

Table B.2- The coordinates of flap

x	y
1.205092	-0.102133
1.204014	-0.101411
1.200754	-0.099373
1.195420	-0.095931
1.188106	-0.091056
1.178790	-0.085249
1.167564	-0.078726
1.154588	-0.071662
1.140013	-0.064282
1.124077	-0.056694
1.106992	-0.049135
1.098093	-0.045428
1.088996	-0.041798
1.079729	-0.038286
1.070330	-0.034929
1.060832	-0.031728
1.051260	-0.028701
1.041673	-0.025861
1.032094	-0.023205
1.022570	-0.020749

Table B.2- The coordinates of flap (continued)

1.013137	-0.018508
1.003821	-0.016532
0.994643	-0.014820
0.985653	-0.013410
0.976874	-0.012269
0.968366	-0.011407
0.960148	-0.010799
0.952264	-0.010473
0.944743	-0.010407
0.937624	-0.010583
0.930955	-0.010922
0.924783	-0.011390
0.919139	-0.011985
0.914029	-0.012722
0.909442	-0.013659
0.905415	-0.014812
0.901946	-0.016156
0.899047	-0.017719
0.896720	-0.019522
0.895009	-0.021474
0.893925	-0.023517
0.893589	-0.025374
0.893925	-0.027199
0.894976	-0.028901
0.896887	-0.030054
0.899614	-0.030749
0.903046	-0.031232
0.907107	-0.031741
0.911738	-0.032320
0.916920	-0.032993
0.922644	-0.033757
0.928889	-0.034582
0.935621	-0.035469
0.942821	-0.036418
0.950452	-0.037440
0.958495	-0.038526
0.966901	-0.039670
0.975646	-0.040906
0.984677	-0.042203
0.993974	-0.043586

Table B.2- The coordinates of flap (continued)

1.003479	-0.045045
1.013157	-0.046609
1.022976	-0.048257
1.032883	-0.050011
1.042829	-0.051865
1.052791	-0.053820
1.062706	-0.055875
1.072539	-0.058038
1.082262	-0.060300
1.091824	-0.062652
1.101185	-0.065091
1.119166	-0.070188
1.135943	-0.075465
1.151267	-0.080787
1.164948	-0.085915
1.176820	-0.090662
1.186673	-0.094993
1.194459	-0.098572
1.200104	-0.101159
1.203556	-0.102670
1.204699	-0.103214